CERN-THESIS-2000-053

Particle identification using time-over-threshold measurements in the ATLAS Transition Radiation Tracker

Andrea Manara

Submitted to the faculty of the Graduate School
in partial fulfillment of the requirements
for the degree
Doctor of Philosophy
in the Department of Physics,
Indiana University

October 2000

Accepted by the Graduate Faculty, Indiana University, in partial fulfillment of the requirements of the degree of Doctor of Philosophy.

Doctoral Committee

Professor Harold Ogren
(Chairman)

Doctor David Rust

Professor Steve Vigdor

31 October 2000

Professor Andrej Zieminski

To my parents.

Acknowledgements

I would like first of all to thank my supervisor Harold Ogren, who gave me the opportunity to join the ATLAS TRT group and has supported my work all the way along. Under his guidance I always felt on the right path towards a Ph.D. degree. I would also like to thank Fred Luehring for having been a constant help with his great computing skills and for several useful discussions. I really enjoyed the many dinners in Geneve with Harold and Fred, I always felt them to be both friends and colleagues. I would like more generally to mention the entire Indiana TRT group as a very nice place to be a graduate student, both from the human and professional point of view.

From the CERN TRT group I would like to acknowledge the many helpful discussions with David Rousseau during the development of the time-over-threshold technique for the TRT. I also would like to thank Daniel Froidevaux and Anatoli Romaniouk for their feedback which surely improved the quality of my work. I also enjoyed the collaboration with Paula Eerola, Sander Nooij and Jerome Damet, who I thank for his hospitality in Uppsala.

I would like finally to mention Steve Vigdor. I worked with him in the DISTO collaboration and he convinced me to come to Indiana University. I really enjoyed working with Steve and with Will Jacobs and Mario Dzemidzic as well.

Abstract

The Transition Radiation Tracker (TRT) in the ATLAS Inner Detector was designed to be a powerful tracking device and to provide electron identification via transition-radiation detection. The TRT is a straw drift-tube detector, with a central barrel section and two end-cap sides, which will give an average of 35 straws crossed per track. Part of the barrel TRT is presently in construction at Indiana University. The straw tubes are filled with a Xe-based gas mixture, that strongly absorbs transition-radiation photons produced by the passage of ultra-relativistic charged particles (electrons) in the radiator material which surrounds the straws. The straw output signal is discriminated in the front-end electronics at a low-threshold level (200 eV) and at a high-threshold level (5000 eV). This thesis describes a novel technique for particle identification with the ATLAS TRT. Detailed Monte Carlo simulation and test-beam experiments lead to the the conclusion that time-over-threshold measurements can improve electron identification at low energy. Time-over-threshold is defined as the width of the discriminated signal above the low-threshold level. The use of time-over-threshold also provides some kaon-pion separation, thereby significantly enhancing the B-physics capabilities of the ATLAS detector. The application of this novel technique for the study of the decay $B \rightarrow KK\pi$ is described in this thesis.

Contents

Acknowledgements **iv**

Abstract **v**

Introduction **1**

1 The Large Hadron Collider **8**

1.1 The LHC project 9

1.1.1 The design concept of the LHC 12

1.1.2 Performance of the LHC 14

1.2 LHC experiments 17

1.2.1 ATLAS 17

1.2.2 CMS 17

1.2.3 LHCb and B physics 18

1.2.4 ALICE and quark-gluon plasma 19

1.3 Physics at the LHC 20

1.3.1 The Standard Model 20

1.3.2 Beyond the Standard Model 24

2 The ATLAS experiment **26**

2.1 The ATLAS detector 27

2.2 Magnet System 30

2.3 Inner Detector 32

2.3.1 Pixel detector 33

2.3.2 Semiconductor tracker (SCT) 34

2.3.3 Transition Radiation Tracker (TRT) 35

2.4 Calorimetry 35

2.5 Muon system 37

2.5.1 Monitored Drift-Tube chambers 40

2.5.2 Cathode Strip Chambers 40

2.5.3 Resistive Plate Chambers 41

2.5.4 Thin Gap Chambers 41

2.6 Trigger and data-acquisition system 42

3 The Transition Radiation Tracker **45**

3.1 Detector Description 46

3.2 Expected performance of the TRT 48

3.3 The TRT straw drift-tube 50

3.3.1 Gas composition 51
3.3.2 Straw signal, gas gain and stability of operation 52
3.3.3 Straw operating conditions at the LHC 55
3.4 Design and Construction of the Barrel TRT 57
3.4.1 Barrel Module Components and Design 58
3.4.2 Assembly Procedures 64
3.5 The TRT electronics 66
3.5.1 The front-end electronics 66
3.5.2 The read-out electronics 72

4 Particle identification using the TRT detector 75

4.1 Ionization 75
4.2 Transition Radiation 79
4.2.1 Single interface 79
4.2.2 Single foil 81
4.2.3 Radiator 82
4.3 Particle identification in the TRT 87
4.3.1 Cluster-counting technique 87
4.3.2 Time-over-threshold method 90

5 Test-beam experiment 93

5.1 Experimental set-up 94

5.1.1 Track reconstruction 96

5.1.2 Particle identification 98

5.2 Time-over-threshold measurement 99

5.2.1 Time-over-threshold studies with a single straw 99

5.2.2 Time-over-threshold studies with pseudo-tracks 102

5.2.3 Performance obtained for electron-pion separation 104

6 Monte Carlo simulation 109

6.1 Simulation framework 110

6.1.1 GEANT 111

6.2 Simulation of the TRT straw tube response 113

6.3 Simulation of the test-beam experiment 115

6.4 Expected performance for e/π separation in the ATLAS TRT 119

6.4.1 Comparison between pseudo-tracks and the full ATLAS Monte Carlo 120

6.5 Expected performance for K/π separation in the ATLAS TRT 122

6.6 Parameterization of the $\frac{dE}{dx}$ estimator 123

6.7 Study of the $B^+ \rightarrow K^+K^+\pi^-$ decay 124

6.7.1 Event simulation 126

6.7.2 Fast simulation parameterization 127

6.7.3 Analysis 128

6.8 The $B_d^0 \rightarrow \pi^+\pi^-$ decay 135

Conclusion **137**

References **142**

List of Figures

1.1 Schematic layout of the LHC. 10

1.2 Injection scheme for the LHC. 11

1.3 Schematic view of a twin-bore magnet for the LHC. 13

1.4 Cross-sections for various processes as a function of the center-of-mass energy. The working line for various machine is given. The event rate is also shown, for the LHC nominal luminosity. From [6]. 15

2.1 The ATLAS detector. 28

2.2 Toroidal bending power. 31

2.3 The Inner Detector layout. 32

2.4 The structure of the barrel accordion calorimeter. 36

2.5 The muon spectrometer. 39

2.6 Trigger chambers. 39

2.7 Block diagram of the Trigger/DAQ system 43

3.1 Perspective view of the TRT layout. The barrel modules and the end-cap wheels are shown, as well as the barrel assembly frame. 46

3.2 Schematic view of the TRT detector in the R-z plane. The main dimension of the detector are shown on the left (resp. right) hand side for the active detector volume (resp. the physical detector envelopes). Units are in mm. 47

3.3 Illustration of the histogramming technique used to find tracks in the barrel TRT. The hit straws are displayed in the R-ϕ plane, the expected pile-up at a luminosity of $2 \cdot 10^{34} cm^{-2} s^{-1}$ is overlaid on top of five electron and five muon tracks of $p_T = 20\,\mathrm{GeV}$. The top histogram shows that the TR-hits alone are sufficient to extract the electron signal from the fluctuations of the pile-up background, whereas the bottom shows that the use of the full TRT information clearly separates the isolated high-p_T tracks from the background. 49

3.4 Total predicted charge-collection time in a magnetic field of 2 T as a function of the CF_4 concentration for straws with a gas mixture containing 70% Xe and at their nominal gas gain of $2.5 \cdot 10^4$. The remainder of the gas is CO_2. 52

3.5 Precise measurements of the straw current response to a point-like ionization. The measurements are well represented by the parametrisation, which has been used for the design of the front-end amplifier and shaper. 53

3.6 Straw gas gain and self-limited streamer discharge probability as a function of the high-voltage. 54

3.7 Effect of space-charge, expressed as the observed fraction of the total amplitude, as a function of the straw gas gain and for different X-ray energies. 54

3.8 Relative gas-gain variation as a function of the wire offset for the nominal TRT gas mixture. For wire offset below 300 μm, the gas gain variation is lower than 5%. 56

3.9 Straw hit probability for energy above 0.2 keV as a function of the photon energy and of the magnetic field. 58

3.10 A view of a barrel module showing a straw alignment plate, the straws, stacks of fiber radiator, and the shell. 59

3.11 Layout of the barrel TRT showing three layers of barrel modules (type I in the inner layer, type II in the middle layer, and type III in the outer layer) and the support structure. 59

3.12 Side view of the module end-plate region. The tension plate, on the top, holds the wires and forms one side of the gas manifold. The straws are glued into the high-voltage plate at the bottom. The wires are centered in the straws by the wire supports inserted in the straw ends (see text). 61

3.13 An high-voltage plate. 62

3.14 Photograph of part of the tension plate. 62

3.15 Printed circuit layout of the tension plate superimposed on the HV board. 63

3.16 The universal assembly fixture. 64

3.17 The Kapton alignment tooling. 64

3.18 Schematic diagram of the TRT electronics. 66

3.19 Block diagram of the ASDBLR circuit. 68

3.20 Simulation of the output of the preamplifier (solid) and shaping circuit (dashed). 69

3.21 Simulation of the signal (for 2 fC (solid line) and 25 fC (dotted line) input charges) after baseline restoration. The larger signal have been scaled to the smaller one. 69

3.22 Output of shaper (top) and discriminator (bottom) of the ASDBLR (20 ns/div). 69

3.23 Low-threshold uniformity. 70

3.24 Counting rate as a function of the low-threshold value. 70

3.25 Schematics of the drift-time measurement circuit. 71

3.26 ROD-ROB bandwidth for a L1A rate of 75 kHz. 74

3.27 Fraction of valid straws as a function of the luminosity and the gate width. 74

4.1 The energy loss curves as a function of momentum for different particles and for different materials. From [7]. 77

4.2 Fractional energy loss per radiation length as a function of electron or positron energy. From [7]. 78

4.3 Differential yield per interface as a function of the photon energy. Results for single interface (monotonic thin line), single slab (dashed line), and multiple foils (thick line) are shown. The particle Lorenz factor is $\gamma = 2 \cdot 10^4$. From [24]. 80

4.4 Comparison of the total generated yield per interface as a function of the particle energy for single interface (thin line), single slab (dashed line), and multi-foil radiator (heavy line). The yield is computed for Mylar-air interface, with foil thicknesses $l_1 = 25\,\mu$m and 127 μm, and spacing $l_2 = 25\,mm$. From [24]. 82

4.5 Differential yield per interface from 15 GeV electrons. Results for single interface (monotonic thin line) and multiple foils (of 25 μm thickness, spaced by 1.5 mm) (thick line) are the same as in Fig. 4.3. The effective yield observable at the exit of the radiator box, and the observable yield in a gaseous detector filled with 4 cm Xe or Kr is also shown. From [27]. 83

4.6 Frequency spectra of transition radiation emerging from three radiator with different foil thickness (from [26]). The points (black circles for 5 GeV and open triangles for 9 GeV electrons) represent measured data, while the curves (dashed line for 5 GeV and solid line for 9 GeV electrons) are results of calculations (see text). 84

4.7 Micro-photograph of a sample of polyethylene fiber radiator. 86

4.8 For 200 GeV electrons and for different type of radiators, probability per straw to observe an energy deposition above a given threshold. . . 86

4.9 Pion misidentification probability as a function of the electron efficiency at 20 GeV, as measured using an end-cap sector prototype. The probabilities to observe a given number of TR-clusters for pions and electrons are shown in the top left-hand corner. 88

4.10 Display of a simulated $B_d^0 \to \mathrm{J}/\psi\ K_s^0$ event in the ATLAS barrel TRT, at low luminosity. Reconstructed tracks are drawn as lines only up to a radius of 50 cm so as not to obscure the TRT hits. The small box selects a part of a pion track from the K_s^0 decay and of an electron track from a J/ψ decay (see Fig. 4.11). 89

4.11 Expanded view of the portion of the tracks within the box in Fig. 4.10. The electron track contains many more high-threshold hits (larger points) than the pion track. Electron identification via transition radiation is based on this difference (see text). 90

4.12 Bethe-Bloch curves for various particles in the ATLAS TRT gas mixture. For the energy range of interest for the TRT, electrons are always on the Fermi plateau, while hadrons are on the relativistic rise up to very large momentum. 91

4.13 Dependence of the time-over-threshold on the track distance, y, from the wire. The straw signal is shown before and after the low-threshold (200 eV) discrimination. 92

5.1 Schematic view of the experimental set-up (not to scale). MWPC's (BC1 and BC2) and silicon detectors (Si1 and Si2) were used for tracking, two scintillators (s1 and s2) were used in coincidence for triggering. Straws for radiator studies (ADC straws), the single straw for the time-over-threshold studies (ToT straw) and the radiator locations are also indicated. The straws that were read out are represented as black circles. 94

5.2 Extrapolation of the BC1-BC2 track to the silicon planes. The upper (resp. lower) distributions show the extrapolation of the track to S1 (resp. S2). The x (resp. y) residual is shown on the left (resp. right). 96

5.3 Extrapolation of the track coordinate inside the straw using the silicon telescope. The 4 mm window of the straw is uniformly illuminated by the beam. 96

5.4 R-t dependence. The drift time is plotted as a function of the track distance to the anode wire, as extrapolated from the silicon telescope. 97

5.5 Residual between the extrapolated coordinate of the track inside the straw and the drift distance, as obtained using the R-t dependence. . 97

5.6 Particle identification in the test-beam experiment. The pulse-height from the Cherenkov counter is shown as a function of the pulse-height from the Leadglass calorimeter. Pions and electrons are obviously distributed in distinct regions. This distribution is shown after offline cuts on pulse-height. 98

5.7 Uncorrected time-over-threshold distributions for 5 GeV pions and electrons for hits without high-threshold discriminator level. 100

5.8 Uncorrected time-over-threshold distributions for 5 GeV pions and electrons for all hits. 100

5.9 Parameterization of the dependence of time-over-threshold upon the distance of closest approach to the anode wire (y) for 5 GeV pions. The points represent the mean value for each y bin of width 200 μm, and the error bars represent the r.m.s. of the time-over-threshold distribution in each y bin. 101

5.10 Correlation between the corrected time-over-threshold residuals (Δ_{ToT}) and the distance of closest approach for 5 GeV pions and electrons. The points represent the mean value for each y bin, and the error bars represent the statistical uncertainty on these mean values. 101

5.11 Corrected time-over-threshold residuals, Δ_{ToT}, for a single straw without high-threshold hits and for samples of 5 GeV pions and electrons (see text). 102

5.12 $< \Delta_{ToT} >$ (no high-threshold hits) for 5 GeV pseudo-tracks. The vertical line represents the $< \Delta_{ToT} >$ value for a 90% electron efficiency. 103

5.13 $< \Delta_{ToT} >$ (all hits) for 5 GeV pseudo-tracks. The vertical line represents the $< \Delta_{ToT} >$ value for a 90% electron efficiency. 103

5.14 Number of high-threshold hits for 5 GeV pseudo-tracks. 104

5.15 Pion misidentification probability versus electron efficiency, as obtained using $< \Delta_{ToT} >$ at 5 GeV for pseudo-tracks constructed from the test-beam data. The open circles are calculated using all the hits along the pseudo-track, whereas the black circles are calculated using only hits without high-threshold discriminator level. The large (resp. small) circles correspond to $< \Delta_{ToT} >$ corrected (resp. uncorrected) for the track position inside the straw. 105

5.16 Distribution of $< \Delta_{ToT} >$ (no high-threshold hits) versus number of high-threshold hits for 5 GeV pseudo-tracks. Electrons are plotted as red squares and pions as blue stars. 106

5.17 Distribution of $< \Delta_{ToT} >$ (all hits) versus number of high-threshold hits for 5 GeV pseudo-tracks. Electrons are plotted as red squares and pions as blue stars. 106

5.18 Likelihood distribution for pions (blue line) and electrons (red line), as obtained combining the two discriminating variables, namely the number of high-threshold hit and $< \Delta_{ToT} >$ (all hits). 107

5.19 Pion misidentification probability versus electron efficiency at 5 GeV for pseudo-tracks constructed from test-beam data. The results are shown for the standard cluster-counting technique and for the combined method using also the time-over-threshold information (see text and Table 5.1). 108

6.1 Illustration of how ionized electrons drift to the anode wire in a TRT straw, in the presence of both an electric and a magnetic field. 114

6.2 Monte Carlo simulation of the straw signal. (A) The ionization clusters drift towards the anode and the signal amplitudes and arrival times are recorded. (B) The straw output signal is then convoluted with a model of the response of the front-end electronics. 114

6.3 For a single straw without radiator and for 5 GeV pions, differential energy spectra from test-beam data (histograms) and Monte Carlo simulation (open circles). 116

6.4 For a single straw without radiator and for 5 GeV electrons, differential energy spectra from test-beam data (histograms) and Monte Carlo simulation (open circles). 116

6.5 Integral energy deposition spectra (integrated above 0.2 keV) for 5 GeV pions and electrons, as measured in the test-beam and predicted by Monte Carlo simulations for a single straw without radiator. 117

6.6 Pion misidentification probability as a function of momentum at 90% electron efficiency for pseudo-tracks in the test-beam setup. The performance is shown for $< \Delta_{ToT} >$, without using high-threshold hits (stars), for $< \Delta_{ToT} >$ using all hits (squares), for the transition-radiation cluster-counting technique (circles) and for the overall combined method (triangles). The test-beam data results at 5, 10 and 20 GeV are shown as points, while the Monte Carlo simulation results are shown as lines from 1 GeV to 20 GeV. The errors shown are statistical (above 5 GeV the errors are often smaller than the symbols). . . 118

6.7 Pion misidentification probability as a function of transverse momentum at 90% electron efficiency for simulated single tracks at $\eta = 0.3$ in the ATLAS Inner Detector without pile-up. The performance is shown for $< \Delta_{ToT} >$ without using high-threshold hits (stars), for $< \Delta_{ToT} >$ using all hits (squares), for the transition-radiation cluster-counting technique (circles), and for the overall combined method (triangles). . 119

6.8 $< \Delta_{ToT} >$ (all hits) for reconstructed tracks in the ATLAS barrel TRT at $|\eta| = 0.3$ for 5 GeV pions (solid line) and kaons (dashed line). . . . 123

6.9 Expected K/π separation in the ATLAS TRT as a function of transverse momentum (no pile-up effects included). The separation is shown as an average over the full rapidity coverage (solid line) and at $|\eta| = 0.3$ (dotted line). 123

6.10 Parameterization of the mean of the dE/dx distribution as a function of η for p_{T}=10 GeV pions, kaons and protons (shown in order of decreasing average mean). 124

6.11 Parameterization of the sigma of the dE/dx distribution for 10 GeV p_{T} pions (upper plot), kaons (central plot) and protons (bottom plot). . 124

6.12 Parameterization of the straight line fit parameters of the mean of the dE/dx distribution as a function of p_{T} for kaons. 125

6.13 Parameterization of the straight line fit parameters of the sigma of the dE/dx distribution as a function of p_{T} for kaons. 125

6.14 Feynman diagrams contributions to $b \rightarrow ss\bar{d}$ decay in various models. From [3]. 126

6.15 Invariant mass for all the possible triplets of two positive and one negative curvature tracks. These spectra are not normalized for the number of events expected at the LHC (see text). 128

6.16 The χ^2 distribution for the B-candidate vertex fit. The signal is shown as red line, while the background as blue line. 129

6.17 Transverse momentum distribution for the B candidate. The signal is shown as red line, while the background as blue line. 129

6.18 The distribution of the distance (in mm) between the primary and the displaced vertex. The signal is shown as red line, while the background as blue line. 130

6.19 Dalitz plot for the signal. The invariant mass squared $m^2_{\pi K_1}$ is shown versus $m^2_{\pi K_2}$. 130

6.20 Invariant mass for all the possible triplets of two positive and one negative curvature tracks, after the application of all the cuts described above. These spectra are not normalized for the number of events expected at the LHC (see text). 132

6.21 The χ^2 probability for three degrees of freedom for the signal (dashed line) and the background (solid line), as expected after the proposed second level trigger (see text). 133

6.22 Background misidentification probability as a function of the signal efficiency, for the $\frac{dE}{dx}$ χ^2 probability after the proposed second level trigger (see text). 133

6.23 $\pi^+\pi^-$ mass spectrum in the ATLAS experiment for B_d^0 signal and various backgrounds and for the scenario without kaon-pion separation in the ATLAS TRT. From [51]. 135

6.24 $\pi^+\pi^-$ mass spectrum in the ATLAS experiment for B_d^0 signal and various backgrounds and for the scenario with a kaon-pion separation in the ATLAS TRT as predicted by the study presented in this thesis (see text). 135

Introduction

This thesis describes a method to improve the electron-pion separation of the Transition Radiation Tracker in the ATLAS detector being constructed for the Large Hadron Collider (LHC) at CERN in Geneve (Switzerland).

The LHC will provide proton-proton collisions at the center-of-mass energy of 14 TeV, which is more than one order of magnitude higher than what has been achieved in previous accelerators. A major goal for the LHC will be the search for the Higgs boson, which in the Standard Model of particle physics is responsible for the particle masses, or the discovery of an alternative explanation for the origin of the masses.

The ATLAS detector is a general purpose detector for the LHC. It is designed to search for a Higgs signal in all the interesting decays channels. Among the most predominant signatures of a Higgs boson decay are very high transverse-momentum leptons (both electrons and muons), photons, jets and missing transverse energy (which indicates the passage of very weakly-interacting neutral particles, like neutrinos). The ATLAS detector is composed of several sub-detectors with very well defined purposes. The inner detector performs pattern recognition and measures the momentum of charged particles from their curvature in a 2 T solenoidal magnetic field. The inner detector is composed by discrete high-granularity silicon detectors (using both pixel and strip technologies) and a continuous tracking straw detector, the Transition

Radiation Tracker (TRT). The TRT also contributes to the electron identification power of the ATLAS detector, using transition radiation detection, complementing the calorimeter electron identification power. The electromagnetic calorimeter identifies and measures the energy of electrons and photons. The hadronic calorimeter measures the energy of hadrons and jets. Both calorimeters also provide coarse track-position information and measure missing transverse energy. Muons are the only charged particles that are not absorbed in the calorimeters; they are detected in the muon spectrometer, which is the outer ATLAS subdetector.

Electron identification is important for many physics investigations. The identification of isolated electrons with $p_T > 20\,GeV$ is important for the search of leptonic decays of the Higgs boson, for new vector bosons and the extraction of a clean samples of t-tbar events for the accurate measurement of m_T. The identification of lower-p_T electrons is important, for example, in the context of b-jets tagging, relevant in the study of the Higgs boson decay to b quarks.

In ATLAS, the electron identification is accomplished using information from the electromagnetic calorimeter (ECAL) and the inner detector tracking system. The TRT detector also gives its own contribution using transition-radiation detection. The ECAL is a sampling calorimeter with interleaved layers of liquid argon and lead. Electrons and photons, interacting with lead atoms, produce electromagnetic showers (cascades of daughter electrons and photons). The energy produced in the shower is measured (sampled) in the liquid argon layer. The ECAL is segmented in three longitudinal sections. The first section is equipped with strip towers, which provide a precise η measurement, the middle section is segmented in square towers, while the back section in larger rectangular towers. In general, electrons and photons are completely absorbed in the ECAL. Hadrons, on the other end, get through and are absorbed in the much larger hadronic calorimeter.

The TRT detector, whose barrel part is being constructed in Indiana University and other U. S. institutions, is a straw drift-tube detector with an average of 35 straws crossed per track. The straw tubes are filled with a Xe-based gas mixture, which strongly absorbs transition-radiation photons produced by the passage of ultra-relativistic charged particles in the radiator material which surrounds the straws. The transition-radiation photon is emitted at very small angle with respect to the parent-particle trajectory, and it is therefore detected in the same straw crossed by the ionizing particle. The absorption of a transition-radiation photon produces a very intense point-like energy deposition in the straw gas which can be distinguished from the usually lower-energy track-ionization clusters. For the purpose of electron tagging, the straw signal is discriminated in the front-end electronics at the high-threshold level of 5000 eV. The cluster-counting technique provides electron identification by counting the number of high-threshold hits along the track. Pions occasionally may be misidentified as electron due to some δ-rays which can be produced along the tracks. These δ-rays produce very large localized energy deposition in the straw and constitute the main background for electron identification using the cluster-counting technique. For particle energy below 2 GeV, in addition, the cluster-counting technique performance degrades since transition-radiation production from electrons is not yet saturated.

Several different approaches have been devised for electron identification in the low and high p_T range using the combined electromagnetic calorimeter-inner detector system. For the high-p_T electron search, the main background is constituted by QCD-jets. The isolated electron-to-jet ratio at the LHC is expected to be around 10^{-5} at $p_T \sim 20 - 40\,GeV$. The information from the electromagnetic calorimeter is first used to identify isolated cell with large energy deposition, providing a jet rejection of about a factor 10^2. A charged track pointing towards that cluster is searched for in the inner detector. The reconstructed momentum of the track is required to match the reconstructed energy in the calorimeter. The jet background, which after the calorimeter energy cuts consists mainly of high-p_T π^0 and η mesons, is expected to be reduced to about a factor $4 \cdot 10^4$ for a 75% electron efficiency. The use of the TRT transition-radiation cluster-counting technique, provides additional electron identification completely independent on the calorimeter measurement, and gives a jet-rejection higher than $1.5 \cdot 10^5$ (resp. $0.45 \cdot 10^5$) for a 68% electron efficiency, at low luminosity (resp. high luminosity).

For low-p_T electron identification, the inner detector is used in the first step to reconstruct charged particle tracks by placing cuts on the number of precision (pixel and silicon strip) hits and the number of TRT hits. In order to remove photon conversion a cut is also placed on the number of pixel hits alone. To remove hadrons (mostly pions) in a first instance a cut is also placed on the number of high-threshold hits along the reconstructed track in the TRT (cluster-counting technique). The information from the inner detector is then matched to the EM calorimeter. The momentum measured in the inner detector is required to match the energy measured in the EM calorimeter in the most energetic 3x3 cluster of cells containing the cell hit by the charged track. A cut on the difference between the pseudo-rapidity of the track as measured by the tracker and by the calorimeter is also applied. The information from the calorimeter alone is used in the last step, by cutting on the energy measured in the first longitudinal sampling, the ratio of energy in the third and first longitudinal sampling, and the shower width, as measured using the η-strip of the calorimeter. Detailed Monte Carlo simulations for soft-electron b-jets tagging using the procedure previously described, show that for a $\sim 60\%$ efficiency for the identification of events with a soft-electron in a b-jet, a rejection of b-jets as high as 10^3 can be achieved.

In the low-energy region, techniques based on energy loss measurements are very successful, due to significant differences in the relativistic rise of the energy loss for different particles. The Bethe-Bloch formula describes the average energy loss; the individual loss fluctuates as described by the Landau distribution. The long high-energy tail of the Landau distribution complicates the particle identification.

Traditionally, multisampling gaseous detector have been used to provide excellent electron-pion separation. By performing multiple measurement of the energy loss for a given particle and rejecting the higher-energy measurements (truncated mean), the fluctuation of the energy loss due to the Landau tail are considerably minimized. The Opal drift wire chamber, for example, is designed to measure the energy loss of particles by multiple measurements of the ionization along a track. The charged deposited on the wire (which measure the energy loss) is recorded using fast ADC. On average, 100 measurements per track are available with these chambers. The highest 30% measurement are rejected according to the truncated mean technique. The Opal chamber gives an electron-pion separation ranging from 2σ for 15 GeV-momentum particles to 6σ for 2.5 GeV-momentum particles.

My thesis focuses on the development of additional electron-pion separation at low energy using energy loss information. In the TRT only 35 straws will be crossed on average by a track and complete information on the energy loss is not available. Partial information on the energy loss however is already available in the TRT front-end electronics. The straw signal is discriminated at the low-threshold level of 200 eV, and the time of the leading and trailing edges of the signal above the low level are recorded. The time of the leading edge of the signal is used to precisely reconstruct the position of the track inside the straw, and allows the TRT to be used as a tracker. The use of this information as an energy loss estimator, discussed in [1], motivated my research of discriminating variables based on signal shaping information.

The work presented in this thesis shows how a consistent improvement for the electron identification power in the low-energy region may be provided by the time-over-threshold (the width of the low-threshold discriminator), used as an estimator of the energy loss.

Detailed Monte Carlo simulations which I performed in the first part of 1999, and whose results were shown in the Krakow TRT workshop (June 1999), motivated the TRT collaboration to study the time-over-threshold performance in a test-beam experiment. The test-beam experiment was run in September 1999 at the H8 line at the CERN SPS. For this experiment I contributed to the experimental set-up, the data-taking and I performed the time-over-threshold data analysis. Pion and electron beams of different energy were used to study the performance for the electron-pion separation for a straw equipped with a version of the analog front-end chip very close to the final design. The analysis required track reconstruction using multiwire proportional chambers and silicon micro-strip detectors and particle selection using a Cherenkov and a leadglass calorimeter detector. I used the ATLAS Monte Carlo simulation, tuned to reproduce the test-beam results, in order to make reliable predictions for the electron-pion separation to be expected in ATLAS. The ATLAS simulation showed that, for energy lower than 10 GeV, a significant improvement with respect to the standard transition-radiation cluster-counting technique can be obtained by using the time-over-threshold information. In particular, a factor of two improvement is expected at 5 GeV, while at the lower energy of 0.6-2 GeV the improvement is expected to be as large as one order of magnitude [2].

The time-over-threshold technique provides some hadron identification, which is useful for B-physics studies with the ATLAS detector. CP-violation studies and the search for physics beyond the Standard Model in rare B decays are amongst the most interesting topics. I have developed a parameterization of the time-over-threshold as a function of p_T and η, which can be used as a tool for hadron identification. I describe in this thesis how this parameterization has been applied for enhancing the signal-to-background ratio for the study of the $B^+ \rightarrow K^+K^+\pi^-$ decay, a rare decay which if seen by ATLAS would provide hints of physics beyond the Standard Model [3].

Chapter 1

The Large Hadron Collider

The Large Hadron Collider (LHC) [4, 5] is the new particle accelerator in construction at CERN. CERN stands for 'Centre Europeenne pour la Recherche Nucleaire', name that recently was changed in 'Organisation Europeenne pour la Recherche Nucleaire'. The LHC should be completed by 2005 and provide proton-proton collisions. Proton beams will collide head-on with an energy of 7 TeV per beam, providing a center-of-mass energy of 14 TeV, which is one order of magnitude higher than that reached in a previous collider (the Tevatron at Fermilab). The LHC design luminosity is $10^{34}cm^{-2}s^{-1}$. In the first three years, when the LHC performance is still being optimized, the machine will provide lower luminosity ($10^{33}cm^{-2}s^{-1}$), and the LHC experiments will be mainly devoted to B-physics studies.

At the highest luminosity, the LHC will allow a test of the Higgs sector of the Standard Model, the current best theoretical model of the elementary particles and their interactions. In the Standard Model, the so-far undiscovered Higgs boson is responsible for the masses of all the known particles. Its discovery is the main challenge for the LHC, but also in the case in which the Higgs boson would turn out to be just an artifact of the theory, the LHC would provide indications for the onset of new physics beyond the Standard Model.

1.1 The LHC project

Progress in physics has always been accompanied by the development of new technologies in particle accelerators. The development of superconducting magnet technologies, as an example, permited more energetic beams in the same accelerator ring. This has led to an increasing center-of-mass energy and, in turn, to a deeper and deeper investigation of the ultimate constituents of matter.

The first CERN collider was the Intersecting Storage Rings (ISR), which accelerated two 30 GeV proton beams in two separate rings of normal magnets. The next accelerator built at CERN was the last of its fixed-target proton machines, the Super Proton Synchrotron (SPS), that, 10 years later, was converted to a proton-antiproton collider. This conversion was made possible by the development of the stochastic cooling technique, that allowed the production of intense high-quality beams of antiprotons. The SPS led to the discovery of the W and Z bosons, the massive carriers of the weak force.

The Large Electron Positron collider (LEP) started operation in 1989 and has provided precision measurements for Standard Model observables. The energy of the e^- e^+ beams has gradually increased in LEP up to the final center-of-mass energy of 209 GeV, in the hope to discover the Higgs boson, the last missing particle in the Standard Model. The benefit of e^- e^+ collisions is that the colliding particles are elementary and the interactions are very clear. The drawback is that leptons are very light and cannot be accelerated to very high energy due to huge synchrotron-radiation energy loss. LEP was shut down November 2, 2000. It will be dismounted and its place in the tunnel will be taken by the LHC.

The LHC is designed to fit into the 27 km LEP tunnel, and will be fed by existing particle sources and pre-accelerators. It will use the most advanced superconducting magnet and accelerator technologies ever employed. The basic layout of the machine, shown in Fig. 1.1, mirrors that of LEP, with eight straight sections each approximately 528 m long, available for experimental insertions or utilities. There are two

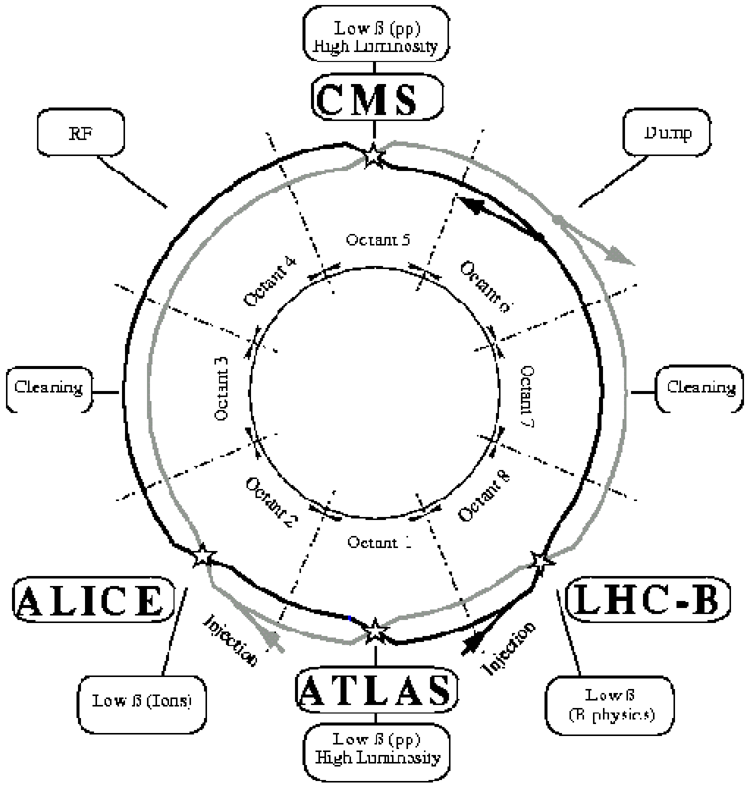

Figure 1.1: Schematic layout of the LHC.

high-luminosity insertions, located at diametrically opposite straight sections, point 1 (ATLAS) and point 5 (CMS). Two more experimental insertions are located at point 2 (ALICE, heavy ions) and point 8 (B physics). These latter straight sections also contain the injection systems. The beams cross from one ring to the other only at these four locations. The remaining four straight sections do not have beam crossings. Insertion 4 contains the RF systems, separate for each beam, while in insertion 3 and 7 there are normal magnets needed to collimate the beam (cleaning). The straight section at point 6 contains the beam dump insertion; the beams are extracted vertically from the machine using a combination of magnets.

The LHC injection system, shown in Fig. 1.2, will use the existing accelerator chain (Linac/Booster/PS/SPS). The protons will be accelerated in the Linac up to

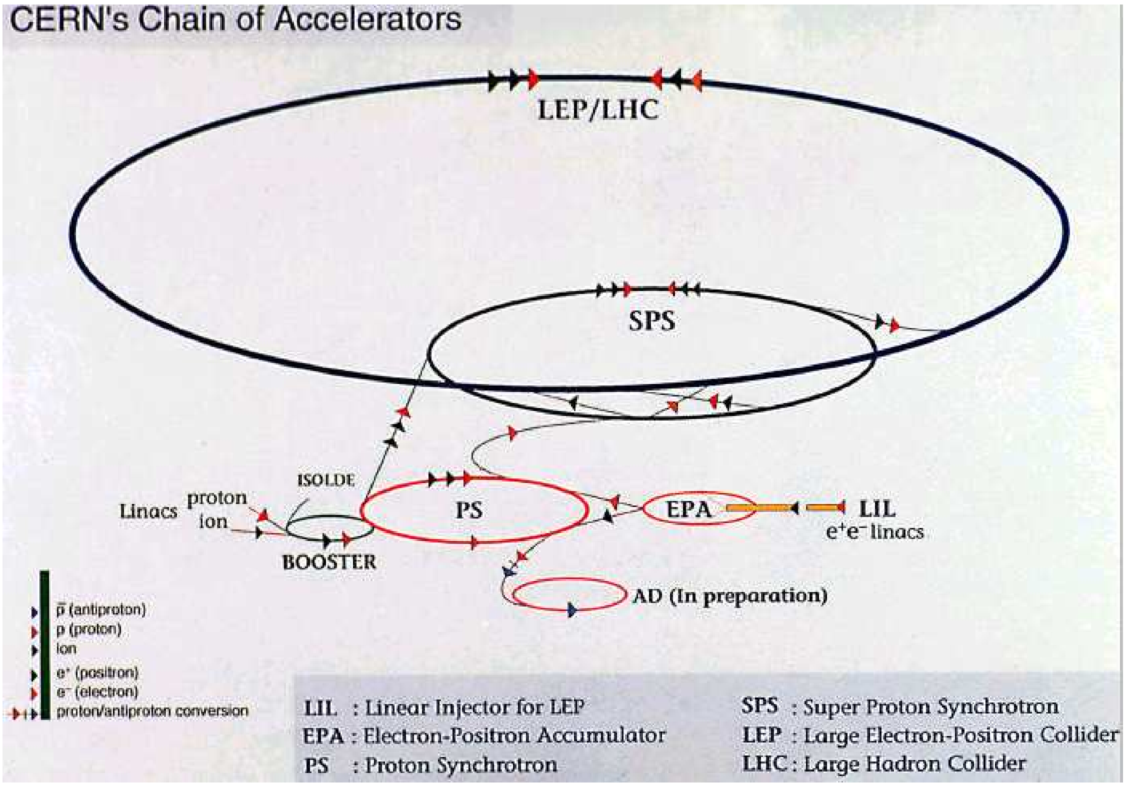

Figure 1.2: Injection scheme for the LHC.

an energy of 50 MeV and then transferred to the PS Booster, where they will reach an energy of 1 GeV. In the PS the protons will be accelerated up to an energy of 26 GeV, transferred in the SPS where, after reaching the energy of 450 GeV, they will be injected in the LHC.

1.1.1 The design concept of the LHC

The LHC is a synchrotron in which bunches of particles are accelerated and kept in a circular orbit by more than one thousand electromagnets. The maximum energy obtainable for the proton beam is determined by the maximum available superconducting dipole fields necessary to bend it in the LHC ring (R=4.5 km). The present technological limit of about 9 T set for the LHC ring a maximum proton beam energy of 7 TeV.

Proton-proton collisions are preferred to proton-antiproton collisions since antiprotons would typically require several hours of accumulation before injection in the LHC. A drawback of this choice, with respect to the choice for SPS and LEP where the same set of magnets was used to keep in orbit particles and antiparticles, is that separate magnetic channels must be used in order to accelerate opposite charged particles. The solution of the problem has been found in a twin-bore magnet, which consists of two sets of coils and beam channels within the same mechanical structure and cryostat, as shown in Fig. 1.3. They lie side by side in the cold yokes of both the 1296 dipole bending magnets and 510 lattice quadrupoles.

The superconducting magnets are the most technologically challenging components of the LHC. Superconductivity is a property that some materials acquire when they are cooled to a low temperature: their resistance to the passage of electrical current virtually disappears. Large currents can flow through small cross-section superconductors, so that compact magnets can be built and operated for much lower cost than conventional magnets made with copper or aluminum conductor. The only energy necessary to produce the superconducting field is the energy dissipated for cooling the magnets. In order to produce the $\sim$9 T dipole field, the LHC magnets must be cooled below 2 K (superfluid He is used as the coolant).

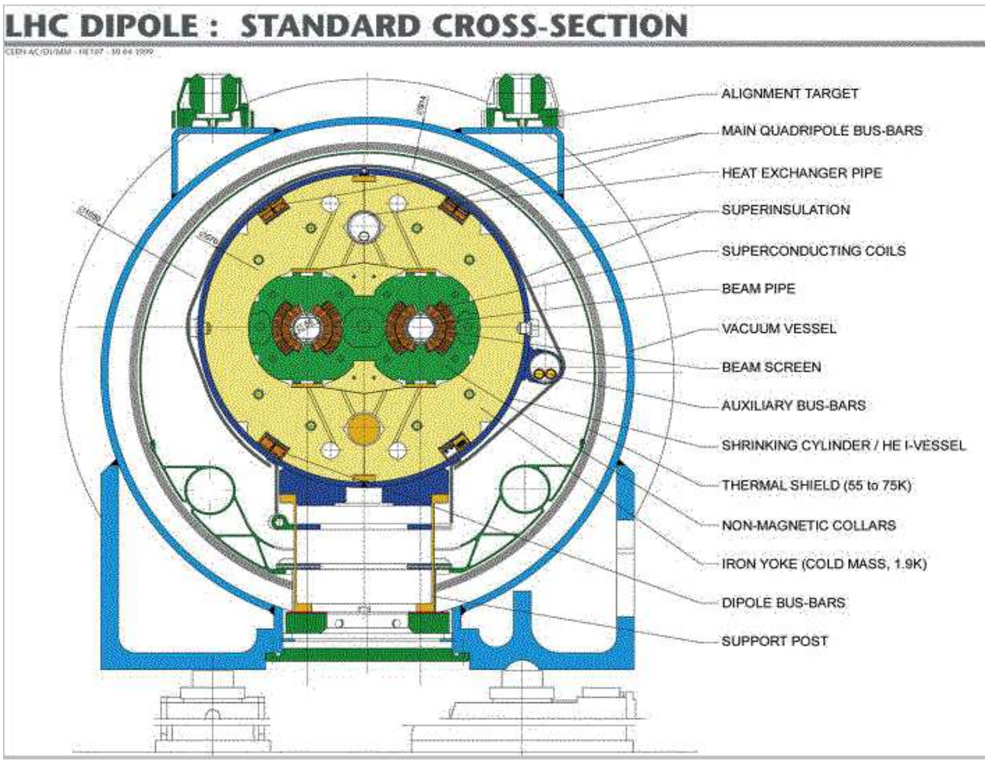

Figure 1.3: Schematic view of a twin-bore magnet for the LHC.

Apart from proton-proton operation, the LHC will also be able to collide heavy-nuclei (Pb-Pb), produced in the existing CERN accelerator complex, giving a center-of-mass energy of 1150 TeV. A peak luminosity of more than $10^{27}cm^{-2}s^{-1}$ can be achieved by turning the existing antiproton ring (LEAR) into an ion-accumulator ring and by applying strong electron cooling.

A very powerful electron-proton collider could also be obtained with the installation of a lepton ring (using existing LEP components) in the free space above the LHC. This would allow to extend to higher energies the studies currently underway at the HERA electron-proton accelerator at DESY.

1.1.2 Performance of the LHC

The main parameters which determine the accelerator's ability to investigate physics processes are the center-of-mass energy and the luminosity. The center-of-mass energy is the energy available for the creation of new particles, while the luminosity (L) determines the rate (R, number of events per second) for a given particle interaction, according to the relation:

$$R = L\sigma_{int} \tag{1.1}$$

where σ_{int} is the interaction cross section.
The performance parameters for p-p operation at the LHC are shown in Tab. 1.1.

Luminosity	10^{34}	$cm^{-2}s^{-1}$
Energy	7.0	TeV
Dipole field	8.4	T
Coil aperture	56	mm
Distance between aperture	194	mm
Injection energy	450	GeV
Circulating current	0.54	A
Bunch spacing	25	ns
Particles per bunch	10^{11}	
Stored beam energy	334	MJ
Normalized transverse emittance	3.75	μm rad
R.m.s. bunch length	0.075	m
β-value at I.P. in collision	0.5	m
Full crossing angle	200	μrad
Beam lifetime	22	h
Luminosity lifetime	10	h
Energy loss per turn	6.7	keV
Critical photon energy	44.1	eV
Total radiated power per beam	3.6	kW

Table 1.1: Main parameters of the LHC.

The cross sections for various processes are shown in Fig. 1.4 as a function of the centre-of-mass energy, for the LHC design luminosity. The working line for the LHC is also shown, and clearly demostrates how the LHC will be able to test new frontiers of physics, not reachable by any other existing machine.

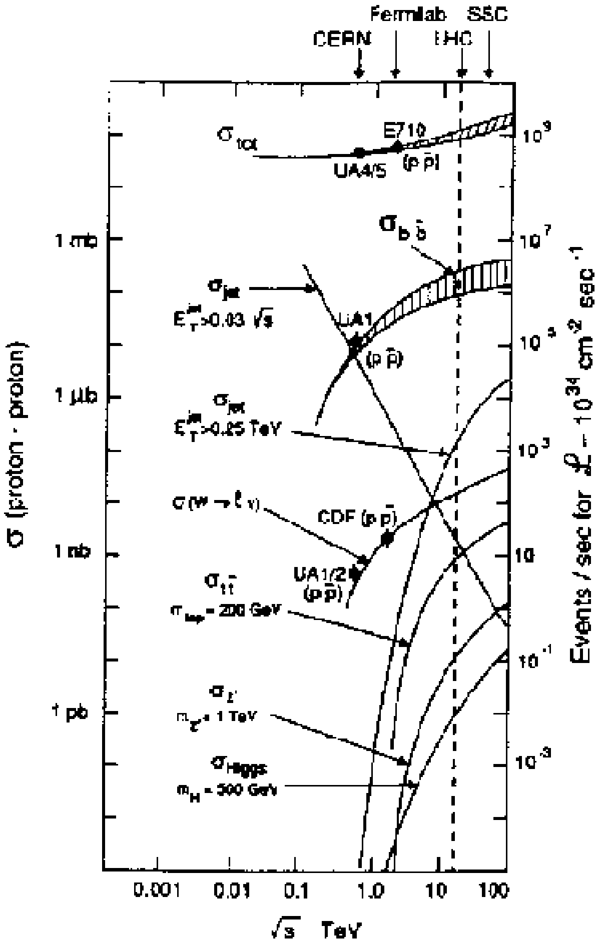

Figure 1.4: Cross-sections for various processes as a function of the center-of-mass energy. The working line for various machine is given. The event rate is also shown, for the LHC nominal luminosity. From [6].

When two bunches, containing n_1 and n_2 particles, collide with frequency f, the luminosity is defined as:

$$L = f\frac{n_1 n_2}{4\pi\sigma_x\sigma_y} \tag{1.2}$$

where σ_x and σ_y characterize the Gaussian transverse profiles in the horizontal (bend) and vertical directions.

The beam size can be expressed in terms of two quantities, namely the transverse emittance (ϵ) and the amplitude function (β) [7]. The transverse emittance is a beam-quality quantity, which depends on bunch-preparation processes. The amplitude function is a beam-optics quantity and is determined by the accelerator-magnets configuration. The dependence of the Gaussian profile of the beam on these two quantities is:

$$\sigma^2 = \frac{\epsilon\beta}{\pi} \tag{1.3}$$

In order to achieve high luminosity, it is therefore necessary to prepare high-population bunches of low emittance, and to make them frequently collide in places where the beam optics provides amplitude-function values as low as possible. The main limitation to the luminosity comes from the so-called beam-beam effect, which tends to extract the periphery of the beam due to the influence of non-linear fields seen by the particles of one beam as they pass through the oncoming bunches of the other. Another constraint comes from the total power delivered to the cold bore of the magnets from synchrotron radiation. This power is negligible with respect to the one dissipated at LEP, but it is nevertheless a problem since it must be absorbed at a temperature of a few Kelvin. This, indeed, is one of the main heat input to the cryogenic system.

At the highest luminosity of the LHC, the stored beam energy will be about 550 MJ. This energy must be absorbed safely at the end of each run or in case of a malfunction or an emergency. Classical beam dumps, made of a central graphite core surrounded by aluminum and iron blocks, and located at the end of two fast extraction channels, have been designed for this purpose.

1.2 LHC experiments

Four detectors will be placed at the LHC intersection points. ATLAS and CMS are the two general purpose experiments, while ALICE and LHCb have a narrowly defined purpose. In the next section ATLAS will be described in detail, with particular emphasis for the Transition Radiation Tracker TRT. In this section the other three experiments are described with particular emphasis on the physics issues they want to address.

1.2.1 ATLAS

The ATLAS detector is described in detail in Chapter 2.

1.2.2 CMS

The CMS (Compact Muon Solenoid) [8] is a general purpose detector. It has been optimized for the search of Standard Model Higgs boson over a mass range from 90 GeV to 1 TeV, but it also allows detection of a wide range of possible signatures from alternative electroweak symmetry breaking mechanisms. CMS is also well adapted for the study of top, beauty and tau physics at lower luminosity and will cover several important aspects of the heavy-ion physics program. CMS has been designed to identify and measure muons, photons and electrons with high precision. At the core of CMS sits a large superconducting solenoid generating a uniform magnetic field of 4 T.

The choice of a strong magnetic field leads to a compact design for the muon spectrometer without compromising the momentum resolution up to $|\eta| < 2.5$, where η is the pseudo-rapidity. The inner tracking system will measure all the high transverse-momentum charged tracks. A high resolution crystal electromagnetic calorimeter, optimized for detection of the two photon decay of an intermediate mass Higgs, is located inside the coil. Hermetic hadronic calorimeters surround the intersection region up to $|\eta| < 4.7$, allowing tagging of forward jets and measurements of missing transverse energies.

1.2.3 LHCb and B physics

LHCb [9] is a detector designed to study B-mesons physics. Since at the LHC B mesons are most likely to emerge in the forward and in the backward directions, the silicon vertex detector sits as close as possible to the beam pipe. The excellent tracking power of the silicon detector in important for an accurate reconstruction of displaced vertices, which are the usual tags for short-lived particles like the B mesons. The Ring Imaging Cherenkov (RICH), another key component of the LHCb detector, provides powerful particle-identification capability over a wide range of momenta.

One of the most important issue that LHCb wants to address is CP violation [7]. CP violation results in a difference in the decay rate of particles and antiparticles. CP violation was first observed in 1964 by Cronin and Fitch in the K_0 system, at the 0.2% level. Several experiments have tried since then to determine the origin and quantify the amount of CP violation in the K_0 system. In the Standard Model (see Section 1.3.1), the amount of CP violation in B decays is not predicted, but it must be experimentally determined. Once the extent of CP violation in one kind of B meson decay has been measured, the result can be fed back into the Standard Model to predict how much CP violation should be seen in all other types of B-meson decays, providing therefore cross-checks for the model. Understanding CP violation is of utmost importance also in cosmology, since it may provide a key to explain the observed unbalance in our universe between matter and anti-matter.

1.2.4 ALICE and quark-gluon plasma

ALICE [10] stands for 'A Large Ion Collider Experiment'. Its goal is to study the so called quark-gluon plasma (QGP). According to the Big Bang cosmology, about 10 μs after the primordial explosion, all the particles which constitute the ordinary matter had yet to form. Temperature and density were so high that quarks and gluons were not yet bound inside the hadrons. This state of matter is the quark-gluon plasma. Evidence for a new state of matter, in which quarks and gluons are not confined, has been claimed in the data from several fixed-target experiment of the CERN's Heavy Ion program. This program will have its natural extension with ALICE. The LHC, in fact, will provide head-on Pb-ion collisions, with an energy of 1150 TeV in the center-of-mass.

The main challenge of heavy-ion physics is to record the enormous number of particles which emerge from the collisions. At CERN present day energies, about 1500 particles are produced in each collision while, at the LHC, this rate will rise up to 50000. A large number of these particles must be tracked and identified, in order to study the evolution from ordinary matter to quark-gluon plasma and back to ordinary matter again.

QGP is also being studied at BNL with the PHENIX and STAR experiments at RHIC, which accelerates gold ions in a 2.4 mile circumference.

1.3 Physics at the LHC

The Standard Model, described in Section 1.3.1, is the theoretical framework that presently best describes our knowledge of elementary particles and their interaction. It is a very successful theory that is presently in agreement with all the experimental results. The only part of the Standard Model that has not yet been tested is the Higgs sector. The so-far-undiscovered Higgs boson is thought to be responsible for the masses of all particles in the model; its discovery is the main goal of the LHC. There is, on the other hand, almost universal agreement that the Standard Model is not the ultimate theory of particle physics. Models beyond the Standard Model are discussed in Section 1.3.2.

1.3.1 The Standard Model

It is well known that Nature is governed by four fundamental interactions. The electromagnetic interaction is responsible for the stability of atoms, the weak interaction for β decays, the strong interaction for binding protons and nucleons inside atomic nuclei, while the gravitational interaction is responsible for the dynamics of celestial bodies.

The Standard Model [11, 12] describes three out of these four interactions. It combines the Weinberg-Salam model of the electromagnetic and weak interactions (successfully unified in the electroweak interaction) and Quantum Chromodynamics, the theory of the strong interaction. Gravity is not included; this suggests that a unified ultimate theory, of which the Standard Model is just a low-energy approximation, is still to be found.

The Standard Model mathematical formalism is based on quantum field theory and on the concept of gauge invariance. Two fermions, the elementary particles that constitute ordinary matter, interact by exchanging a third particle, the so-called gauge boson. These bosons are a consequence of the local gauge invariance applied to the fermion fields and are a manifestation of the symmetry group of the theory, i.e. SU(3)xSU(2)xU(1).

In the Standard Model there are 12 elementary particles (fermions), organized in two groups, quarks and leptons. There are three leptons with a negative unit charge, the electron (e), the muon(μ) and the tau (τ), and three electrically neutral leptons, the neutrinos ν_e,ν_μ and ν_τ. Similarly, there are three families of quarks with electric charge 2/3, up (u), charm (c) and top (t), and three families of quarks with electric charge -1/3, down (d), strange (s) and bottom (b).

The universe in which we live today, is mainly formed by fermions of the first families. The u and d quarks make up protons and neutrons in the atomic nuclei, while electrons circulate in orbits around the nuclei, making the atoms electrically stable. The electron neutrino is an elusive particle, its presence in the β decays is detected by means of missing energy in the reaction. The other two families of fermions are higher mass replications of the first family. Some of the particles of those families (like the muons) can be seen in cosmic rays; others can just be produced with particle accelerators.

The left-handed states for quarks and leptons are doublets under the SU(2) group, while the right-handed states are singlets. The quarks are triplets under the SU(3) group, and carry an additional charge, the so-called color. The leptons, on the other hand, are singlet under the SU(3) group. There is mixing between the three generations of quarks, which is parametrized by the Cabibbo-Kobayashi-Maskawa (CKM) matrix.

The Weinberg-Salam model

The Weinberg-Salam [13, 14] model describes the SU(2)xU(1) group of the electroweak interaction. This group has four generators, from which the gauge bosons originate. There is the photon (γ), which mediates the electromagnetic interaction, and there are the three gauge bosons associated with the weak interaction, namely the neutral Z^0, which is responsible for the neutral weak currents, and the charged W^+ and W^-, which participate in the charged weak currents.

The SU(2)xU(1) group is spontaneously broken by the existence of a postulated Higgs field with a non-zero expectation value. In the theory without the Higgs, all the four gauge bosons would be massless. By interacting with the Higgs field, the Z^0 and the W's acquire a mass, while the γ remains massless: the symmetry is broken. In the Standard Model without the Higgs all the fermions should be massless since they also acquire mass by interacting with the Higgs field. In the simplest version of the model, there is just one degree of freedom in the Higgs sector, which should manifest itself as a neutral scalar boson H^0, presently unobserved.

Quantum Chromodynamics

Quantum Chromodynamics (QCD) is described by the SU(3) symmetry group. There are eight generators of the group. They are represented by eight gluons, which mediate the strong interaction. The gluons carry color charge themselves, and are therefore self-interacting. Quarks of any given flavor exist in three different states of color, namely the red, the green and the blue; observable particles, on the other hand, are colorless combinations of two (q$\bar{\text{q}}$, so-called mesons) or three (qqq, so-called baryons) quarks.

The QCD coupling α_s is small for large momentum transfer (q^2), but is large for small q^2, i.e. at large distances; this leads to the quark confinement inside hadrons. When $\alpha_s \gg O(1)$, perturbative QCD is not reliable and other techniques, like lattice QCD, need to be used.

Successes and weakness of the Standard Model

Many experimental tests of the Standard Model have been performed in recent years, mostly with LEP, but also at SLC and at the Tevatron. Among the biggest successes of the Standard Model, is the prediction of the weak neutral currents, experimentally observed in 1973 at CERN, and the discovery of the three vector bosons Z^0, W^- and W^+.

The results of measurements of Z at LEP have greatly improved the accuracy of the data in the electroweak neutral current sector. The couplings of quarks and leptons to the weak gauge bosons have been measured and found in agreement with Standard Model predictions within a few tenths of one percent. This agreement demonstrates the validity of the theory not only at the lowest order but also at the leading order for the quantum corrections.

The last two fermions predicted by the theory were found recently. The top quark was discovered in 1995 at the Tevatron, while the τ neutrino was directly observed at FNAL in 2000.

Despite its striking successes, it is almost universally accepted that the Standard Model is just a very good low-energy approximation of some more fundamental theory. Among the features not explained by the Standard Model are the very large difference in fermion masses (between m_e and m_{top} there are 7 orders of magnitude), the number of generations, the origin of CP-violation, and the very large number of free parameters of the theory.

In the simplest version of the theory there are 19 free parameters:

- three coupling constants of the gauge theory SU(3)xSU(2)xU(1);
- three lepton and six quark masses;
- the mass of the Z boson, which sets the scale of the weak interaction;
- four parameters (three angles and a phase) which describe the rotation from the weak to the mass eigenstates of the charge -1/3 quarks (CKM matrix);
- a CP-violating parameter associated with the strong interaction (supposed to be exceedingly small);
- the mass of the Higgs boson.

The so-called hierarchy problem is the most fundamental problem with the Standard Model. It is related to the presence of divergences in quantum corrections to particle masses. Chiral symmetry prevents quantum corrections to fermion masses from being more than logarithmically divergent. The Standard Model Higgs boson, on the other hand, does not have any symmetry to protect its mass, which is therefore subjected to quadratically divergent quantum corrections. Since the quantum corrections shouldn't be more important than the bare value, in order for the theory to make any sense, the theory is valid just up to a cut-off value Λ, which is on the order of one TeV.

1.3.2 Beyond the Standard Model

Two kind of models have been proposed in order to solve the hierarchy problem. In the 'composite models', the Higgs boson is not regarded as an elementary particle but rather as a bound state of fermions or as a condensate, due to a new strong force so far unknown. A variety of new hadrons should appear in the LHC energy range. The most appealing examples for this kind of model are technicolor theories [15].

'Supersymmetric models' (SUSY), on the other hand, treat the Higgs boson(s) as fundamental object(s) and introduce a symmetry betwen fermions and bosons. For any Standard Model particle of spin s there is a correspondent SUSY partner with spin $s-1/2$. Supersymmetry is clearly broken, since SUSY particles have not yet been observed, but their masses are predicted to be in the LHC energy range. These SUSY particles have couplings which allow exact cancellation of the quadratic divergences, providing therefore a very elegant solution of the hierarchy problem. SUSY preserves all the virtues of the Standard Model, the necessary SUSY breaking can be introduced through soft terms that do not spoil the good convergence property of the theory.

The simplest SUSY model is the Minimal Supersymmetric Standard Model (MSSM), which predicts the existence of two Higgs doublets. After spontaneous symmetry breaking, five physical Higgs particles are left:

- two neutral scalar bosons, h^0 and H^0;
- one neutral pseudo-scalar boson, A^0;
- two charged bosons, H^+ and A^-.

Grand Unified Theories [16] (GUT) aim towards the unification of the electroweak and the strong forces at energy scales of $M_{GUT} \sim 10^{14} - 10^{16} GeV$, close to the Planck scale of quantum gravity, $M_{Plank} \sim 10^{19} GeV$. Gravity could also be included, superstrings [17] provides the best attempt at such a theory.

Phenomenological evidence of a SUSY Nature comes from extrapolations of the values of the coupling constants to very high energy [18]; the unifications of couplings is possible in GUT's theories only if SUSY particles are taken into account.

Chapter 2

The ATLAS experiment

ATLAS (A Toroidal LHC ApparatuS) [19] is one of the two general purpose detectors for the LHC. It is designed to exploit the full discovery potential of the LHC.

The main physics goal that has led to the design of the ATLAS detector is the discovery of the Higgs boson, and more generally the investigation of the origin of mass at the electroweak scale. The ATLAS detector was therefore designed to be sensitive to the largest possible Higgs mass, providing as many signatures as possible for its detection, like high transverse momentum (p_T) leptons (both electrons and muons), photons, jets and missing transverse energy (E_{Tmiss}). In the high-rate environment of the LHC, this variety of signatures will allow robust and redundant physics measurements with an ability of internal cross-checks. The same signatures are believed to be present in several possible interesting physics processes beyond the Standard Model, like in the Supersymmetric models. Other important goals of the ATLAS experiment are the searches for heavy W and Z-like objects, for supersymmetric particles, for compositeness of the fundamental fermions, and detailed study of the top quark.

During the initial lower-luminosity running, ATLAS will mainly study B-meson decays, which allow the investigation of CP violation. For these studies, ATLAS will use more complex signatures such as tau-lepton detection and heavy-flavor tags from secondary vertices.

The main analysis work of this thesis (discussed in detail in Chapters 4-6) is important for B-physics studies, since it shows how some hadron identification may be possible using time-over-threshold information from straw tubes of the Transition Radiation Tracker.

2.1 The ATLAS detector

Detailed Monte Carlo simulations of benchmark processes, selected either for their relevance in the SM or for their occurrence in alternative models, have been studied and used to set basic criteria for the ATLAS detector design:

- Very good electromagnetic calorimetry for electron and photon identification and measurements, complemented by full-coverage hadronic calorimetry for accurate jet and E_{Tmiss} measurements;
- High-precision muon-momenta measurements, with the capability to guarantee accurate momentum measurements at the highest luminosity using the external muon spectrometer alone;
- Efficient tagging at high luminosity for high-p_T lepton measurements, electron and photon identification, tau-lepton and heavy-flavor identification, and full-event reconstruction at lower luminosity;
- Large acceptance in pseudorapidity (η) with almost full azimuthal angle (ϕ) coverage everywhere;
- Triggering and measurements of low-p_T particles, providing high efficiency for most physics processes of interest at the LHC.

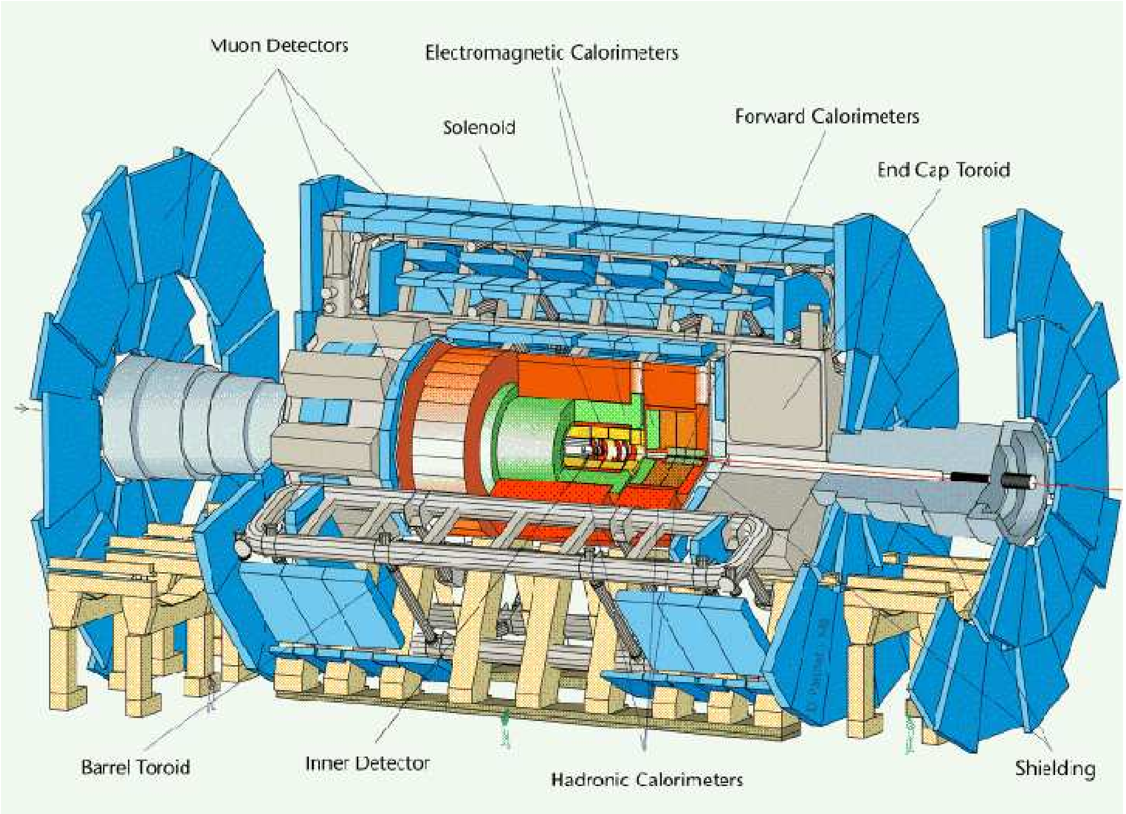

Figure 2.1: The ATLAS detector.

The overall detector layout is shown in Fig. 2.1. The magnet configuration, described in more detail in Section 2.2, is based on an inner thin superconducting magnet surrounding the inner detector cavity, and large superconducting air core toroids consisting of independent coils arranged with an eight-fold symmetry outside the calorimeters.

The inner detector, described in detail in Section 2.3, is contained within a cylinder of length 7 m and a radius of 1.15 m, in a solenoidal magnetic field with a nominal value of 2 T. Pattern recognition, momentum and vertex measurements, and electron identification are achieved with a combination of discrete high-resolution semiconductor pixel and strip detectors in the inner part of the tracking volume, and a continuous straw tube tracking detector with transition-radiation capability in its outer part.

The calorimeter system, discussed in more detail in Section 2.4, surrounds the inner detector cavity. It is composed of an inner electromagnetic and an outer hadronic component. A high-granularity lead/Liquid Argon (LAr) electromagnetic sampling calorimeter (ECAL), with excellent performance in terms of energy and position resolution, covers the range $|\eta| < 3.2$. In the end-caps, the LAr technology is also used for the hadronic calorimeters (HAC), which share the cryostats with the ECAL end-caps. The same cryostats also house the special LAr forward calorimeters which extend the coverage up to $|\eta| = 4.9$. The bulk of the HAC is provided by a novel scintillator tile calorimeter, which is separated into a large barrel and two smaller extended barrel cylinders, one on each side of the barrel. The LAr calorimeter is contained in a cylinder with an inner radius of 2.25 m and extends longitudinally to $\sim$ 6.65 m along the beam axis. The outer radius of the scintillator tile calorimeter, whose support integrates the solenoid flux-return iron yoke, is 4.25 m and its half-length is 6.10 m.

The calorimeter is surrounded by the muon spectrometer, described in Section 2.5. The air-core toroid system, with a long barrel and two inserted end-cap magnets, generates a large magnetic field volume with strong bending power within a light and open structure. Multiple scattering effects are thereby minimized, and excellent muon-momentum resolution is achieved with three stations of high-precision tracking chambers. The muon instrumentation also includes trigger chambers with very fast time response. The muon spectrometer defines the overall dimensions of the ATLAS detector. The outer chambers of the barrel are at radius of about 11 m and the third layer of the forward muon chambers, mounted on the cavern wall, is located about 23 m from the interaction point. The overall weight of the ATLAS detector is about

7000 tons.

2.2 Magnet System

The magnet system in ATLAS, shown in Fig. 2.1, is formed by a central solenoid (CS), that provides magnetic field to the inner detector, and an outer arrangement of three large air-core toroids (a barrel toroid (BT) and two end-cap toroids (ECTs)) generating magnetic field for the muon spectrometer.

The solenoid is a superconducting magnet, kept at 4.5 K, placed inside the LAr calorimeter. This configuration requires a careful minimization of the material in order to achieve the desired calorimeter performance. Therefore the CS and the LAr calorimeter share one cryostat, thus saving two cryostat walls. To minimize material further, the solenoid is considerably shorter than the inner detector (2.65 m versus 3.40 m half-length), producing some non-uniformity in the magnetic field along the z-direction. The solenoidal field, in fact, drops from the nominal value of 2 T at the interaction point to a value of about 0.5 T at the end of the inner detector.

The toroid system is designed to produce a large-volume magnetic-field coverage in the range $0< |\eta| < 2.7$. Its open structure minimizes the contribution of multiple scattering to the momentum resolution. The BT extends over a length of 25 m with an inner bore of 9.4 m and an outer diameter of 20.1 m. The two ECTs are inserted in the barrel at each end. The ECTs have a length of 5 m, an inner bore of 1.65 m and an outer diameter of 10.7 m.

Each toroid consists of eight flat coils assembled radially and symmetrically around the beam axis. The ECT coils are rotated in azimuth by an angle of 22.5 ° with respect to the BT coils to provide for radial overlap and to optimize the bending power in the transition region between the two toroids. The BT coils are contained in individual cryostats, held rigidly together in a support frame. The eight coils of each ECT are assembled in a single large cryostat.

The performance in terms of bending power is characterized by the field integral $\int B \cdot dl$, where B is the azimuthal field component and the integral is taken on a straight line trajectory between the inner and outer radius of the toroids. The toroidal bending power is shown in Fig. 2.2, which shows that the bending power is lower in the transition region.

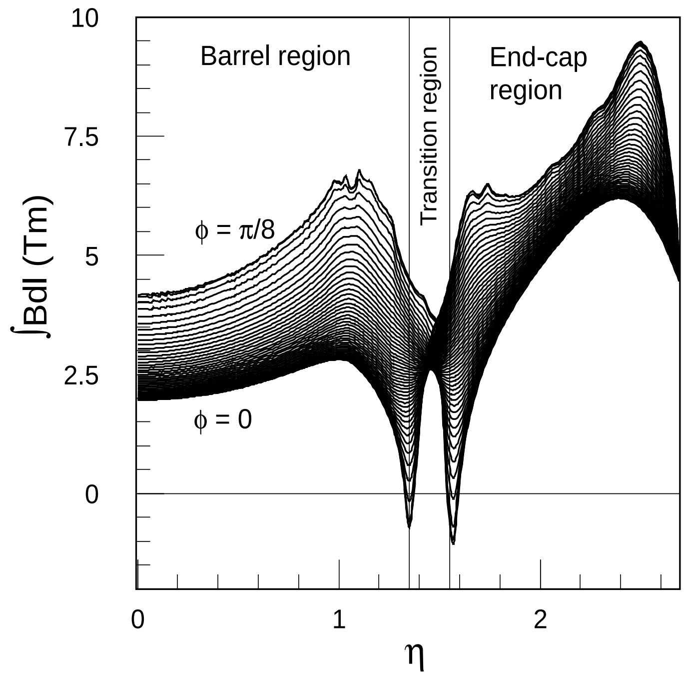

Figure 2.2: Toroidal bending power.

2.3 Inner Detector

The inner detector combines high-granularity silicon detectors (using both pixel and micro-strip technologies) with continuous tracking elements (straw tubes), and is contained in a 2 T solenoidal magnet. The layout of the inner detector is shown in Fig. 2.3. The outer radius of the inner detector cavity is 115 cm, fixed by the inner dimension of the cryostat containing the LAr ECAL calorimeter, and the total length is 7 m, limited by the position of the end-cap calorimeters. Mechanically, the inner detector consists of three units: a barrel part extending over ± 80 cm and two identical end-caps covering the rest of the cylindrical cavity. The precision tracking elements are contained within a radius of 56 cm, followed by the continuous tracking and finally the general support and service region at the outermost radius.

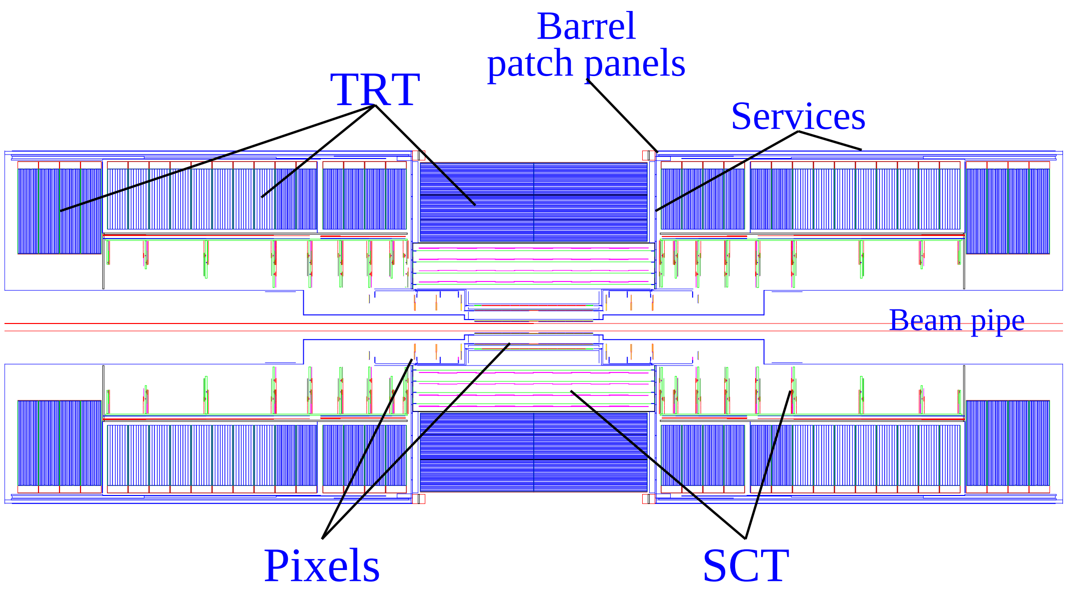

Figure 2.3: The Inner Detector layout.

The inner detector is designed to provide a very robust pattern recognition, high precision in both z and ϕ coordinates, good momentum and vertex resolution as well as electron identification. The very large track density expected at the LHC requires high-granularity detectors at the inner radii in order to achieve good momentum and vertex resolution.

The silicon pixel detector is formed by three pixel layers, which gives three high-resolution space points per track, and is placed as close as possible to the beam pipe. The innermost layer, also called the B layer, is placed at 4 cm from the interaction point.

The silicon microstrip detector (SCT) surrounds the pixel detector, and is composed by eight SCT layers, which give four space-points per track. The total number of precision layers is limited because of the material they introduce and because of their cost.

At the outer radii a large number of position measurements (on average 32 per track) is provided by the straws of the Transition Radiation Tracker (TRT), which provides continuous tracking at very low cost, and in addition provides electron identification capability.

2.3.1 Pixel detector

The pixel detector is located in the innermost region of the inner detector. It is a very high-granularity detector, composed of more than 140 million pixels, that has been designed to provide excellent pattern recognition; it determines the impact-parameter resolution and the ability of the inner detector to find very short-lived particles, such B hadrons and τ leptons.

Each track will cross at least three pixels, resulting in three high-precision space-points. The pixel dimensions are 50 x 300 μm. The occupancy, due to the very high granularity, is extremely low: only about one pixel out of ten thousand gives a signal at the LHC design luminosity. For a single pixel, the spatial resolution is on average $\sigma_{r\phi} \sim 14\,\mu$m and $\sigma_z \sim 87\,\mu$m, and it can be improved by studying how the charges are shared between neighbors.

The pixels are organized in modules, identical in the barrel and in the end-caps. Each module is 62.4 mm long and 21.4 mm wide for a total of 61440 pixel elements read out by 16 chips. The readout chips, bump-bonded to the detector, contain individual circuits for each pixel element, including buffering to store the data during the level one trigger latency (see Section 2.6). The barrel part is formed by three layers of modules, at average radii of 4, 10 and 13 cm, while the end-caps are formed by 5 disks of modules on each side, between radii of 11 and 20 cm.

2.3.2 Semiconductor tracker (SCT)

The SCT covers the intermediate radial range of the inner detector. It provides eight precision measurements (four space points) per track over the full rapidity coverage, contributing to the momentum, impact-parameter and vertex-position measurement.

The basic element is a 6.36 x 6.40 cm^2 single side p-on-n silicon detector, with 768 readout strips of $80\,\mu$m pitch. The spatial resolution is on average $\sigma_{r\phi} \sim 16\,\mu$m and $\sigma_z \sim 550\,\mu$m. The occupancy is around 1%.

Each barrel module consists of four elements. On each side of the module, two detectors are wire-bonded together to form 12.8 cm long strips. Two of such detector pairs are then glued together back-to-back at a 40 mrad angle, separated by a heat transport plate; the electronics is mounted above the detector. The readout chain consists of a front-end amplifier and discriminator, followed by a binary pipeline which stores the hits above threshold during the level one trigger latency. The end-cap modules are very similar in design but use tapered strips (one set aligned radially), whose length, varying between 6 to 12 cm, has been chosen in order to optimise the η-coverage. The barrel modules are mounted on carbon-fiber cylinders which carry the cooling system. Four complete barrel layers, linked together, are located between radii of 30.0 and 52.0 cm. The end-cap modules are mounted into nine wheels, and interconnected by a space-frame.

2.3.3 Transition Radiation Tracker (TRT)

The TRT is described in detail in Chapter 3.

2.4 Calorimetry

Calorimeters are composite detectors that measure the energy and position of incident particles and jets, which are usually absorbed in the process. Each calorimeter is made of multiple individual cells, over whose volume the absorbed energy is integrated; cells are aligned to form towers. The analysis of cells and towers permits to measure lateral and longitudinal shower profiles.

Typically, incident electromagnetic particles, i.e. electrons and photons, are fully absorbed in the ECAL, the innermost electromagnetic part of the detector. The relatively short and concentrated electromagnetic shower make it possible to build a compact ECAL. Incident hadrons, on other hand, may start showering in the ECAL, but they will be fully absorbed only in the outer part of the detector, the hadronic calorimeter (HAC).

The calorimeters also provide signatures for particles that are not absorbed, like muons and neutrinos. Muons do not shower, but they leave an ionization signal. Neutrinos, on the other hand, leave no signal, but their presence can be inferred by energy conservation: in an hermetically closed calorimeter the passage of a neutrino can be 'observed' by detecting missing transverse energy.

In ATLAS, the calorimetry consists of an ECAL covering the pseudorapidity region $|\eta| < 3.2$, a barrel HAC covering $|\eta| < 1.7$, an end-cap HAC covering $1.5 < |\eta| < 3.2$, and forward calorimeter covering $3.1 < |\eta| < 4.9$.

The ECAL is a lead/liquid argon sampling calorimeter with accordion geometry. The structure of the barrel accordion ECAL is shown in Fig. 2.4. Over the range

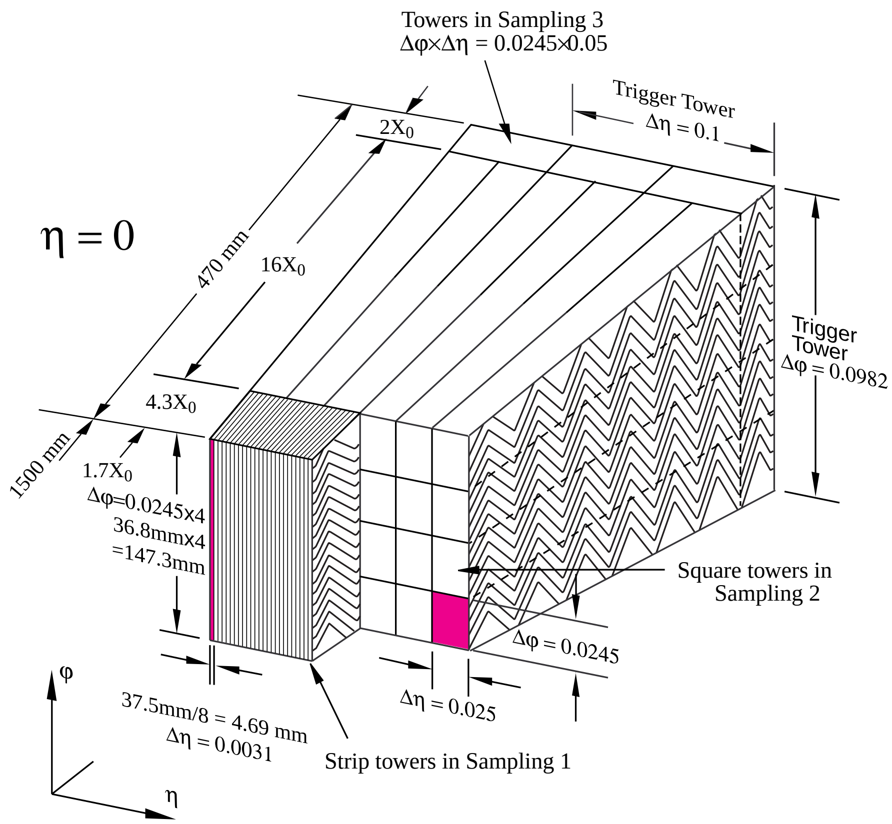

Figure 2.4: The structure of the barrel accordion calorimeter.

$|\eta| < 1.8$ it is preceded by a presampler, installed immediately behind the cryostat cold wall and used to correct for the energy lost in the upstream material (inner detector, cryostats, coil).

The barrel HAC is a cylinder divided into three sections: the central barrel and two identical extended barrels. It is based on sampling technique with plastic scintillator plates (tiles) embedded in an iron absorber. At large η, where higher radiation resistance is needed, the intrinsically radiation-hard LAr technology is used for all the calorimeters: the HAC end-caps, a copper LAr detector with parallel plate geometry, and the forward calorimeter, a dense LAr calorimeter with rod-shaped electrodes in a tungsten matrix. The barrel ECAL is contained in the barrel cryostat, which surrounds the inner detector cavity. The solenoid, which supplies the 2 T magnetic field to the inner detector is integrated into the vacuum of the barrel cryostat and is placed in front of the ECAL. Two end-cap cryostats house the end-caps ECAL and HAC, as well as the integrated forward calorimeter. The barrel and extended barrel tile calorimeter support the LAr cryostats and also act as the main solenoid flux return.

The energy resolution in the electromagnetic calorimeter can be expressed as:

$$\frac{\sigma}{E} \sim \frac{a}{\sqrt(E)} \otimes \frac{b}{E} \otimes c$$

The term a ($\sim 10\%$) is determined by the statistical fluctuations in the shower development; it decreases with increasing energy, and dominates the energy resolution over most of the useful range in the calorimeter. The term b ($\sim 400\,MeV$) is due to instrumental effects, like electronic noise and pedestal effect, and dominates at low energy. The term c ($< 0.7\%$), the constant term, sets the limit at very high energy and is due to calibration errors and non-uniformities of the calorimeter.

2.5 Muon system

High-momentum final-state muons are among the most promising and robust signatures of interesting physics at the LHC. To exploit this potential ATLAS will use a high-resolution muon spectrometer with stand-alone triggering and momentum measurement capability over a wide range of transverse momentum, pseudorapidity and azimuthal angle. The muon system design fulfills the following conditions:

- A transverse-momentum resolution of 1% in the low p_T region. This limit is set by the requirement to detect the H $\rightarrow$ ZZ* decay in the muon channel with a high suppression of the background.
- At the highest p_T the muon system should have sufficient momentum resolution to give good charge identification for Z' $\rightarrow \mu\mu$ decay.
- A pseudorapidity coverage $|\eta| < 3$. This condition guarantees a good detection efficiency for high-mass objects decaying to muons with all muons within the acceptance region.
- A hermetic system to prevent particles escaping through holes.
- Measurement of spatial coordinates in two dimensions to provide good mass resolution.
- A low rate of both punch-through hadrons and fake tracks.
- A trigger system for almost all physics channels. The requirement on pseudorapidity coverage is similar to the requirement for the main muon system. For B physics a maximal coverage for muons with transverse momentum down to 5 GeV is desirable.

The layout of the muon spectrometer is shown in Fig. 2.5. It is based on the magnetic deflection of muon tracks in the toroidal field described in Section 2.1, and it is instrumented with separate trigger (shown in Fig. 2.6) and high precision tracking chambers.

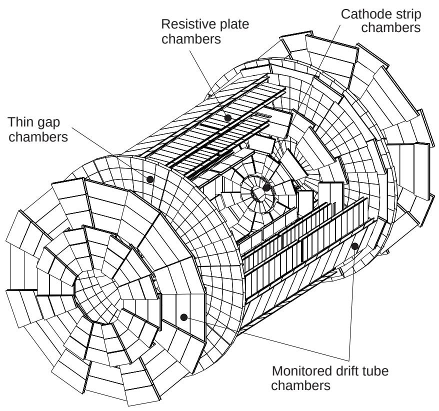

Figure 2.5: The muon spectrometer.

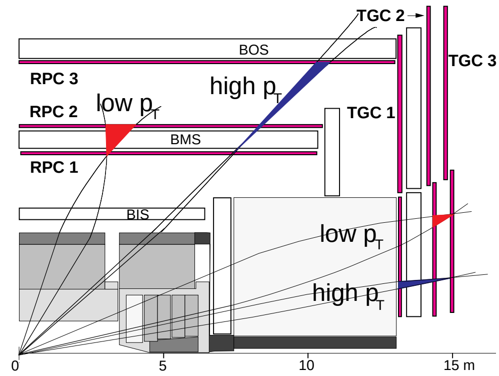

Figure 2.6: Trigger chambers.

The detector has been designed in such a way that a track will cross three high-precision stations for all η. In the barrel region these chambers are arranged in cylindrical layers around the beam axis while in the transition and end-cap regions the chambers are installed vertically. In the barrel region one set of chambers is placed inside the magnetic field, while the other two are outside, near the inner and outer field boundaries, in order to determine the momentum from the sagitta of the trajectory. In the end-caps, where the toroid cryostat prevents chambers from being placed inside the magnetic field, the muon momentum is measured from a point-angle measurement.

Over most of the pseudorapidity range, a precision measurement of the track coordinates in the principal bending direction of the magnetic field is provided by Monitored Drift Tubes (MDTs). At large η and close to the interaction point, Cathode Strip Chambers (CSCs) with higher granularity are used to sustain the demanding rate and background conditions.

The trigger system covers the range $|\eta| < 2.4$. Resistive Plate Chambers (RPCs) are used in the barrel and Thin Gap Chambers (TGCs) in the end-cap region. Both types of trigger chambers also provide a second measurement of the track coordinates orthogonal to the precision measurement, in a direction approximately parallel to the magnetic field lines. The trigger chamber layout is shown in Fig. 2.6.

2.5.1 Monitored Drift-Tube chambers

The MDT chambers are proportional chambers made of aluminium tubes of 30 mm diameter and length varying from 70 cm to 630 cm. The anode is 50 μm W-Re wire and the gas mixture is 93% Ar 7% CO_2. The maximum drift time is about 700 ns and the single wire resolution is about 80 μm. To improve the resolution of the chamber beyond the single wire limit and to achieve adequate redundancy for pattern recognition, the MDT are constructed from multilayer pairs of three (middle and outer station) or four (inner layer) monolayer, placed on opposite side of a rigid support structure. The support structures allow an accurate positioning of the drift tubes with respect to each other, for mechanical integrity under effects of temperature and gravity, and are also part of the alignment system.

2.5.2 Cathode Strip Chambers

The CSC's are multiwire proportional chambers with a wire spacing of 2.5 mm. The gas mixture is 30% Ar% 50 CO_2 20% CF_4. The maximum drift time is 30 ns. Cathode strips arranged perpendicularly to the anode wires give a second coordinate in the readout which, together with the finer granularity compared to the MDT's, make it possible to find tracks in the forward region, where the track density is higher compared to the barrel region. This second coordinate is obtained by measuring the charge induced on the cathode by the avalanche formed on the anode wire. Good spatial resolution is achieved by segmentation of the readout cathode and by charge interpolation between neighboring strips. The cathode readout pitch is 5.08 mm. A measurement of the transverse coordinate is obtained from orthogonal strips, i.e. oriented parallel to the anode wires, which form the second cathode of the chamber. Position resolution better than 60 μm has been measured in several prototypes.

2.5.3 Resistive Plate Chambers

The RPC is a gaseous detector providing an excellent space-time resolution, typically of the order of 1 cm x 1 ns, with digital read-out. The basic RPC unit is a narrow (2 mm) gas gap formed by two parallel resistive bakelite plates, separated by insulating spacers. The primary ionization electrons are multiplied into avalanches by a high uniform electric field, typically 4.5 kV/mm. The gas mixture is based on $C_2H_2F_4$ with small admixture of SF_6. The signal is read out via capacitive coupling by metal strips on both sides of the detector. A trigger chamber is made from two rectangular detector layers, each one read out by two orthogonal series of pick-up strips: the 'η strips' are parallel to the MDT wires and provide the bending view of the trigger detector; the 'ϕ strips', orthogonal to the MDT wires, provide the second coordinate measurement which is also required for offline pattern recognition.

2.5.4 Thin Gap Chambers

The TGCs are similar in design to the CSCs, with the difference that the anode-wire pitch is larger than the anode-cathode distance. Signals from the anode wires, arranged parallel to the MDT wires, provide the trigger information together with readout strips arranged orthogonal to the wires. These readout strips are also used to measure the second coordinate.

Operated with a highly quenching gas mixture of 55% CO_2 and 45% n-pentane (n-C_5H_{12}) this type of cell geometry permits operation in saturated mode.

2.6 Trigger and data-acquisition system

The bunch crossing rate at the LHC is 40 MHz. At the design luminosity of $10^{34}\,cm^{-2}s^{-1}$, the expected interaction rate is about 1 GHz. The trigger system is designed to reduce this rate by a factor 10^7, down to the 100 Hz rate acceptable by the data-acquisition (DAQ) system for permanent storage. The interesting physics processes must clearly be accepted with high efficiency, while the overwhelming minimum bias events (events with many low p_T hadrons resulting from fusion processes of gluons or quarks with a small energy transfer) must be very efficiently rejected. The trigger/DAQ system is schematized in Fig. 2.7.

The level-1 (LVL1) trigger makes an initial selection based on reduced-granularity information from the muon trigger chambers and the calorimeters. The LVL1 trigger latency (the time taken to form and deliver the LVL1 trigger decision) is less than 2.5 μs (during this time the data from all the sub-detectors are stored in pipeline memories) and reduces the event rate to about 75 kHz, a value that is acceptable by all the ATLAS front-end systems. The LVL1 trigger searches for several interesting signatures. The RPCs and TGCs trigger chambers are used to identify high-p_T muons, while high-p_T electrons and photons, jets and τ-leptons decaying into hadrons are searched for in reduced granularity regions (towers) in the calorimeter. Information from large missing and total transverse energy, calculated by summing over trigger towers in the calorimeter, is also used at the LVL1 trigger.

Events accepted by the LVL1 trigger are read-out from the front-end electronics systems of the detector into readout drivers (RODs) and then transferred into readout

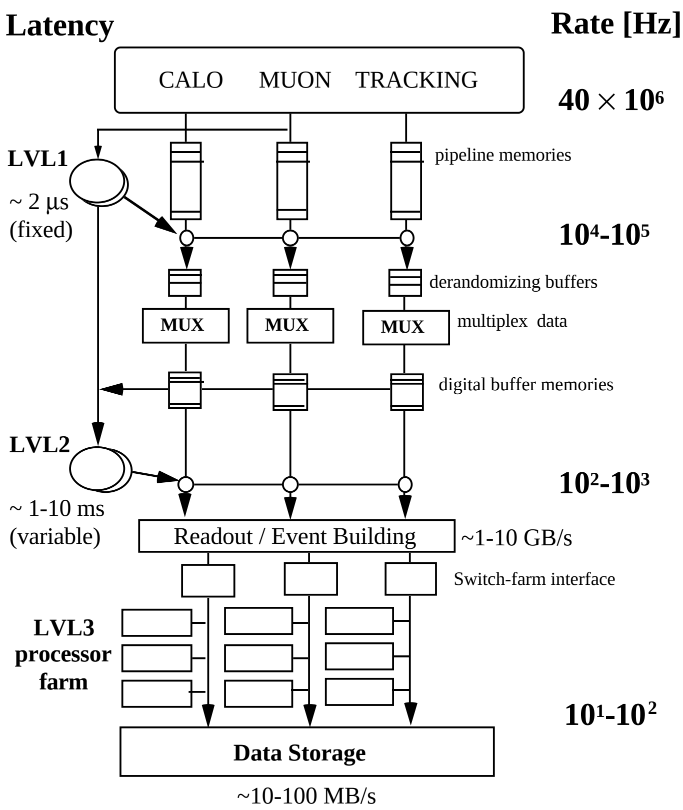

Figure 2.7: Block diagram of the Trigger/DAQ system

buffers (ROBs). Intermediate buffers, called derandomizers, average out the high istantaneous data rate at the output of the pipeline memories to match the available input bandwidth of the RODs. The data for the bunch crossing selected by the LVL1 trigger are held into the ROBs during the LVL2 trigger latency (expected in the range 1-10 ms). The trigger rate is reduced by LVL2 to about 1 kHz.

The LVL2 trigger uses 'region-of-interest' (RoI) information provided by the LVL1 trigger, such as the position (η and ϕ), the p_T of candidate objects and energy sums, and uses information from all the sub-detectors. In case of a muon trigger, the additional rejection power due to the LVL2 comes from a sharpening of the p_T threshold, using also information from the precision muon chambers and the inner detector, and from the requirement for the muon to be isolated, using calorimeter information around a narrow region around the muon candidate. For isolated electrons, rejection power at the LVL2 comes from using the full granularity calorimeter information, from the requirement of a matching high-p_T charged track in the inner detector, and from the use of transition-radiation information of the TRT. For photons, additional rejection power is limited by the relatively high probability for photon conversion in the inner detector material, so the use of the inner detector is not allowed. For the hadron/τ trigger, a localised isolated hadronic calorimeter cluster with a matching high-p_T inner detector track is required.

If the event is accepted by LVL2, the data is transferred by the DAQ system to the Event Filter (EF), which constitutes the LVL3 trigger. The process of moving the data from the ROBs to the EF is called the event builder. The EF employs offline algorithms and methods, using up to date calibration and alignment information such as the magnetic field map. Most of the rejection power of the EF, that reduces the rate to 100 Hz, comes from the use of complex algorithms and criteria which, because of processing time limits, cannot be performed at LVL2, such as vertex and track fitting using bremsstrahlung recovery for electrons.

Chapter 3

The Transition Radiation Tracker

The Transition Radiation Tracker (TRT) [20] is a part of the Inner Detector of the ATLAS experiment. It has been designed to provide excellent pattern recognition capabilities as well as electron identification via transition radiation. The TRT is a straw drift tube detector, with a central barrel section and two end-cap sides, that will give an average of 35 crossed straws per track. In the barrel TRT, axial straws are embedded in fiber radiators, while in the end-cap layers of radial straws and foil radiators are alternated. These geometries are chosen to maintain an approximately constant number of straws crossed by tracks with $p_T > 0.5\,\text{GeV}$ over the full pseudorapidity coverage ($|\eta| < 2.5$).

The straw technology is particularly suitable for high-luminosity hadron colliders, given its relatively low cost for tracking over large volumes and its intrinsic radiation hardness. Many years of R&D work, detailed Monte Carlo simulations and test-beam measurements, performed also with large-scale prototypes, give confidence that the TRT will operate and perform reliably in the harsh LHC environment.

The TRT detector is described in Section 3.1, while the expected performance is outlined in Section 3.2. The basic principles of operation of a TRT straw tube are given in Section 3.3, as well as its performance and the front-end electronics requirement. The design and the assembly procedures for the construction of a barrel module is described in detail in Section 3.5, while the barrel TRT electronics is discussed in Section 3.6.

3.1 Detector Description

The TRT consists of a barrel part and two end-cap sides. The perspective view of the TRT layout is shown in Fig. 3.1, while the schematic view of the TRT detector in the R-z plane is shown in Fig. 3.2.

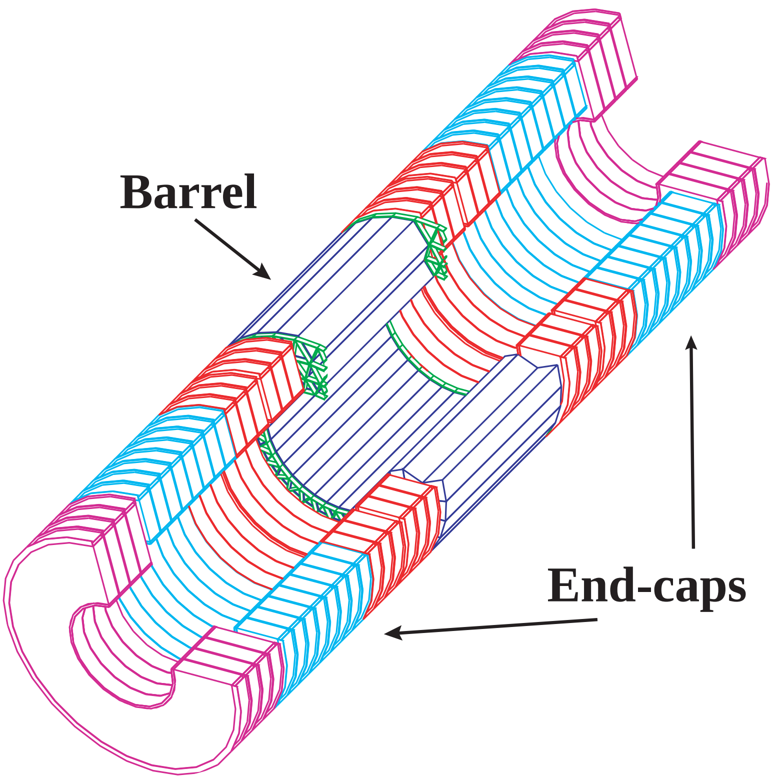

Figure 3.1: Perspective view of the TRT layout. The barrel modules and the end-cap wheels are shown, as well as the barrel assembly frame.

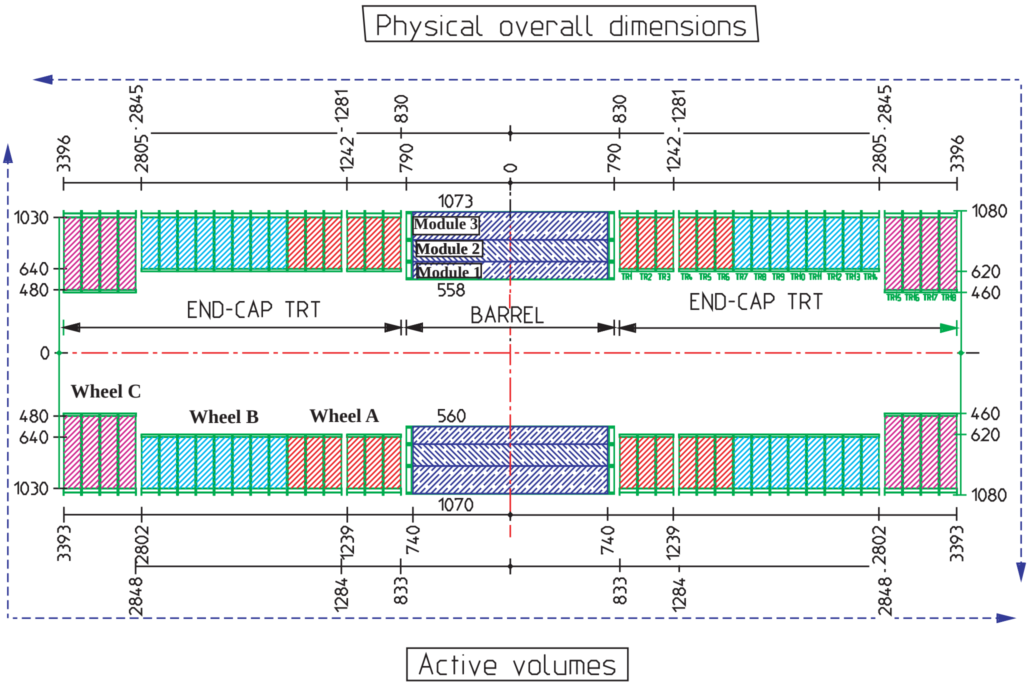

Figure 3.2: Schematic view of the TRT detector in the R-z plane. The main dimension of the detector are shown on the left (resp. right) hand side for the active detector volume (resp. the physical detector envelopes). Units are in mm.

The barrel part consists of three cylindrical rings, each containing 32 identical and independent modules. The three types of modules contain respectively 329 (type I modules, at the innermost radii), 520 (type II modules, at the middle radii) and 793 straws (type III modules, at the outermost radii). In the barrel, the straws are $\pm$ 70 cm long, placed axially with respect to the beam and are embedded in fiber radiator. In the end-caps the straws are shorter (between 39 cm and 55 cm) and are placed radially.

Each of the two end-caps consists of three sets of identical and independent wheels. In the wheels straws and radiator layers are alternated. In order of increasing distance from the interaction point they are: the type-A wheel (6 wheels with 12288 straws each), the type-B wheel (8 wheels with 6144 straws each) and the type-C wheels (4 wheels with 9216 straws each). The type-C wheels extend towards the beam pipe more than the other type of wheels, in order to maintain an approximately constant number of straws crossed by a track also at large η.

The detector modularity (both for barrel and end-caps) simplifies the assembly procedures and minimizes at every stage the number of straws affected by any failure in the overall system. The engineering envelopes of the TRT modules are larger than the active modules, as can be seen, for example, in Fig. 3.2 in the barrel region between z=740 mm (edge of the active volume) and z=790 mm (edge of the engineering envelope). This accounts for the space needed to place cables, services, front-end electronics and mechanical support frames. In the barrel TRT the straw wires are electrically disconnected in the middle, in order to reduce the occupancy, and the signals are read out on either side of the modules. In the end-caps, on the other hand, the signals are read out just at the outer radius, minimizing in such a way the material at the inner radius.

3.2 Expected performance of the TRT

The TRT is designed to provide pattern recognition and level-2 trigger, momentum measurement and electron identification. The first three requirements are reached together with the precision pixel/SCT tracker, the fourth one jointly with the calorimeter.

- High-p_T isolated muons and electrons must be identified at level-2 with high efficiency guided by the relevant level-1 Region of Interest (RoI) defined in Section 2.6. The level-2 algorithm uses a very fast and robust histogramming technique; the algorithm scans all the relevant RoI and the number of hit straws corresponding to a given p_T bin are recorded as soon as the pattern of crossed straws changes. The histogram, shown in Fig. 3.3, contains therefore a very large number of bins and the signal from isolated electrons and muons can be seen above the fluctuations of the pile-up background.

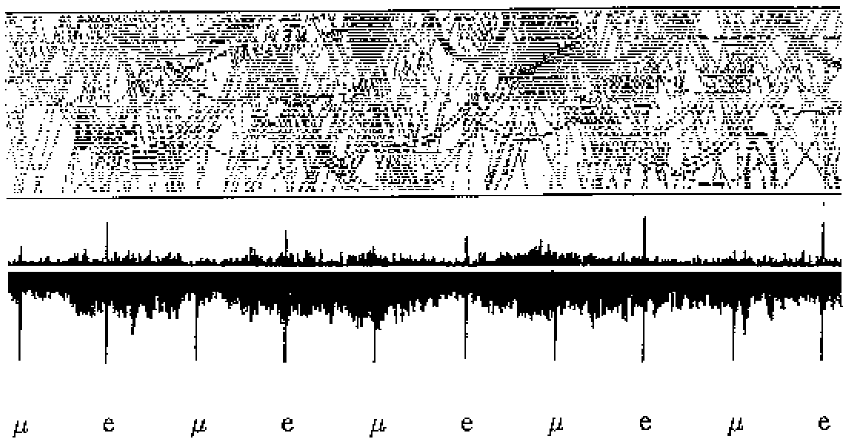

Figure 3.3: Illustration of the histogramming technique used to find tracks in the barrel TRT. The hit straws are displayed in the R-ϕ plane, the expected pile-up at a luminosity of $2 \cdot 10^{34} cm^{-2} s^{-1}$ is overlaid on top of five electron and five muon tracks of $p_T = 20\,\text{GeV}$. The top histogram shows that the TR-hits alone are sufficient to extract the electron signal from the fluctuations of the pile-up background, whereas the bottom shows that the use of the full TRT information clearly separates the isolated high-p_T tracks from the background.

- The TRT contributes to the momentum measurement by providing measurements of the track position in a large number of straws. A track will cross on average 35 straws, and a large fraction of them will give a hit (i.e. will yield a measured drift time within a two-standard-deviation window from the reconstructed position of the track). The hit efficiency depends partially on η and largely on luminosity [21]. At low luminosity, for example, the hit efficiency is expected to be around 90%, providing therefore 32 measurements per track. In this case, the spatial resolution per straw is expected to be 170 μm averaged over all straw layers.

- Electron identification in the TRT is achieved normally using the transition-radiation cluster-counting technique, described in detail in Chapter 4.
- A novel technique for particle identification in the TRT, namely the time-over-threshold, may improve electron identification at low energy and can provide, as well, some hadron identification. This is the main subject of this thesis and it is discussed in detail in Chapter 4-6.

3.3 The TRT straw drift-tube

The basic detecting element of the TRT is the straw drift-tube. A drift-tube is a gaseous detector which is used to measure the position of the track inside the tube. This measurement is performed by very accurately detecting the time that the electron clusters, released in the gas by the ionizing particle, take to drift to the anode wire.

The TRT straw tubes are 4 mm in diameter and less than 150 cm in length. The maximum length is dictated by the overall detector dimensions and the maximum acceptable straw occupancy at the LHC. The 4 mm radius, which gives a 42 ns maximum collection time of the signal, is a compromise between different requirements:

- the detector should respond as fast as possible to ionizing particles (this is crucial at the LHC, since the proton beams collide each 25 ns);
- the straw signal should be large enough to be detectable by the front-end electronics (reducing the diameter of the straws shortens the maximum collection time of the signal, but reduces as well the number of ionization clusters);

- the number of straws crossed by the track should be as large as possible, in order to maximize the number of measurements; this is important for particle identification and momentum measurement.

The TRT straw tube functions as an ionization chamber in the proportional regime, since the charge collected on the wire is proportional to the ionizing particle energy loss. The front-end electronics, discussed in detail in Section 3.6.1, has been designed to provide a very accurate determination of the time of the leading edge of the signal above the 200 eV low-threshold discriminator level. It also detects very large energy depositions (above the 6 keV high-threshold discriminator level), which may be a consequence of a transition-radiation photon absorption, providing therefore the electron signature required of the TRT. The width of the low-threshold discriminator signal also provides partial information about the energy loss of a particle crossing the straw, enhancing therefore the particle identification capability of the TRT detector.

3.3.1 Gas composition

The gas mixture that has been chosen for the TRT is 70% Xe, 20% CF_4, 10%$C0_2$. The choice of Xenon as the main component of the gas mixture is dictated by the necessity to absorb very efficiently photons in the X-ray region. The drawback of this choice, apart from the cost, is the very slow positive ion tail (which needs to be removed by the front-end electronics) with respect to the choice of Argon gas for many detectors. The CF_4 is a molecular gas, which is used to make the gas as fast as possible, minimizing therefore the pile-up in time, which consists of overlapping signals from particles produced in interactions that occurred before or after the bunch crossing of interest. At the LHC, this is a crucial issue since the time between successive bunch crossing is just 25 ns. Since the Xe-CF_4 mixture is rather prone to high-voltage discharge, a small amount of CO_2 is added to stabilize the mixture.

The maximum charge-collection time is determined by the electron drift velocity, which in turn is a function of the electric field in the straw, and depends on the magnitude and the direction of the magnetic field. The dependence of the charge-collection time on the CF_4 concentration (as predicted by the MAGBOLTZ [22] simulation program) is shown in Fig. 3.4, for a ternary mixture containing 70% Xe, in a 2 T magnetic field and for the nominal straw gain of $2.5 \cdot 10^4$. The remainder of the gas is CO_2.

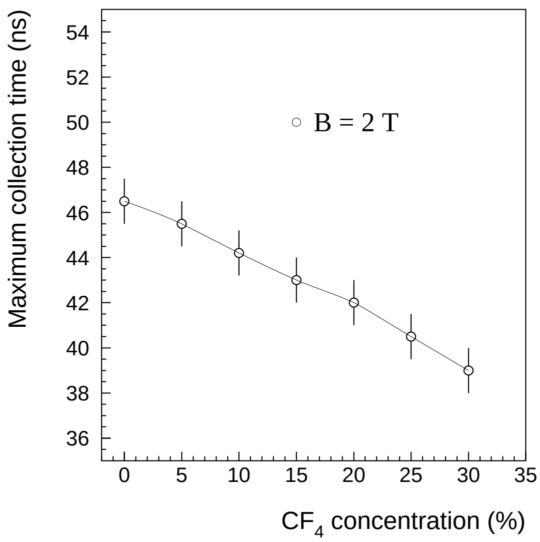

Figure 3.4: Total predicted charge-collection time in a magnetic field of 2 T as a function of the CF_4 concentration for straws with a gas mixture containing 70% Xe and at their nominal gas gain of $2.5 \cdot 10^4$. The remainder of the gas is CO_2.

3.3.2 Straw signal, gas gain and stability of operation

A detailed knowledge of the intrinsic property of the straw signal is essential for the front-end electronics design. Detailed measurements of the currents and the charge deposited in the straws were performed for the chosen TRT gas mixture and the nominal gain of $2.5 \cdot 10^4$. The results of these measurements, reported in Fig. 3.5, show a very fast electron component and a very long ion tail, that extends up to 60 μs. A very long ion tail is characteristics of Xe-based gas mixtures, and must be carefully

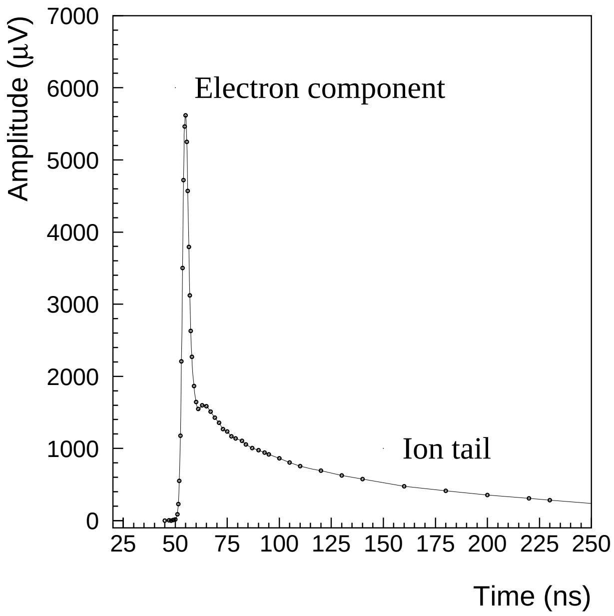

Figure 3.5: Precise measurements of the straw current response to a point-like ionization. The measurements are well represented by the parametrisation, which has been used for the design of the front-end amplifier and shaper.

removed by the front-end electronics. Possible overlapping of these ion tails from successive hits in the same straw may, in fact, lead to a fluctuating baseline current in the straw and, in turn, to a possible spread of the discriminator thresholds. The fast electron component of the straw signal contains only 3-5% of the total charge (integrated over 60 μs), and the signal amplitude for minimum-ionizing particles is smaller by a factor of 3 to 5 then the one obtained for Ar-based mixtures.

The range of gas gain (2.5 to $4 \cdot 10^4$) chosen for the straws for reliable operation at the LHC followed from various considerations. The lower limit on the gas gain is set by the necessity to produce a signal for minimum-ionizing particles (MIPs) well above the noise level in the front-end electronics ($\sigma \sim 40\,\text{eV}$). Extensive studies show that a gas gain of $2.5 \cdot 10^4$, combined with a low-threshold setting of 200 eV, achieves a high drift-time measurement efficiency and the required drift-time accuracy. The maximum gas gain, on the other hand, is limited by the probability to create self-limited streamer (SLS) discharge, which rises very quickly with the gas gain, as is shown in Fig. 3.6. This plot also shows that non-linearities in the dependence of the gas gain on the straw high voltage appear above 1600 V, due to space-charge effects in the avalanche. The space-charge effect, expressed as the reduction in signal amplitude, is shown in Fig. 3.7 as a function of the gas gain and of X-ray energies. The maximum gas gain has been set to $4 \cdot 10^4$, following the requirement that the loss

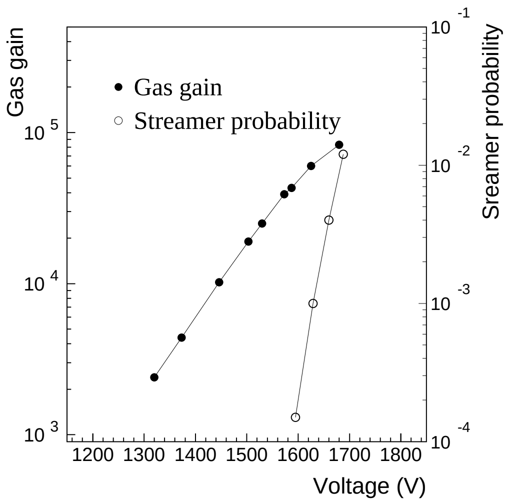

Figure 3.6: Straw gas gain and self-limited streamer discharge probability as a function of the high-voltage.

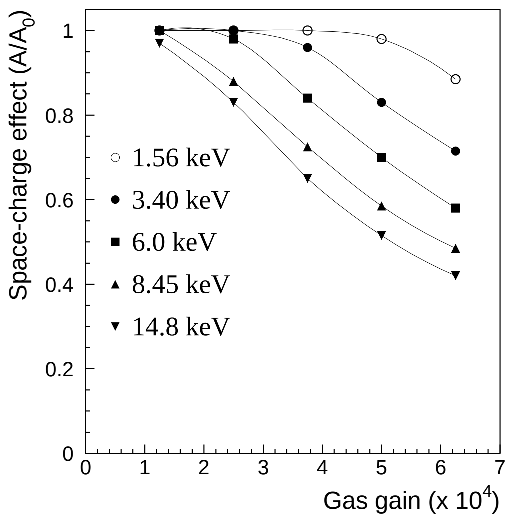

Figure 3.7: Effect of space-charge, expressed as the observed fraction of the total amplitude, as a function of the straw gas gain and for different X-ray energies.

of the signal due to space-charge effects should not exceed 20% for X-ray energies of 6 to 7 KeV relevant for transition radiation.

The straw operation in proportional mode is always accompanied by SLS discharges. The fast component of the signals due to the SLS has an amplitude 100 to 200 times larger than the corresponding one in proportional mode, due to the much larger radial size of the streamer (1 to 1.5 mm) with respect to the normal avalanche size of about 10 to 20 μm in the normal proportional mode. As shown in Fig. 3.6, for gas gain below $4 \cdot 10^4$, the SLS probability remains well below 10^{-2}; this guarantees that the front-end electronics dead-time will remain below 1-2%.

The gas gain depends on environmental conditions, as temperature and pressure, therefore some straws irradiated with Fe-55 source will be constantly monitored and the HV adjusted via an HV feed-back loop. However, the most important dependence of the gas gain is on the wire offset (the displacement of the anode wire from the central position inside the straw), as shown in Fig. 3.8. In the case of a large wire offset, the electric field on the side of the wire closest to the straw wall increases significantly, causing large variation in the gas gain. The specification for the construction of the TRT detector requires the wire offset to be below 300 μm, that in turn implies a gas gain variation lower than 5%.

3.3.3 Straw operating conditions at the LHC

The TRT straws at the LHC will be continuosly irradiated by charged particles (mostly MIPs coming from primary inelastic collisions), neutrons and photons. The expected straw counting rates are tabulated in Table 3.1 as a function of the straw position in the TRT and of the signal amplitude, respectively for MIPs and for all particles (in parenthesis). The largest rates (almost 20 MHz) are expected for the innermost straw barrel layers and for the long radial straws in the end-cap.

The neutron background (from which most of the photon background originates) is rather uniform and arises mainly from hadronic showers in the calorimeters. The

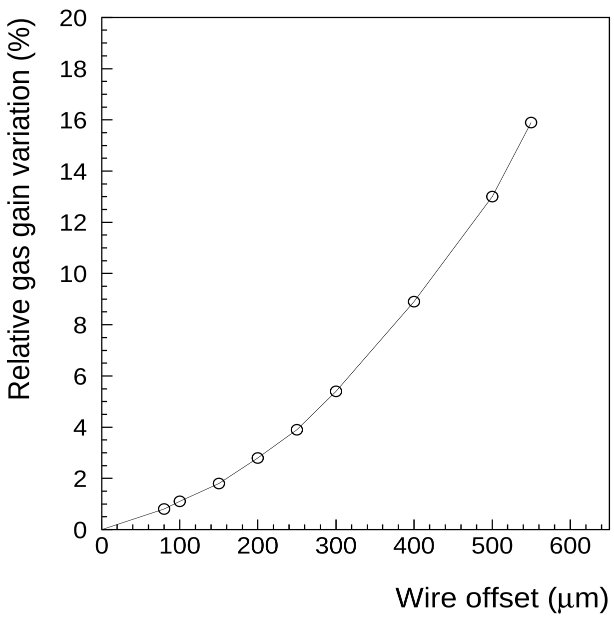

Figure 3.8: Relative gas-gain variation as a function of the wire offset for the nominal TRT gas mixture. For wire offset below 300 μm, the gas gain variation is lower than 5%.

neutron energy spectrum, which depends on the detailed geometry of the surrounding material, is shifted towards the thermal region by the radiator material and by other moderator material, placed for this purpose in front of the end-cap calorimeters. The presence of moderator material greatly reduces the rate of the recoil protons, due to fast neutrons, which is expected to be lower than a couple of kHz. These recoil protons are heavily ionizing particles which produce streamer discharges in the straw gas; their expected rate ($\sim$ 1 kHz), on the other hand, is much lower that the one expected from MIPs.

Thermal neutrons, instead, produce mainly a large low-energy photon flux (in the 100 to 200 MHz range, at the LHC design luminosity), which turns out to be the dominant source of the straw counting rates due to neutrons. Measurements of the straw response to such photons, performed using a small prototype of a barrel

Table 3.1: Expected straw counting rates from MIPs and from all particles (in parenthesis). The uncertainties on these rates are ∼50%, dominated by uncertainties on the inelastic cross-section at the LHC.

Straw position in the TRT	0.2 keV threshold	6.5 keV threshold	Streamers and large-amplitude signals
Barrel (R = 108 cm)	5 (6) MHz	0.25 (0.40) MHz	2.5 (11) kHz
Barrel (R = 64 cm)	17 (18) MHz	0.90 (1.1) MHz	9 (21) kHz
Average in end-cap for 39 cm long straw	6.5 (8) MHz	0.32 (0.5) MHz	3.2 (4) kHz
Maximum in end-cap for 55 cm long straw	17 (19) MHz	0.80 (1.1) MHz	10 (10) kHz

module, are shown in Fig. 3.9, which represents the probability for an incident photon to trigger the 200 eV low-threshold discriminator level as a function of the photon energy and the orientation of the magnetic field with respect to the straw axis. These measurements, together with the evaluation of the expected photon background in the TRT region, made it possible to estimate the expected straw counting rate due to photons, which is the main reason for the discrepancy between the two sets of numbers in Table 3.1. The straw counting rate due to photons is predicted to be lower than 15% for the low-threshold level, while it can be as high as 60% for the high-threshold level.

3.4 Design and Construction of the Barrel TRT

A barrel TRT module is shown in Fig. 3.10. The straws, a straw alignment plane, stacks of fiber radiator and the carbon-fiber shell can be seen. The complete barrel contains 96 of such modules, disposed in three rings as described in Section 3.1, and it is shown in Fig. 3.11 together with the two barrel support structures at each end. The

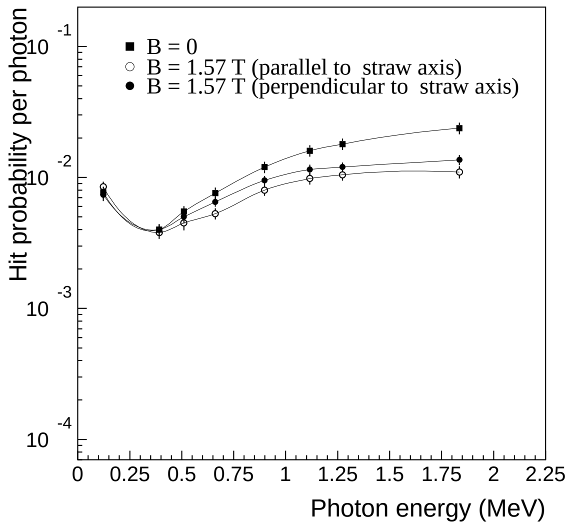

Figure 3.9: Straw hit probability for energy above 0.2 keV as a function of the photon energy and of the magnetic field.

modular design permits the testing of individual modules as soon as they are built and allows the construction to be split between different sites. The main features of the design of a barrel module and the assembly procedures are given in the following subsections.

3.4.1 Barrel Module Components and Design

A barrel module, as illustrated in Fig. 3.10, is housed in a carbon-fiber shell. The carbon-fiber material has been chosen for his stiffness, necessary to keep the module straight, and for the high thermal conductivity required to carry out the heat produced in the straws via cooling tubes placed in two diagonal corners. The shell supports the radiators and the alignment planes, necessary to align the straws.

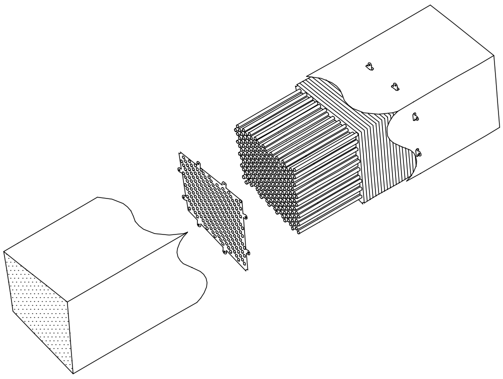

Figure 3.10: A view of a barrel module showing a straw alignment plate, the straws, stacks of fiber radiator, and the shell.

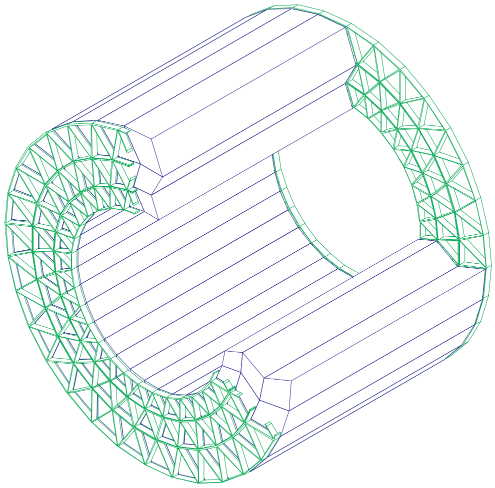

Figure 3.11: Layout of the barrel TRT showing three layers of barrel modules (type I in the inner layer, type II in the middle layer, and type III in the outer layer) and the support structure.

The alignment planes are 100 μm thick Kapton sheets with a pattern of 4.3 mm diameter holes and are positioned every 25 cm along the module within the shell. This configuration keeps the straws straight over the full length of the barrel module. The alignment planes have a set of tabs on each side that pass through small holes in the shell. Holes punched in these tabs allow the Kapton sheets to be aligned on an external frame, and then to be glued to the shell after alignment.

The radiator chosen for the barrel consists of 5 mm fabric plies, formed by polypropylene-polyethylene fibers, with a hole pattern to match the ones in the alignment planes. All the space in the shell between successive alignment planes is filled with radiator plies loosely packed.

The straws, made from a coated polymide film (Kapton based) and reinforced with C-fibers, are inserted through the holes and therefore totally embedded in the radiator.

The signal wire for the straws is a gold-plated tungsten wire with a (30 ± 0.3) μm diameter. The wires in the barrel TRT are electrically disconnected in the middle, with the exception of the nine most innermost layers, where the straw wires are divided in two places in order to give an active region of 36 cm at each end. The central part is not read out. This strategy reduces the occupancy of these straws, which otherwise would be too large for the proper operation of the detector in the LHC environment. The wire sections are joined by fusing a small glass capillary tube to the two segments of wire. The wire is supported at the center of the straw by a wire centering structure, called twister. Twisters are also used for centering the wire at the end of each module.

The module end-plate region is shown in Fig. 3.12. The two main components of the end-plate are two printed-circuit boards that form the gas manifold, namely the high-voltage (HV) plate (at the bottom in the figure) and the tension plate (at the top in the figure). The HV plate, whose front-side view is shown in Fig. 3.13, is glued into the shell. The straws are held and sealed to the HV plate. The high-voltage is brought from the high-voltage source to the back side of the HV plate through copper traces on a thin Kapton sheet, and then transferred to the front side of the HV plate through pin sockets to the group of eight straws. Conducting glue is then used to make the electrical connection between the individual straws and the HV plate. Each group of eight straws in the HV plate has its own 1000 pF HV capacitor, which is connected with a double pin to the socket in the HV plate. This design allows for HV capacitor replacement. The other end of the HV capacitor is grounded to the tension plate.

The tension plate, part of which is shown in Fig. 3.14, holds the wires and forms the outer gas manifold. The sense wire is fixed to the tension plate with a tension

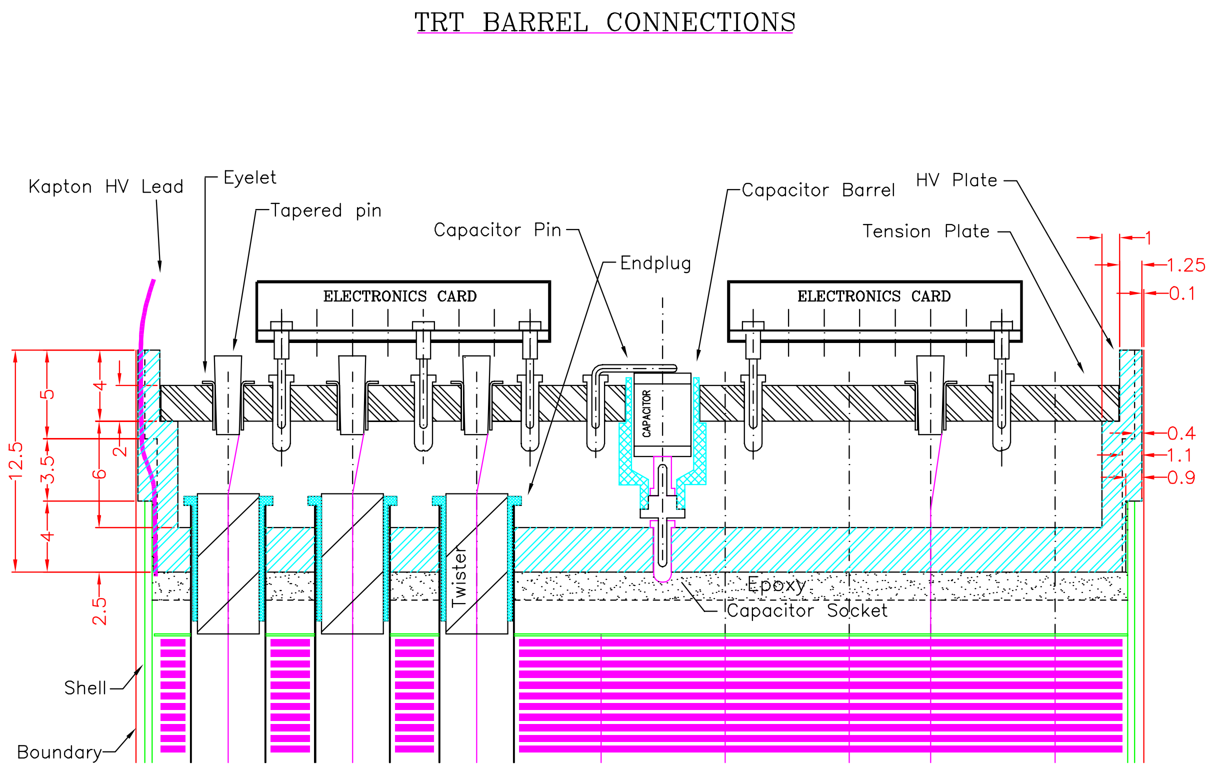

Figure 3.12: Side view of the module end-plate region. The tension plate, on the top, holds the wires and forms one side of the gas manifold. The straws are glued into the high-voltage plate at the bottom. The wires are centered in the straws by the wire supports inserted in the straw ends (see text).

of 60 g using a conical pin forced into an eyelet on the tension plate. The holes for the capacitor sleeves (large holes), the holes for the wire fixations (medium holes) and the sockets for the connectors to the front-end electronics boards (small holes) are shown in Fig. 3.14. In the design of the tension plate, as well as in the one of the HV plate, there is space on the diagonal corners for the cooling tubes. Cooling is necessary to keep the module temperature within the 10° C range that has been specified for the TRT; this range would otherwise be exceeded due to the power dissipated in the straws as the positive ions, created by the ionizing particles, flow to the cathode. The total power dissipated per module is about 6 W at the design luminosity. These cooling lines will be part of the 15° C fluorinert-cooling system foreseen for the complete TRT detector. The printed circuit layout of the tension plate superimposed on the HV board is shown in Fig. 3.15.

From the gas manifold, or from the straws, some Xe may leak into the module body surrounding the straws. This leak could cause increased absorption of TR photons outside the gas active volume, reducing the TRT electron-identification power in the straws. A CO_2 ventilation system is foreseen for the module array to keep this region free from Xe.

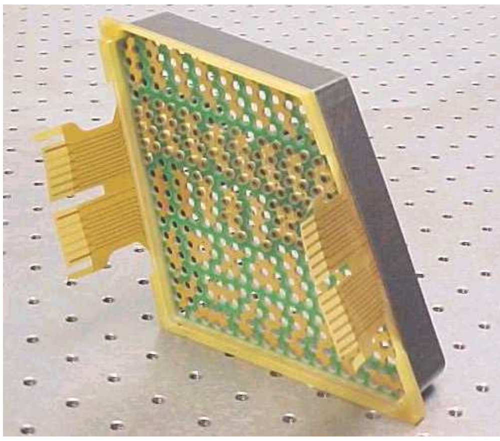

Figure 3.13: An high-voltage plate.

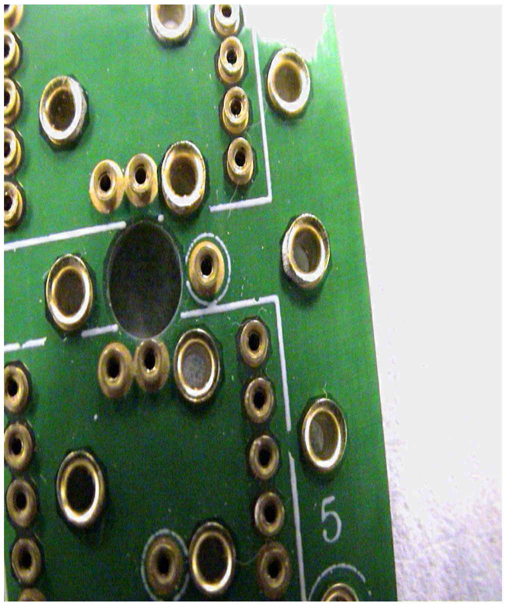

Figure 3.14: Photograph of part of the tension plate.

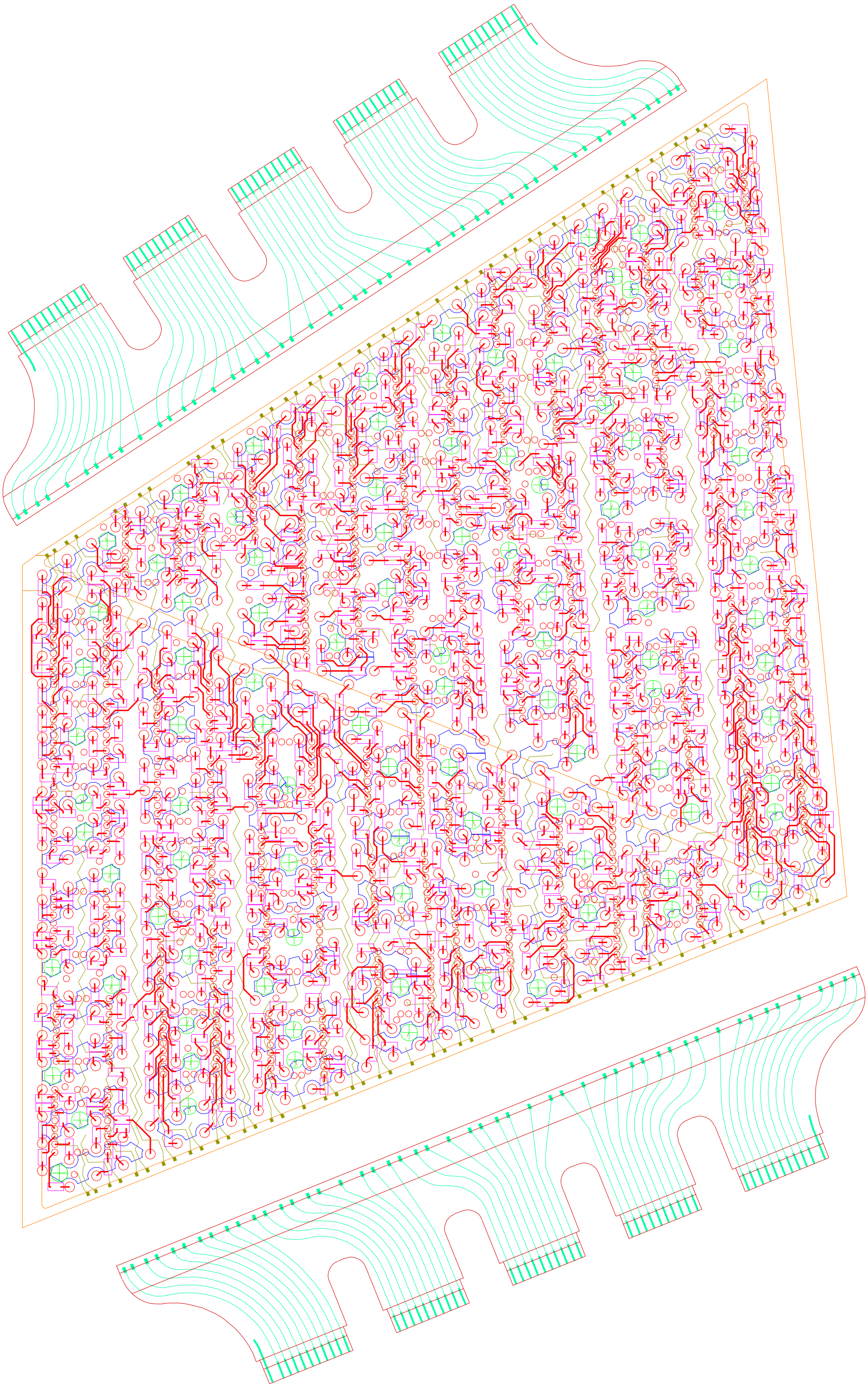

Figure 3.15: Printed circuit layout of the tension plate superimposed on the HV board.

3.4.2 Assembly Procedures

Many of the components of the barrel TRT are manufactured in industry. In the production sites these components are tested for the conformance to their specification. The shell preparation is the first operation during assembly. For this operation, and for alignment purposes, a universal assembly fixture, shown in Fig. 3.16, has been designed. This tool is large enough to contain the type III module, and can be adapted to smaller modules (type I and II) using smaller fittings. The shell is fixed on

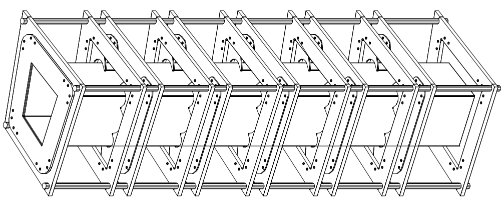

Figure 3.16: The universal assembly fixture.

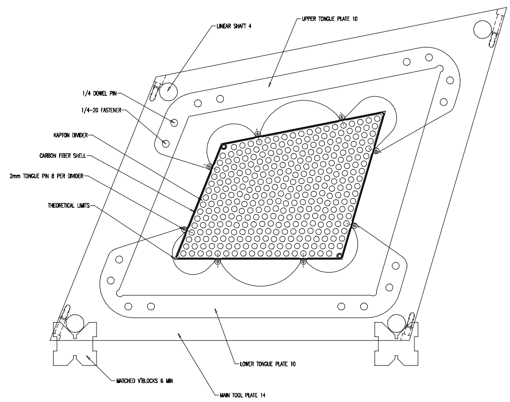

Figure 3.17: The Kapton alignment tooling.

the universal assembly fixture, where it is cut to length and machined for the straw alignment plane tabs. The fixture is clamped to a flat assembly table. The alignment planes are positioned with an accuracy of better than 50μm. The alignment tooling, that guarantees the correct positioning of the straws in the module, is represented in Fig. 3.17, which shows a transverse view of the universal assembly fixture. The planes are aligned by a set of pins that hold the tabs that extend through the shell. Eight alignment pins are positioned by a double set of alignment fingers attached to the assembly frame, with an upper set holding four and a lower set holding four.

During the insertion and the alignment of successive alignment planes, the fiber radiator is inserted into the shell. The fabric radiator plies are punched by a stamping company with the hole pattern required using a steel die and a 70 ton traveling head press. The punched radiator is formed at the component assembly site at Hampton University, into packs about 25 cm thick. After insertion of the radiator and alignment planes, the high-voltage plate is then inserted.

The high-voltage plate assembly (shown in Fig. 3.12) consists of a printed circuit plate with holes for passage of the straws, a Kapton distribution line bringing the HV to the plate and a G-10 collar. It is inserted in the end of the shell and the outside of the collar glued to the shell.

The straws are then inserted into the structure, after having been cut to length. In order to minimize leaks from the ionization gas volume, the straws are glued on either side of the HV plate. Conducting epoxy, which also establishes the electrical connection to the straws, is applied on the front side of the plate, while non conducting epoxy is injected on the back side of the plate through small holes in the shell (potting). The potting operation is carried on with the module sitting in vertical position, in a mobile carrying fixture. The potting glue is a very fluid epoxy glue, which flows easily on the plate and guarantees an efficient gas barrier.

The tension plate is then glued into the high-voltage collar, and wire stringing begins. Before the insertion in the module, the wire is cut into 2 m lengths with the wire joint about midway. With 60 g tension the wire is centered on the wire stringing machine and a pinning tool locked at the 75 cm point on one side of the joint. A 50 μm tungsten leader is then inserted through the straw, attached to one end of the wire and used to pull the wire through the straw. The wire is then tensioned to 60 g, positioned using the reference tool, and fixed to the tension plate, by inserting a locking taper pin.

3.5 The TRT electronics

The TRT electronics consists of a front-end section, which is plugged into the tension-plate, and of a back-end part, which is located outside the Inner Detector. The schematic diagram of the TRT electronics (both front-end and back-end) is shown in Fig. 3.18.

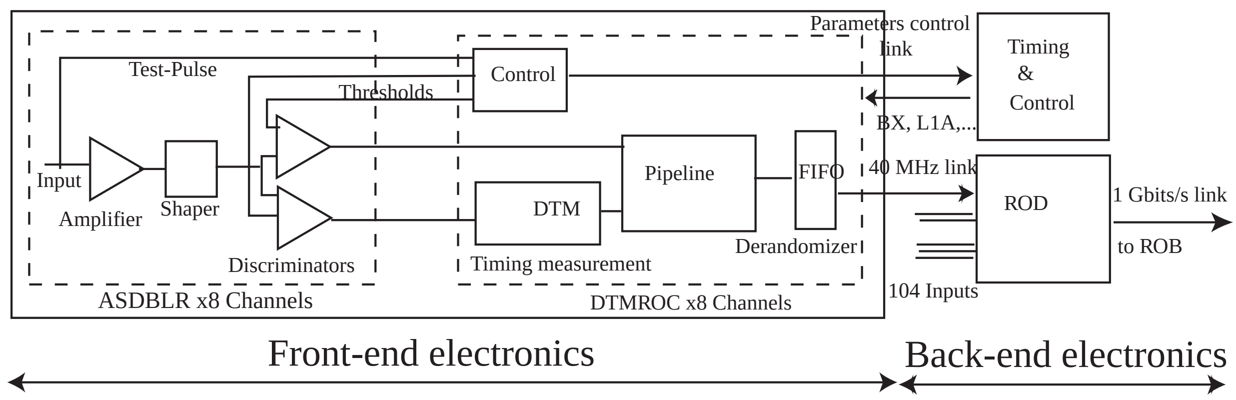

Figure 3.18: Schematic diagram of the TRT electronics.

The front-end electronics is discussed in Section 3.5.1, while the back-end electronics and its interface with the ATLAS Data Acquisition System (DAQ) is discussed in Section 3.5.2.

3.5.1 The front-end electronics

The TRT front-end electronics consists of two chips, the ASDBLR (Amplifier Shaper Discriminator BaseLine Restorer) and the DTMROC (Drift Time Measurement Read Out Control). These two chips are located on the detector and are therefore constructed with radiation-hard technology to withstand the very large radiation doses inside the Inner Detector.

The ASDBLR is designed to amplify and to shape the signal coming from the straw, removing the long tail arising from the slow ion signal component, and to discriminate the signal at two distinct thresholds. The low-threshold (200 eV) is used to detect minimum-ionizing particles and provides tracking functionality, while the high-threshold (5000 eV) is used for transition-radiation functionality.

The DTMROC provides timing information for the low-threshold signal (used to measure the position of the track inside the straw), and stores in a pipeline this information and the status of the two discriminators (above or below the thresholds) while waiting for the level-1 trigger decision. For any level-1 trigger accepted (L1A), the DTMROC extracts from the pipeline that information (for the bunch crossing which gave rise to the L1A and the two following bunch crossings), and transmits it to the back-end electronics, as described in Section 3.6.2.

The ASDBLR Integrated Circuit

The ASDBLR is a full-custom, analog, bipolar ASIC chip. It provides eight channels of amplifier, shaper, discriminator and baseline restorer on a 6.17x4.78 mm silicon substrate. The block diagram of the circuit is shown in Fig. 3.19. The response of the circuit for a point-like ionization (according to a SPICE calculation) is shown in Fig. 3.20 at the output of the preamplifier (solid line) and of the shaper (dotted line). The long ion tail characteristics of a Xe-based gas mixture is removed by a cancellation network in the shaper.

The peaking time in the shaper has been set to 7.5 ns in order to optimize signal-to-noise ratio, position resolution and double-pulse resolution. The barrel straws are read out at both end, while the center insulated break is not terminated. When the

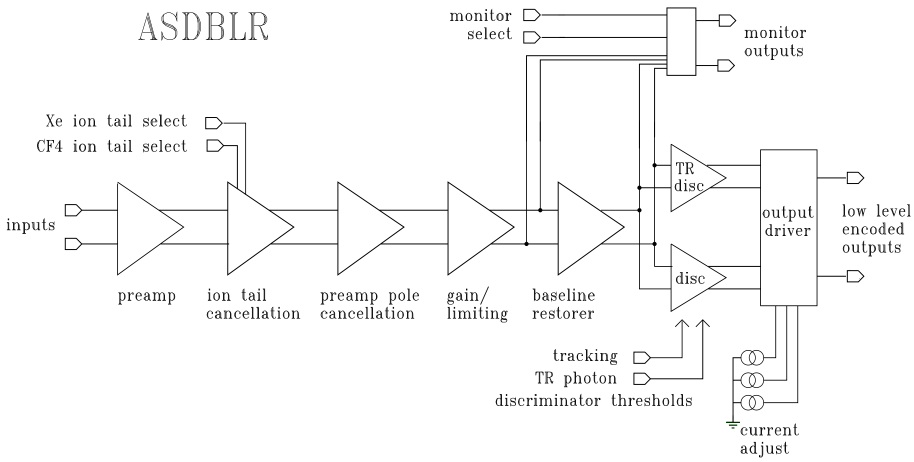

Figure 3.19: Block diagram of the ASDBLR circuit.

ionization clusters reach the anode wire, part of the signal travels towards the front-end electronics; the reimanent part travels towards the unterminated end, is reflected and reaches the preamplifier delayed from the prompt signal by as much as 6 ns. The straw output signal depends therefore on the position where the particle crosses the straw; in order to limit this dependence the shaping time should therefore be kept small.

At very high rate, the threshold may become unstable, due to large energy depositions that saturate the ion tail cancellation network; this also could result in persistent triggering. This problem is solved by the implementation of a baseline restorer. The signal at the output of the baseline restorer (BLR) is shown in Fig. 3.21, respectively for a small (2 fC) signal and for a large (25 fC) signal. The BLR signal output is fed into two discriminators, whose output is encoded into a programmable bi-level output current. The ^{55}Fe response of the ASDBLR shaper (upper trace) and bi-level discriminator (lower trace) is shown in Fig. 3.22. Several ASDBLR chips have been measured to determine channel-to-channel uniformity and noise characteristics. The

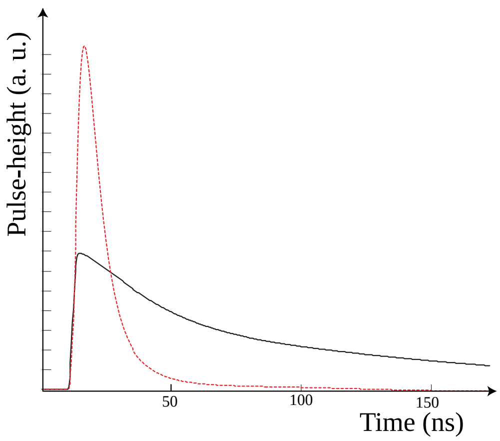

Figure 3.20: Simulation of the output of the preamplifier (solid) and shaping circuit (dashed).

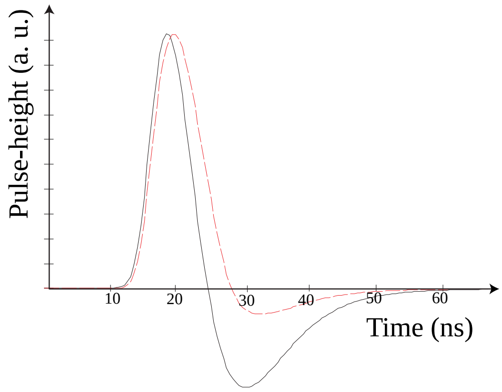

Figure 3.21: Simulation of the signal (for 2 fC (solid line) and 25 fC (dotted line) input charges) after baseline restoration. The larger signal have been scaled to the smaller one.

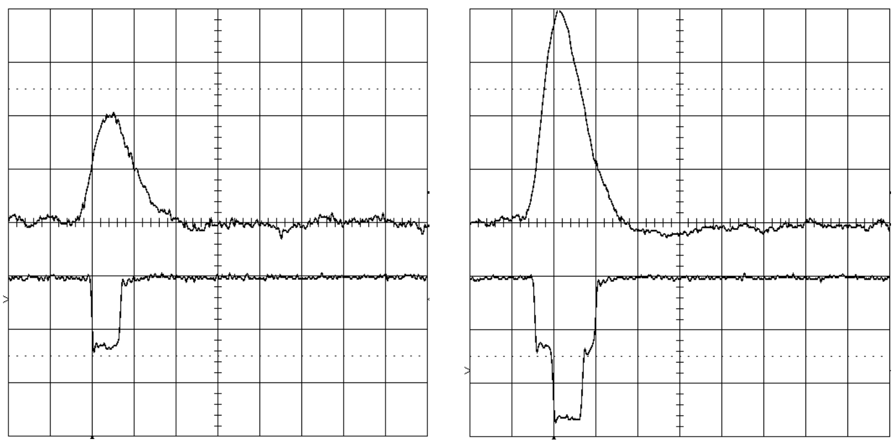

Figure 3.22: Output of shaper (top) and discriminator (bottom) of the ASDBLR (20 ns/div).

relation between input signal amplitude and the discriminator threshold, shown in Fig. 3.23, demonstrates for a group of 16 straws that a 200 mV threshold corresponds to a 250±25 eV energy threshold.

The low-threshold should be set as low as possible in order to have a high efficiency for detecting minimum ionizing particles. It is, therefore, important to minimize the noise in the front-end chips. The noise counting rate is shown in Fig. 3.24 as a function of the low-threshold settings; at the nominal low-threshold setting of 200 eV, the counting rate is well below 10 kHz.

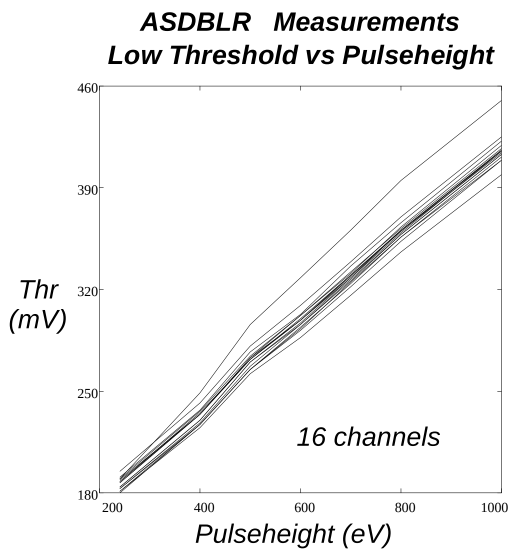

Figure 3.23: Low-threshold uniformity.

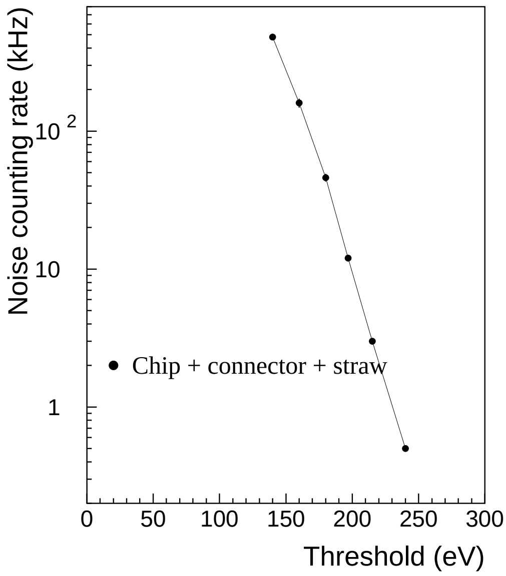

Figure 3.24: Counting rate as a function of the low-threshold value.

The DTMROC Integrated Circuit

The DTMROC, shown in Fig. 3.18, is composed of two main parts. The control section communicates with both the ASDBLR and the back-end electronics, by transmitting reference currents for threshold adjustments, as an example. The time-measurement and read-out section processes the ternary encoded information from the ASDBLR. The read-out part consists of a digital pipeline, where the data is stored and delayed for the level-1 trigger latency of 128 beam crossing, and of a derandomizer, where the data correspondent to the bunch-crossing accepted from level-1 trigger and the two successive bunch-crossings are stored while waiting for readout.

The drift-time measurement (DTM) circuit, shown in Fig. 3.25, consists of a delay-locked-loop (DLL) and a Gray encoder. The LHC clock (BX) is delayed exactly one

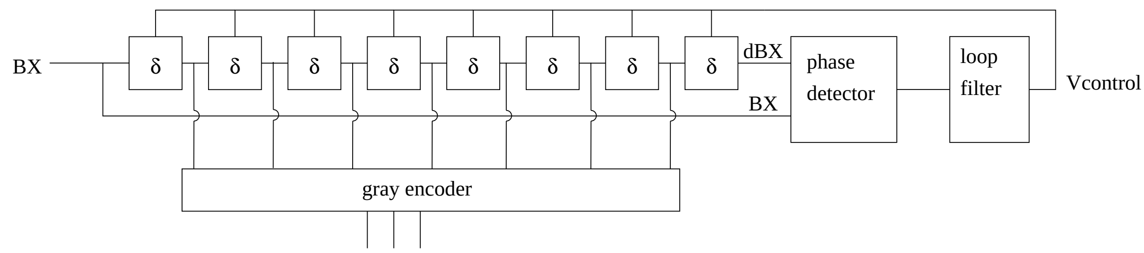

Figure 3.25: Schematics of the drift-time measurement circuit.

clock cycle in a chain of 8 identical delay elements. By storing the state of the nodes between the delay elements when the input signal occurs, the time measurement is performed with a binning of 1/8 of the cycle time, e.g. 25 ns/8=3.125 ns. The phase detector controls the chain in order to insure a one clock cycle as the total delay. A gray encoder encodes the state of the 8 nodes into 3 bits which are then fed to the latch. The latch inputs are also connected to the low and the high-discriminator signals. When the low-threshold signal is high, the inputs are latched. The output of the latch is fed into the pipeline and then to the derandomiser, from where the data are serially read out via a twisted pair cable to the Read Out Driver (ROD), discussed in Section 3.6.2.

The barrel front-end boards

The main front-end electronics board printed circuit is the tension-plate, which has already been discussed, from the mechanical point of view, in Section 3.5. The tension-plate is the fixing-plate for the straw wires and, in addition, is the mechanical support for the ASDBLR boards. The design of the tension-plate, from the electrical point of view, is very delicate, since the straw signals are very low in amplitude and sensitive to noise. The signal traces on the tension-plate (which carries the signal from the straws to the ASDBLR via the ASDBLR board) are as short and separate as possible, in order to minimize the cross-talk. A ground plane is placed on the top side of the tension-plate, while the signal traces run on the bottom side.

There are six different types of tension-plates, since there are three type of modules of different dimensions, and the straws are read out at both end. Each tension-plate is sub-divided into two smaller triangular areas, where the daughter boards are mounted. The straws are connected to high voltage but in a case of breakdown they could destroy the electronics, so all the ASDBLR inputs are equipped with a protection network consisting of a fast diode and a current-limiting resistor. The diodes and resistors are mounted in the ASDBLR boards.

3.5.2 The read-out electronics

The data flows from the front-end read-out boards to the Read Out Drivers (RODs) and then to the Read Out Buffers (ROBs), as shown in Fig. 3.18. The ROB is common to all ATLAS sub-detectors, and it is used to provide the data for the second and third level triggers. The data is therefore stored in the ROBs according to the Region of Interest (ROI), defined by the first level trigger. For the TRT, a ROI is defined by $\Delta\phi=2\pi/32$ and the read out organized in subsets of $\Delta\phi$. One ROD reads out 1/32 of each barrel side, or in other words 1664 straws or 104 DTMROCs. A trigger ROI will then be covered by 2 RODs and subsequently by 2 ROBs.

Data flow and data reduction

The very high expected TRT occupancy requires a very careful design of the data flow. For each L1A, the DTMROC transmits 27 bits for each straw (1 bit to indicate the presence of the high-threshold level and 8 bits for the status of the low-threshold discriminator, for three consecutive bunch crossings), plus control bits. The DTMROC reads out 16 straws, for a total of 509 bits. A ROD receives data from 104 DTMROCs, which in turn implies about 52 kbits of information per L1A. For a 75 kHz L1A rate, the total rate is $\sim$ 4 Gbits/s, far in excess of the available bandwidth (the link between a ROD and a ROB cannot exceed 800 Mbits/s for design).

A zero-suppression scheme must therefore be implemented in the ROD, in order to significantly reduce the amount of data to be transmitted. The zero-suppression scheme applies a gate of tunable position and width to the data received from the front-end electronics. Straws with the low-threshold bit set within this gate are considered as "valid", and the information is reduced in the following way:

- For empty straws, only two consecutive bits set to 0 are transmitted.
- For "valid" straw, the complete information is transmitted (leading edges, trailing edge flag, high-threshold hit flag).
- For non "valid" straws which are not empty, only the low and the high-threshold bits are transmitted.

This scheme is based on the fact that each particle crossing the straw deposits energy near the straw wall. Positioning a narrow gate close to the maximum drift time of

42 ns should then in principle allow all the hits from the bunch crossing of interests to be tagged, minimizing the contribution from the neighboring bunch hits, which have the same distribution but shifted by 25 ns. The width of the gate must be chosen as a compromise between a high efficiency to record hits from the in-time bunch and a good rejection of the out-of-time bunch hits. The expected bandwidth from the ROD to the ROB is shown in Fig. 3.26 as a function of the luminosity, for a 75 kHz L1A trigger rate and for different gate widths while the fraction of "valid" straws is shown in Fig. 3.27, again as a function of the luminosity.

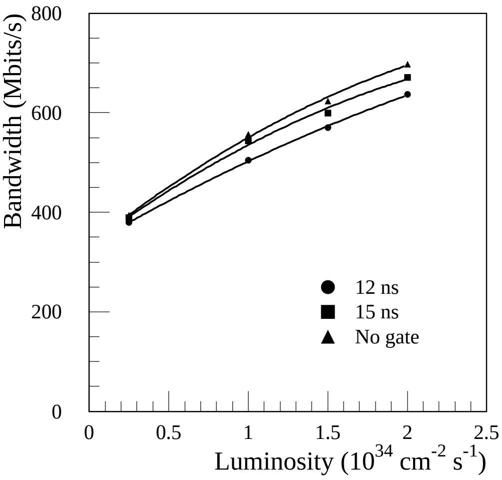

Figure 3.26: ROD-ROB bandwidth for a L1A rate of 75 kHz.

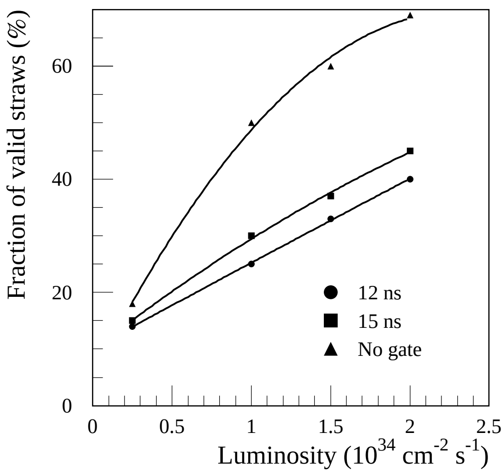

Figure 3.27: Fraction of valid straws as a function of the luminosity and the gate width.

Chapter 4

Particle identification using the TRT detector

The TRT straw drift-tube, as has been discussed in Chapter 3, provides two types of information: the distance of closest approach of the track to the anode wire (for tracking purposes via drift-time measurements) and the energy deposited in the straw (for particle identification). This energy deposition is the sum of the ionization losses of the charged particle crossing the straw and of the usually larger energy depositions due to transition-radiation photon absorption. In the following sections a review of these two processes is given, and the techniques for particle identification in the ATLAS TRT are discussed.

4.1 Ionization

Charged particles lose energy continuously by interacting with matter. Moderately relativistic charged particles other than electrons lose energy primarily by ionization. The mean energy loss is given by the Bethe-Bloch function [7]:

$$-\frac{dE}{dx} = Kz^2\frac{Z}{A}\frac{1}{\beta^2}[\frac{1}{2}\ln\frac{2m_ec^2\beta^2\gamma^2T_{max}}{I^2} - \beta^2 - \frac{\delta}{2}] \tag{4.1}$$

where T_{max} is the maximum kinetic energy which can be imparted to a free electron in a single collision.

$$T_{max} = 2m_e c^2 \beta^2 \gamma^2 \tag{4.2}$$

This latter formula is valid for $\frac{2\gamma m_e}{M} \ll 1$; at the highest energy T_{max} has a small dependence on M, the incident particle mass, but for all practical purposes in high-energy physics $\frac{dE}{dx}$ in a given material depends only on β. The variables used in the previous formulae are defined in Tab. 4.1. The Bethe-Bloch curves are shown in

Symbol	Definition	Units or Value
α	Fine structure constant ($e^2/4\pi\epsilon_0\hbar c$)	1/137.035 999 76(50)
M	Incident particle mass	MeV/c^2
E	Incident particle energy γMc^2	MeV
T	Kinetic energy	MeV
$m_e c^2$	Electron mass $\times c^2$	0.510 998 902(21) MeV
r_e	Classical electron radius $e^2/4\pi\epsilon_0 m_e c^2$	2.817 940 285(31) fm
N_A	Avogadro's number	6.022 141 99(47) $\times 10^{23}$ mol^{-1}
ze	Charge of incident particle	
Z	Atomic number of medium	
A	Atomic mass of medium	g mol^{-1}
K/A	$4\pi N_A r_e^2 m_e c^2/A$	0.307 075 MeV g^{-1} cm^2 for $A = 1$ g mol^{-1}
I	Mean excitation energy	eV (*Nota bene!*)
δ	Density effect correction to ionization energy loss	
$\hbar\omega_p$	Plasma energy ($\sqrt{4\pi N_e r_e^3}\, m_e c^2/\alpha$)	$28.816\sqrt{\rho\langle Z/A\rangle}$ eV$^{(a)}$
N_e	Electron density	(units of r_e)$^{-3}$
w_j	Weight fraction of the jth element in a compound or mixture	
n_j	$\propto$ number of jth kind of atoms in a compound or mixture	
X_0	Radiation length	g cm^{-2}
—	$4\alpha r_e^2 N_A/A$	(716.408 g cm^{-2})$^{-1}$ for $A = 1$ g mol^{-1}
E_c	Critical energy	MeV
E_s	Scale energy $\sqrt{4\pi/\alpha}\, m_e c^2$	21.2052 MeV
R_M	Molière radius	g cm^{-2}

Table 4.1: Summary of the variables used in this Section. From [7].

Fig. 4.1 for different materials. The energy loss decreases with increasing momentum as $\frac{1}{\beta^2}$ at low momentum, and reaches a minimum at $\beta\gamma \sim 3$. Above that point, the energy loss rises logarithmically in the so-called relativistic rise region, until it saturates (at the so-called 'Fermi plateau'). The relativistic rise is limited by the polarization of the media, which depends on the electron density. For gases, which have a low electron density, the relativistic rise is fairly high. For Xenon, as an example, the relativistic rise is around 75%. The Bethe-Bloch formula describes just

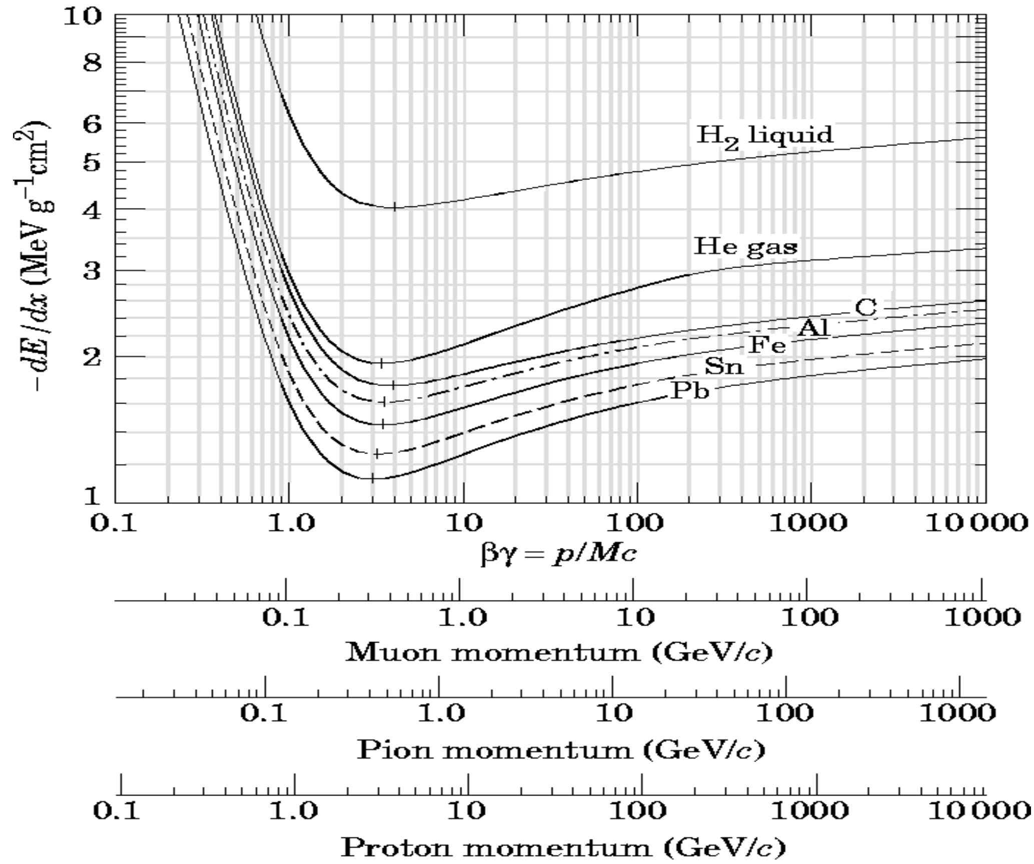

Figure 4.1: The energy loss curves as a function of momentum for different particles and for different materials. From [7].

the mean energy loss. The distribution of the energy loss is Gaussian for thick layers, while it follows the so-called Landau distribution in the case of thin layers. Big fluctuations in the energy loss, in this latter case, cause the typical high-energy tail of the distribution (the Landau tail), which is due to knock-on electrons, or δ-rays.

Electrons, on the other hand, at low energy lose energy primarily by ionization, but as the energy increases bremsstrahlung becomes more important, as shown in Fig. 4.2. Ionization loss by electrons differs from loss by heavy particles because of kinematics, spin and the identity of the incident electron with the electrons which it ionizes. While ionization losses rise logarithmically with energy, bremsstrahlung losses rise nearly linearly and dominate above a few tens of MeV in most materials.

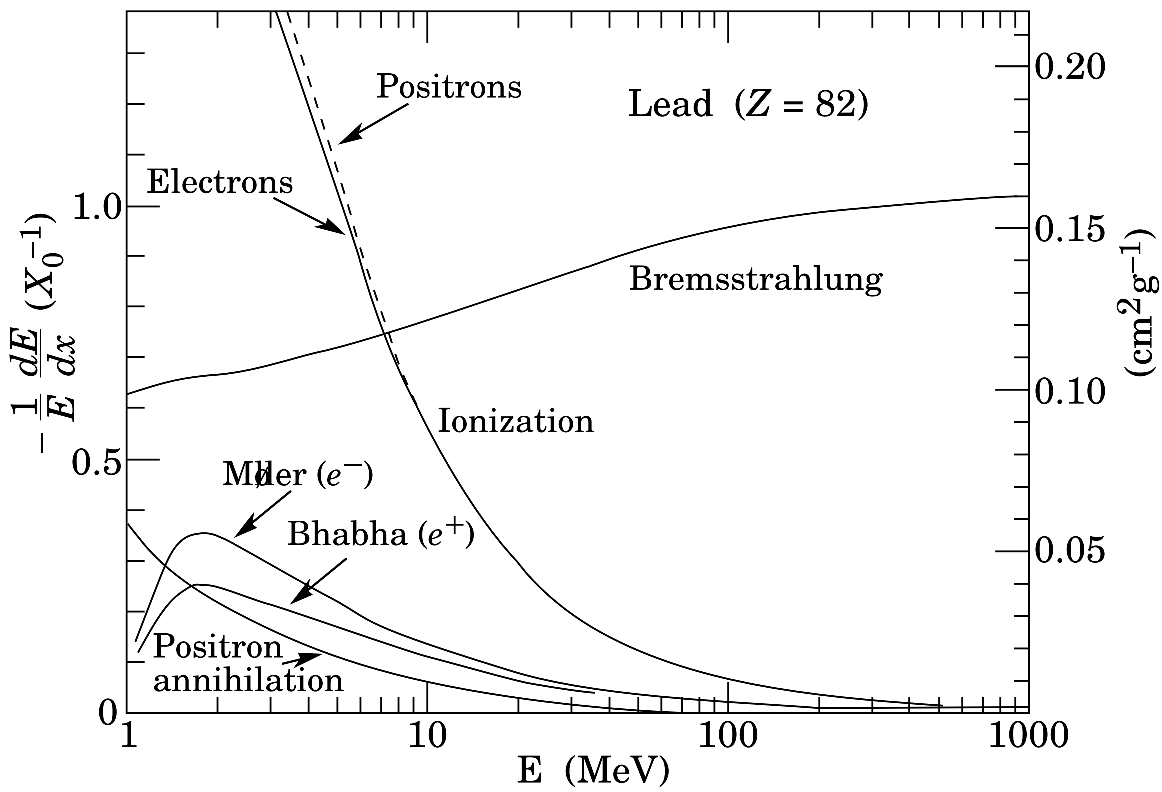

Figure 4.2: Fractional energy loss per radiation length as a function of electron or positron energy. From [7].

4.2 Transition Radiation

Transition radiation (TR) is the electromagnetic radiation that is emitted when a charged relativistic particle crosses the interface between media with different dielectric properties. The theory regarding transition radiation was developed around the middle of this century [23] but, due to the very low intensity of the radiation, experimental evidence was found much later. Efficient detection of the TR photons, in the X-ray region, useful for the design of a practical transition-radiation detector, was shown to be possible only in the 1970's [24, 25, 26, 27]. The theoretical predictions important for experimental work are outlined in this section. The formulae presented were derived using standard electromagnetism calculations. The ideal case of transition radiation from single interface is first discussed, then the extension to the practical case of single foil and radiator is described.

4.2.1 Single interface

The distribution of the transition radiation intensity with respect to the emission angle θ (between the emitted photon and the parent-particle trajectory) and the TR photon frequency, for a charge particle crossing a single interface, is:

$$\frac{d^2S_0}{d\theta d\omega} = \frac{2\alpha h\theta^3}{\pi}\left(\frac{1}{\frac{1}{\gamma^2}+\theta^2+\frac{\omega_1^2}{\omega^2}} - \frac{1}{\frac{1}{\gamma^2}+\theta^2+\frac{\omega_2^2}{\omega^2}}\right)^2 \tag{4.3}$$

where ω_i is the plasma frequency of the medium i, defined as

$$\omega_i = \frac{4\pi\alpha n_i}{m_e} \sim (28.8eV)^2\left(\frac{Z_i\rho_i}{A_i}\right) \tag{4.4}$$

where n_i is the electron density, Z_i and A_i the atomic number and weight, ρ_i the density of medium i, while α is the fine-structure constant. It can be shown that

TR photons are mostly emitted within a cone of half angle $\frac{1}{\gamma}$, which for relativistic particles practically implies that TR photons are emitted along the parent-particle trajectory. After integration over angles, the differential frequency spectrum is a monotonic function of the X-ray energy, as shown by the thin line in Fig. 4.3. This

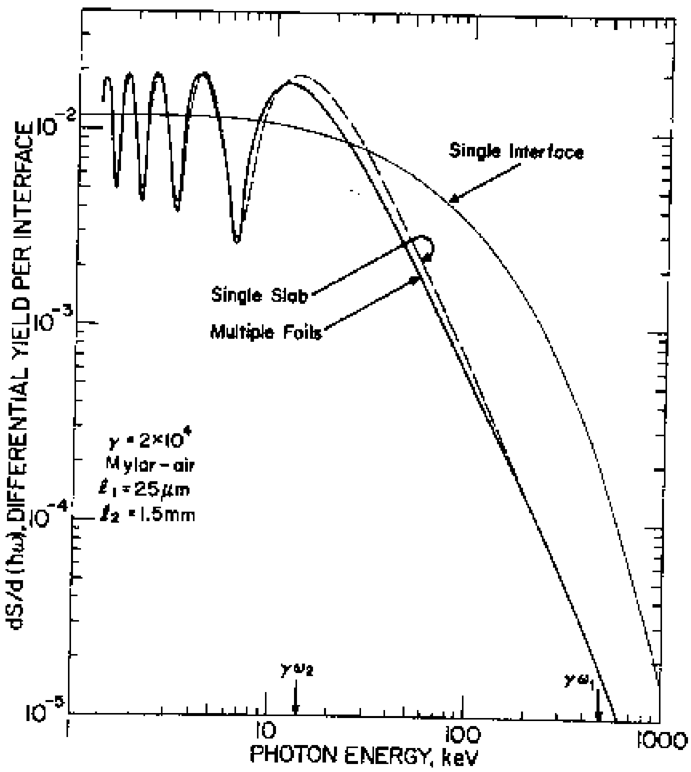

Figure 4.3: Differential yield per interface as a function of the photon energy. Results for single interface (monotonic thin line), single slab (dashed line), and multiple foils (thick line) are shown. The particle Lorenz factor is $\gamma = 2 \cdot 10^4$. From [24].

frequency spectrum may be divided in three regions:

- for small photon energies ($\omega < \gamma\omega_1$) the yield is constant;

- for intermediate photon energies ($\gamma\omega_1 < \omega < \gamma\omega_2$) the yield is logarithmically decreasing with ω;
- for large photon energies ($\omega > \gamma\omega_2$) the yield drops as $\frac{\gamma^4}{\omega^4}$.

The total radiation intensity is calculated by integration over angles and frequencies:

$$S = \frac{\alpha h Z^2}{3} \frac{(\omega_1 - \omega_2)^2}{\omega_1 + \omega_2} \gamma \tag{4.5}$$

The total intensity is of the order of magnitude of $\alpha = \frac{1}{137}$ and is directly proportional to γ, as shown by the thin line in Fig. 4.4.

4.2.2 Single foil

Single interfaces represent an ideal case, for any practical purpose foils of finite thickness are used. For a single foil (thin slab of material with thickness l_1 and two interfaces), the coherent sum of the radiation amplitudes from the two interfaces produces interference phenomena, which drastically modify the single-interface monotonic behavior in the differential spectrum, as shown by the dashed line in Fig. 4.3. Pronounced maxima and minima are clearly visible. The interference pattern is described by:

$$(\frac{d^2 S}{d\theta d\omega})_{foil} = \frac{d^2 S_0}{d\theta d\omega} 4 \sin^2 (\frac{l_1}{z_1(\omega, \theta)}) \tag{4.6}$$

This modulation depends, therefore, on the foil thickness and on the so-called formation zone (z_1), defined as:

$$z_1(\omega, \theta) = \frac{4c}{\omega} (\frac{1}{\gamma^2} + \theta^2 + \frac{\omega_1^2}{\omega^2})^{-1} \tag{4.7}$$

The formation zone can be regarded as the distance needed for particle and radiation to decouple. For foil thickness smaller than the formation zone, the intensity of

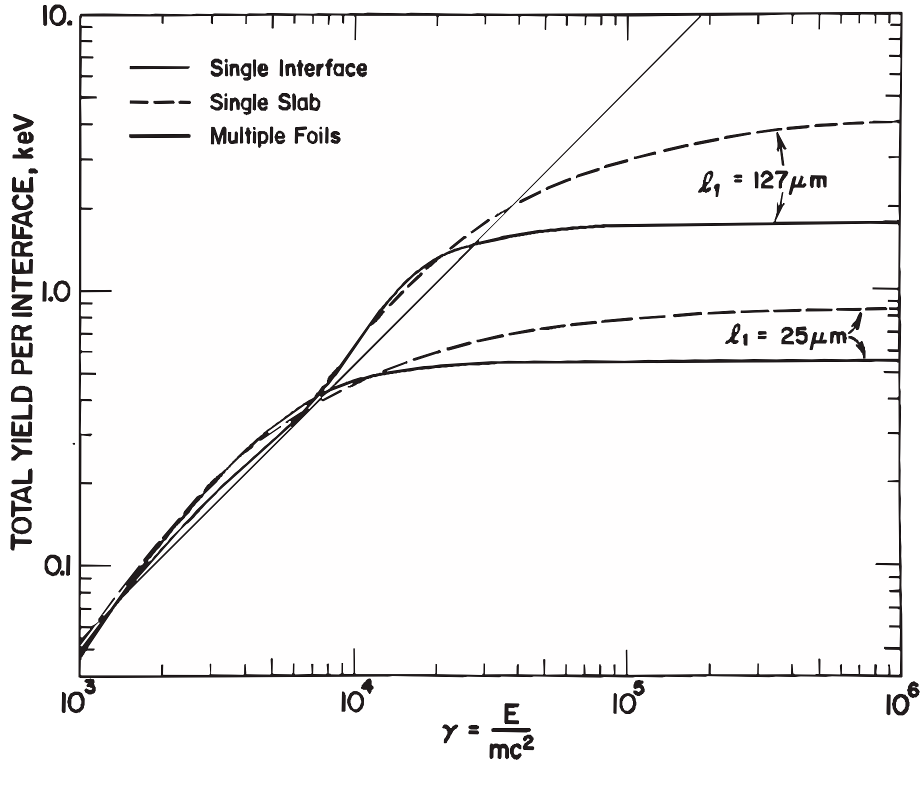

Figure 4.4: Comparison of the total generated yield per interface as a function of the particle energy for single interface (thin line), single slab (dashed line), and multi-foil radiator (heavy line). The yield is computed for Mylar-air interface, with foil thicknesses $l_1 = 25\,\mu$m and $127\,\mu$m, and spacing $l_2 = 25\,mm$. From [24].

the radiation deteriorates. For ultra-relativistic particles, in addition, the total yield saturates, as shown by the dashed lines in Fig. 4.4, for single foils with different thickness.

4.2.3 Radiator

A radiator is usually formed by several foils (of thickness l_1) placed at a regular distance l_2. The spectral intensity distribution is different with respect to the distribution for a single foil, due to interference effects for the amplitude for each foil, as shown by the thick curve in Fig. 4.3. For this radiator configuration, typical for particle detectors, the ratio $\frac{l2}{l1}$ is large (i.e. $\frac{l2}{l1} > 10$), and the shape of the spectrum is largely determined by the single foil interference. The multiple foil interference

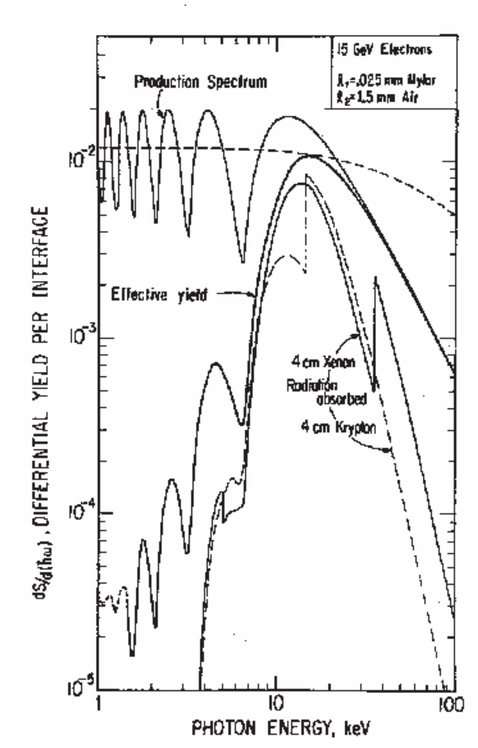

Figure 4.5: Differential yield per interface from 15 GeV electrons. Results for single interface (monotonic thin line) and multiple foils (of 25 μm thickness, spaced by 1.5 mm) (thick line) are the same as in Fig. 4.3. The effective yield observable at the exit of the radiator box, and the observable yield in a gaseous detector filled with 4 cm Xe or Kr is also shown. From [27].

governs, on the other hand, the saturation at high energy. The saturation of the total intensity for large γ for the radiator is shown by the thick line in Fig. 4.4, which shows that a radiator provides saturation of the transition-radiation total yield for a lower incident-particle energy with respect to the single foil. At saturation, and under the conditions $\omega_1 > \omega_2$ and $l_2 > l_1$, the frequency of the highest maximum is expressed by:

$$\omega_{max} = \frac{l_1 \omega_1^2}{2\pi c} \tag{4.8}$$

which shows how ω_{max} is proportional to the foil thickness and does not depend on the particle energy. An important effect using foils of finite thickness is the re-

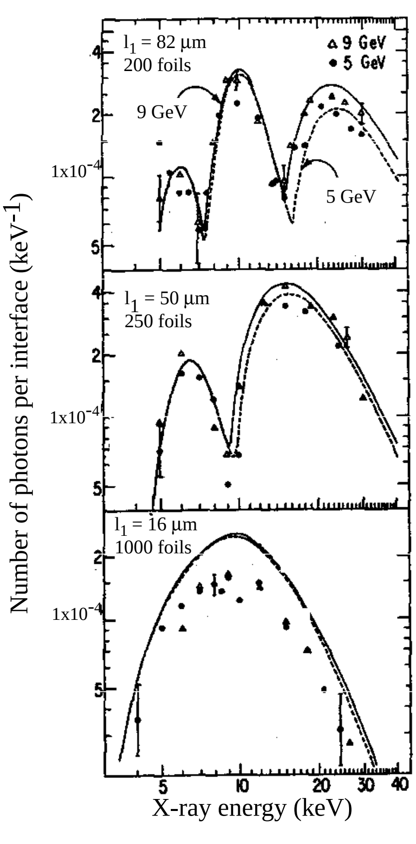

Figure 4.6: Frequency spectra of transition radiation emerging from three radiator with different foil thickness (from [26]). The points (black circles for 5 GeV and open triangles for 9 GeV electrons) represent measured data, while the curves (dashed line for 5 GeV and solid line for 9 GeV electrons) are results of calculations (see text).

absorption of the radiation by the material itself. The effect of the absorption is shown in Fig. 4.5 for the case of a polypropylene radiator. The effective yield curve shows the differential yield when absorption is taken into account; the lower photon energies are clearly cut off. The bottom plot in Fig. 4.5 represents the fraction of the effective yield that would be absorbed in detectors of 4-cm Xenon (solid line) or 4-cm Krypton (dashed line). In order to optimize this yield, the X-ray absorption cross-section of the detecting gas must obviously match very well the effective yield spectra.

The first experiments aimed to observe transition radiation concentrated on studies of the total yield (see for example [24]), while frequency spectra measurements were performed for the first time in 1976 by M. L. Cherry and D. Muller [26]. These latter measurements are shown in Fig. 4.6 for 5 and 9 GeV electrons incident into three radiators with different foil thickness but fixed spacing between them (1.5 mm). The number of foils was chosen in order to keep the total mass (and hence the photoelectric absorption) constant for the three radiators under study. The points represent the data, while the lines the theoretical calculations. The expected interference pattern was obviously very well reproduced by these measurements, while the absolute yield was lower than expected (the calculated spectra are shifted down by a 0.64 factor for a better comparison). Also to be noted that the radiation hardens with increasing radiator foil thickness; this feature allows one to design the system in such a way to make the radiation appear predominantly at frequencies where the detector is most sensitive.

Radiator chosen for the ATLAS TRT

Standard radiators for transition-radiator detectors consist of polypropylene foils ($\sim 15-20\mu$m thick) with regular spacing between them ($\sim 200-300\mu$m). These regular radiators provide the best TR yield, because the radiator parameters can be easily optimized for the particular detector considered. This foil radiator is used for the

ATLAS TRT end-caps. The plasma frequencies are $\omega_1 = 20eV$ for polypropylene and $\omega_2 = 0.7eV$ for air. For the barrel TRT, on the other hand, the modular geometry prevents the use of regular foil radiators and other solutions have been investigated. One of the first types of radiator investigated for the barrel TRT was the so-called foam radiator, which consists of a mixture of plastic and air with a certain average wall thickness and a certain average space between bubbles. Polyethylene gave the best result as a foam radiator, although its performance is quite far from the regular foil radiator. The solution finally adopted for the barrel TRT is the use of a fiber radiator. Recent studies show, in fact, that a radiator made of polyethylene/polypropylene fibers, oriented perpendicularly to the charged particle trajectory, is almost as efficient as regular foil radiators. A micro-photograph of such a radiator is shown in Fig. 4.7, where separate filaments of 15μm diameter can clearly be seen. The TR performance

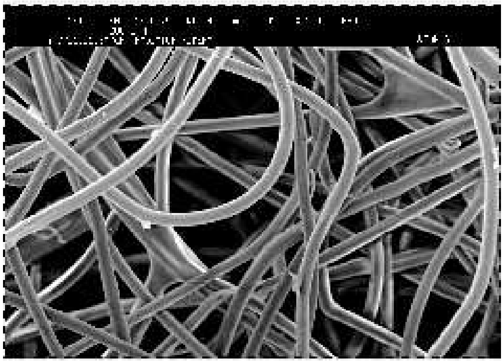

Figure 4.7: Micro-photograph of a sample of polyethylene fiber radiator.

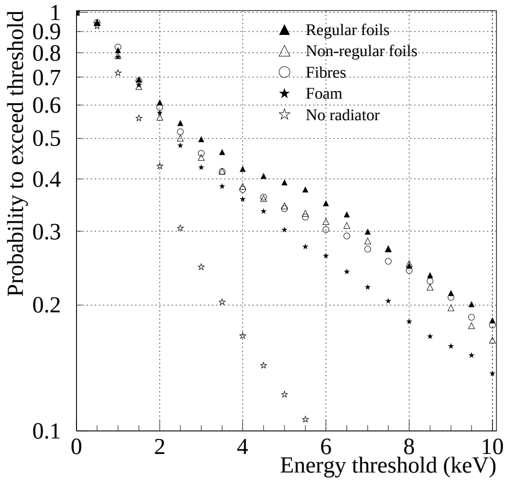

Figure 4.8: For 200 GeV electrons and for different type of radiators, probability per straw to observe an energy deposition above a given threshold.

of different radiators has been measured in a recent test-beam using 200 GeV electrons. The probability to observe in a single straw an energy deposition above a certain threshold is shown in Fig. 4.8 as a function of the threshold and for different radiator type. The fiber radiator clearly approaches the optimum TR yield, which is given by regular foil radiators.

4.3 Particle identification in the TRT

Transition-radiation photons, as described in the section above, are emitted at very small angle, and are therefore detected in the same straw as the ionizing particle. The absorption of the TR-photon in the straw gas gives rise to a very large point-like energy deposition. This highly-energetic cluster reaches the front-end electronics superimposed on the the usually lower-energy clusters due to track ionization. Very large energy depositions due to δ-rays constitute the main background to TR measurements. The front-end electronics, discussed in Section 3.6.1, was designed in order to tag a TR-photon candidate by discriminating the straw signal at a high-threshold, namely 5 keV, which is optimized for e/π separation using the cluster-counting technique.

4.3.1 Cluster-counting technique

Particle identification studies based on the cluster-counting technique with different TRT prototypes have been reported in [28, 29, 30]. In these studies, e/π separation was achieved by counting the number of high-threshold hits along the reconstructed track. For electrons, the tail above 5 keV is dominated by transition-radiation hits, while for pions it is mostly due to δ-rays. By requiring more than a certain number of high-threshold hits along the track, the probability to misidentify pions as electrons was measured as a function of the electron efficiency. The performance of this technique is shown in Fig. 4.9, as measured in a recent test-beam with an end-cap sector prototype, using 20 GeV pion and electron beams. The pion misidentification probability is shown as a function of the electron efficiency, while in the top left-hand corner the probabilities to observe a given number of high-threshold hits are shown.

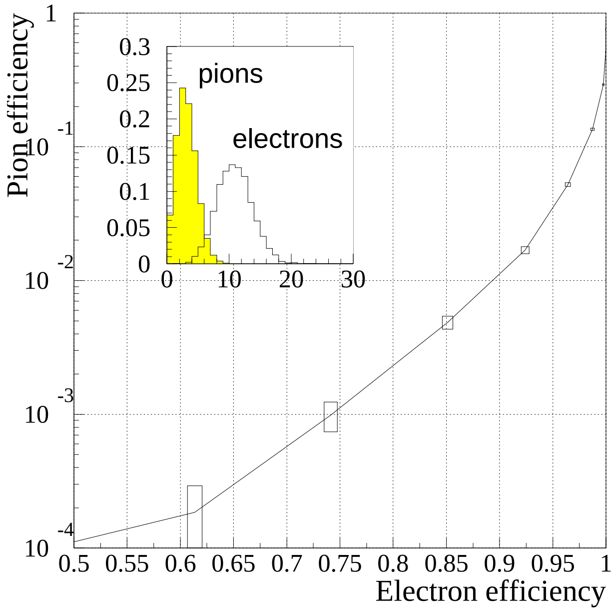

Figure 4.9: Pion misidentification probability as a function of the electron efficiency at 20 GeV, as measured using an end-cap sector prototype. The probabilities to observe a given number of TR-clusters for pions and electrons are shown in the top left-hand corner.

The application of this technique for the ATLAS detector is illustrated in Fig. 4.10, where a display of a simulated $B_d^0 \rightarrow \mathrm{J}/\psi\ K_s^0$ event (at low luminosity) in the ATLAS barrel TRT is shown, and in Fig. 4.11, where portions of a pion track from the K_s^0 decay and of an electron track from a J/ψ decay are shown in an enlarged frame (see box in Fig. 4.10). Dots represent straws crossed by charged particles. The electron track contains obviously many more high-threshold hits (larger points) than the pion track.

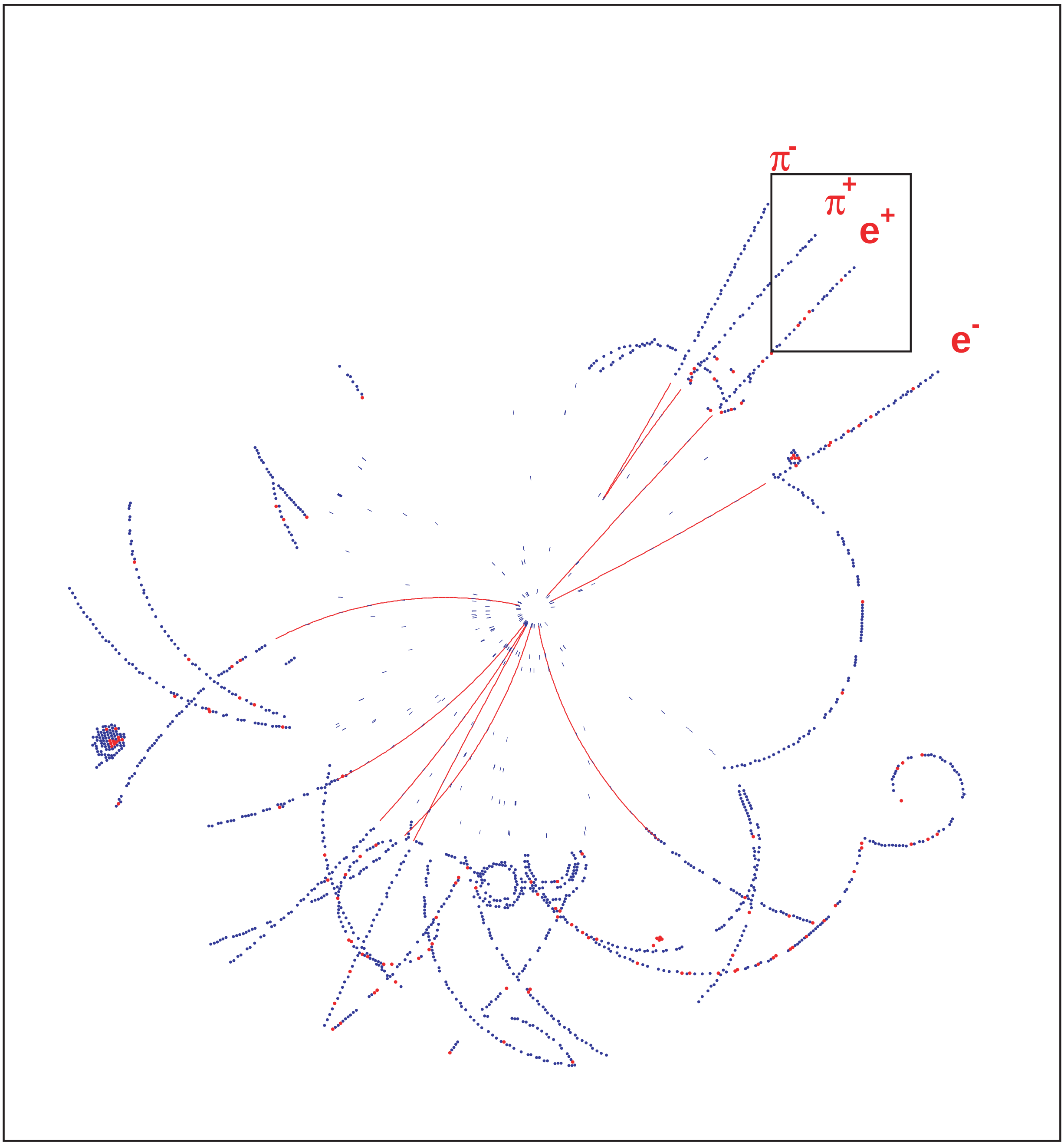

Figure 4.10: Display of a simulated $B_d^0 \rightarrow J/\psi\ K_s^0$ event in the ATLAS barrel TRT, at low luminosity. Reconstructed tracks are drawn as lines only up to a radius of 50 cm so as not to obscure the TRT hits. The small box selects a part of a pion track from the K_s^0 decay and of an electron track from a J/ψ decay (see Fig. 4.11).

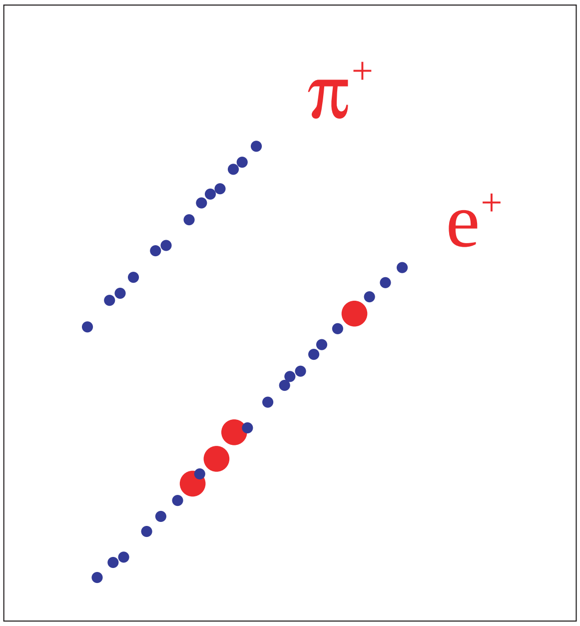

Figure 4.11: Expanded view of the portion of the tracks within the box in Fig. 4.10. The electron track contains many more high-threshold hits (larger points) than the pion track. Electron identification via transition radiation is based on this difference (see text).

4.3.2 Time-over-threshold method

The possibility of using the information from the low-threshold discriminator to improve particle identification in the TRT was discussed in previous works [31, 1]. The low-threshold discriminator level, as discussed in Section 3.1.1, is set to a nominal value of 200 eV, safely above the noise level ($\sigma \sim 40$ eV) and significantly below the average energy loss of ~ 2 keV, expected for minimum-ionizing particles traversing the straw gas. With this low-threshold setting, the front-end electronics was designed to detect the initial ionization cluster for precise drift-time determination.

A time-over-threshold technique for straw tubes, similar to the one discussed in this thesis, was discussed in a 1994 ATLAS internal note [31], whereas recent Monte

Carlo simulations [1] show that hadron identification in the TRT was possible by using the time of the leading-edge of the signal (above the low threshold), corrected as a function of track distance from the wire. This technique is based on the idea that larger energy deposition leads to faster rising time of the signal.

The development of a time-over-threshold method which includes corrections for the track position inside the straw [2] is discussed in this thesis. The time-over-threshold is defined as the width of the low-threshold discriminator signal. This signal width, larger for signals with larger amplitudes, contains partial information from $\frac{dE}{dx}$ (not complete information since the signal is not integrated but just discriminated). The Bethe-Bloch curves, reported in Fig. 4.12 for particles in the TRT gas mixture,

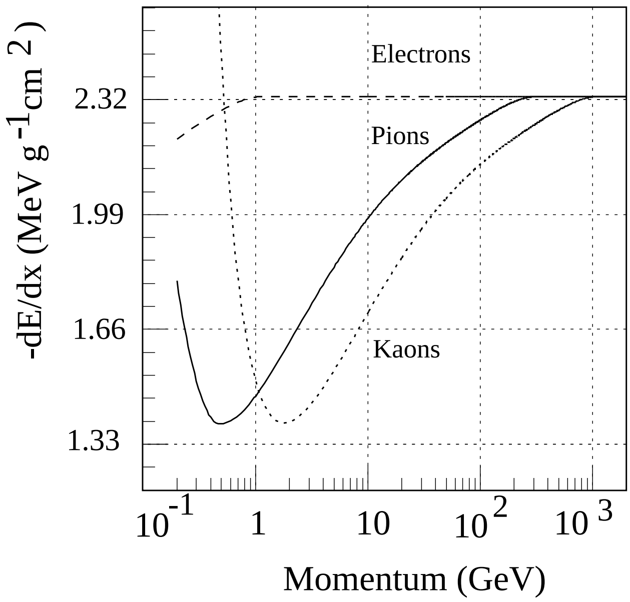

Figure 4.12: Bethe-Bloch curves for various particles in the ATLAS TRT gas mixture. For the energy range of interest for the TRT, electrons are always on the Fermi plateau, while hadrons are on the relativistic rise up to very large momentum.

show that for the momentum range of interest at the LHC, electrons are always on the

Fermi plateau, while hadrons are on the relativistic rise up to very large energy. As an example, a 10 GeV electron will lose in the straw gas more energy than a 10 GeV pion and therefore its time-over-threshold is expected, on average, to be greater.

However, the time-over-threshold also depends on the track position inside the straw, as illustrated in Fig. 4.13. For a track crossing the straw near the anode wire, the signal width is obviously larger than for the case when the track crosses the straw near the cathode. In order to extract information about the energy loss of a particle, it is important to correct for this dependence; this results in a significant improvement with respect to the method without track-position correction used in [31].

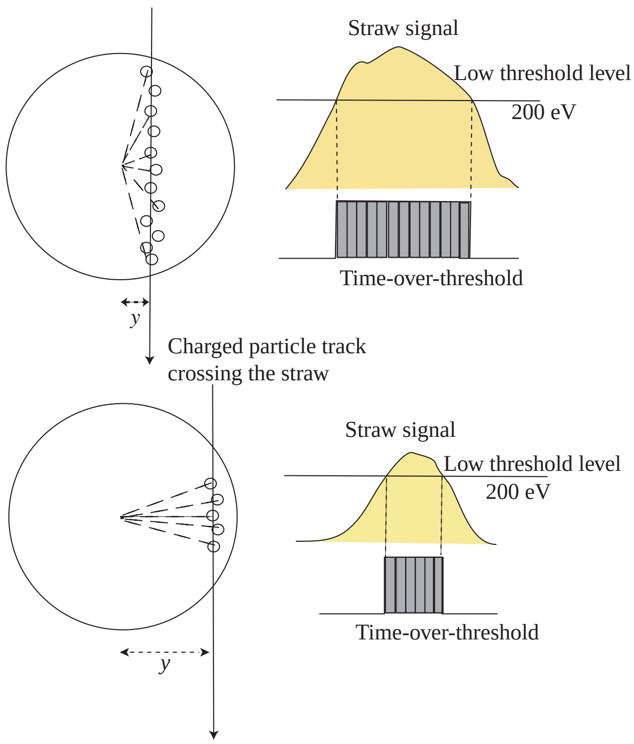

Figure 4.13: Dependence of the time-over-threshold on the track distance, y, from the wire. The straw signal is shown before and after the low-threshold (200 eV) discrimination.

Chapter 5

Test-beam experiment

Test-beam studies of the TRT straw tube performance in terms of electron-pion separation using the time-over-threshold method are described in this chapter. The test-beam experiment was performed in September 1999 in the H8 beam line at the CERN SPS, using 5, 10 and 20 GeV pion and electron beams.

The experimental set up is described in Section 5.1. A single TRT straw tube, equipped with a front-end analog chip very close to the final design, was used for the time-over-threshold measurements. In order to form an energy loss estimator from a single straw, these measurements were corrected for the position of the track inside the straw, according to the procedure described in Section 5.2.1. Pseudo-tracks were then created by randomly combining hits from different test-beam events, to simulate the situation expected in the ATLAS barrel TRT, according to the procedure described in Section 5.2.2. The performance obtained for the electron-pion separation is then outlined. A pion misidentification probability as low as 2.6% was measured at 5 GeV with the time-over-threshold method alone, for a 90% electron efficiency. Combining this method with the standard transition-radiation cluster-counting technique, an overall pion misidentification probability of about 0.4% was measured at 5 GeV, as discussed in Section 5.2.3.

5.1 Experimental set-up

The performance of the time-over-threshold method for electron-pion separation was evaluated in the H8 beam line at the CERN SPS. Pion and electron beams of different energies were used (20, 10 and 5 GeV). The experimental set-up is shown in Fig. 5.1.

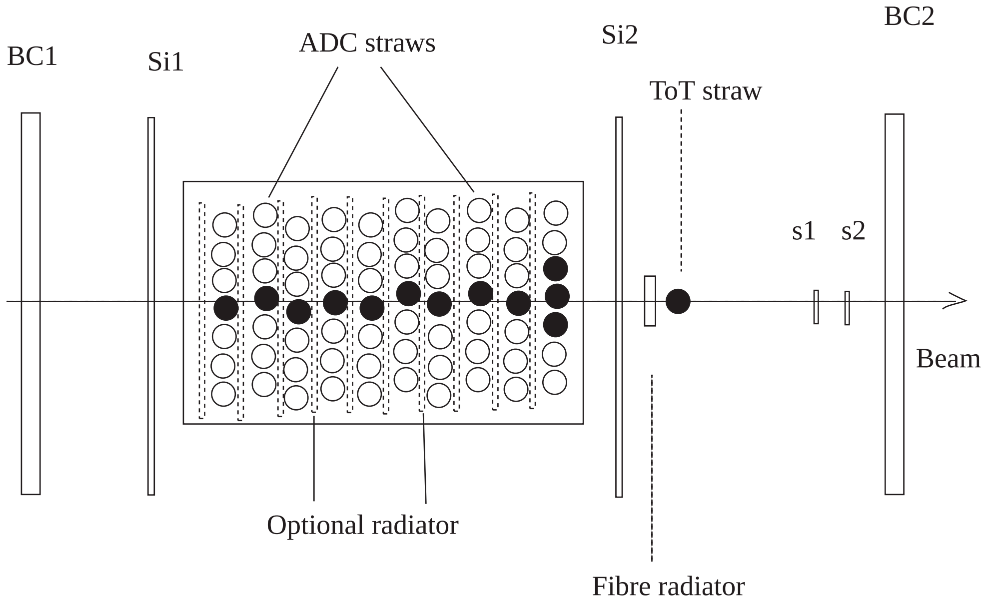

Figure 5.1: Schematic view of the experimental set-up (not to scale). MWPC's (BC1 and BC2) and silicon detectors (Si1 and Si2) were used for tracking, two scintillators (s1 and s2) were used in coincidence for triggering. Straws for radiator studies (ADC straws), the single straw for the time-over-threshold studies (ToT straw) and the radiator locations are also indicated. The straws that were read out are represented as black circles.

It included a small straw prototype used for precise ionization loss and transition-radiation measurements ('ADC straws'), and a single straw used for time-over-threshold measurements ('ToT straw'). Other equipment consisted of two standard multi-wire beam chambers (BC1 and BC2) for a first coarse track reconstruction, of two silicon detectors (Si1 and Si2) with an intrinsic accuracy of about 10 μm, which provided a very precise reconstruction of the beam track position in the TRT straws, and of two small scintillators (s1 and s2) used in coincidence as the trigger. Two Cerenkov detectors and a lead-glass calorimeter were also read out and used for particle identification.

The straw prototype, placed between the two silicon detectors, had 10 layers of straw drift-tubes, optionally interleaved with radiator (the presence and type of the radiator was run-dependent), and was read out with conventional ADCs. The information from these drift tubes was used to tune the Monte-Carlo model and to study the transition-radiation performance of different radiators inserted between them.

The single straw used for the time-over-threshold method was placed behind the second silicon detector, and was oriented at an angle of 21° from the perpendicular to the beam. A 12 cm thick fibre radiator was positioned in front of this straw, in order to simulate a straw at $|\eta| = 0.3$ in the ATLAS barrel TRT (see Section 6.4). This single straw was equipped with an amplifier-shaper-discriminator (ASDBLR), with low-level (200 eV) and high-level (5 keV) discriminator thresholds. For this study, the discriminated signal was fed into a multi-hit TDC, with a 1 ns resolution, that provided leading and trailing edge time information for both low and high-threshold signals.

Standard TRT 4 mm diameter Kapton straws with a 30 μm diameter gold-plated tungsten wire were used. The straws were 10 cm in length. The ionization gas mixture was 69.5%Xe + 22%CF_4 + 8.5%CO_2, very close to the one which will be used for the ATLAS TRT (70%Xe + 20%CF_4 + 10%CO_2). This gas mixture provides good absorption for photons in the X-ray region, a short total drift time of about 40 ns and good operational stability with respect to discharges. The gain was set to $2.5 \cdot 10^4$ and stabilized through a high-voltage feedback loop with an accuracy of better than 1%, as nominally required for operation in ATLAS .

5.1.1 Track reconstruction

The detectors used for track reconstruction, shown in Fig. 5.1, were two standard multiwire beam chambers (BC1 and BC2), with coarse resolution but excellent noise properties, and two silicon detectors (S1 and S2) which formed a very precise telescope. Each of those detectors is constituted by two planes of microstripes, oriented respectively along the x and the y directions. The track reconstruction was performed

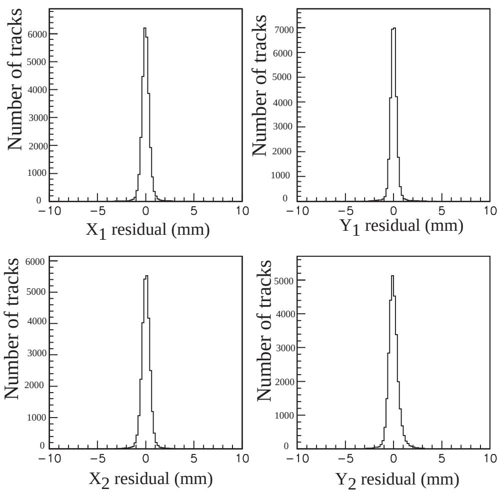

Figure 5.2: Extrapolation of the BC1-BC2 track to the silicon planes. The upper (resp. lower) distributions show the extrapolation of the track to S1 (resp. S2). The x (resp. y) residual is shown on the left (resp. right).

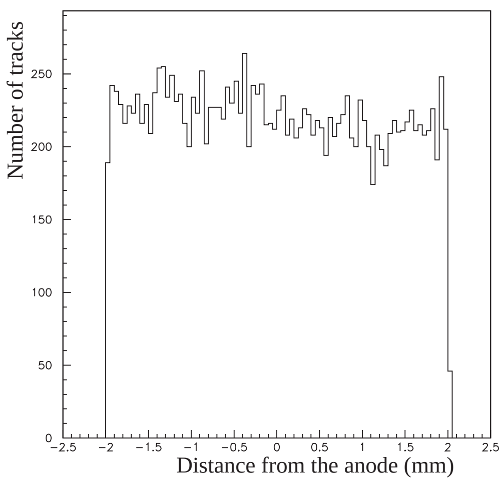

Figure 5.3: Extrapolation of the track coordinate inside the straw using the silicon telescope. The 4 mm window of the straw is uniformly illuminated by the beam.

using simple linear fits, since there was no magnetic field. A coarse track was reconstructed using hits from BC1 and BC2. The track was then extrapolated to S1 and

S2, and silicon hits associated to the track if found within a 1 mm window. In the rare case of multiple hits, the one closest to the track predicted coordinate was selected. The residuals for the track extrapolation to the silicon planes is shown in Fig. 5.2. A track candidate was then accepted if all the silicon planes satisfied this requirement. The track fit was then refined using the very accurate information from the silicon detectors. The track was then extrapolated to the straw, and the anode wire aligned by centering the track coordinate within the 4 mm window as shown in Fig. 5.3, which also indicates that the straw was fully illuminated by the beam. The time of the lead-

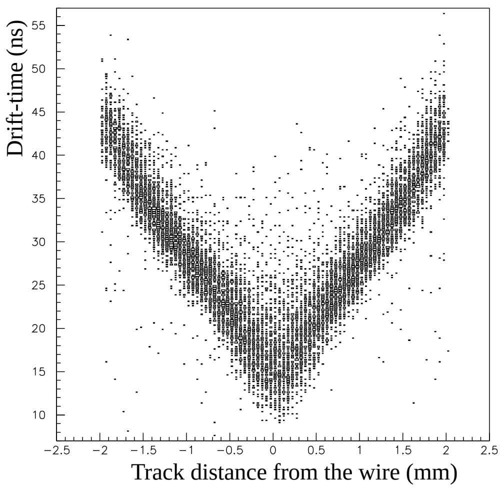

Figure 5.4: R-t dependence. The drift time is plotted as a function of the track distance to the anode wire, as extrapolated from the silicon telescope.

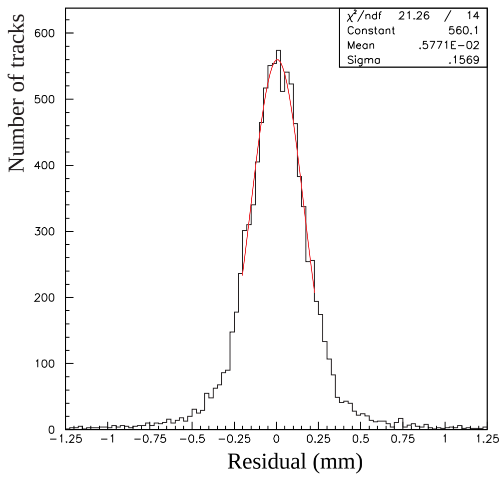

Figure 5.5: Residual between the extrapolated coordinate of the track inside the straw and the drift distance, as obtained using the R-t dependence.

ing edge of the straw signal above the low threshold (drift time) is shown in Fig. 5.4 as a function of the track distance from the anode wire, as extrapolated using the silicon telescope. By fitting this distribution with a third-degree polynominal, the so called R-t dependence is obtained, which is a universal formula that can be used to calculate the drift distance (i.e. the position of the track inside the straw) using the drift-time information. The width of the arms of that distribution depends on the straw-tube spatial resolution. The residual between the extrapolated coordinate of the track inside the straw and the drift distance is shown in Fig. 5.5. A spatial resolution ranging between 125 μm at 20 GeV and 155 μm at 5 GeV was achieved. The degradation at lower energy is due to multiple scattering in the material of the set-up.

5.1.2 Particle identification

The detectors used for particle identification (not shown in Fig. 5.1) were a Cherenkov counter and a leadglass calorimeter. The Cherenkov counter was placed ahead of BC1, while the leadglass detector was placed immediatly behind BC2. The Cherenkov

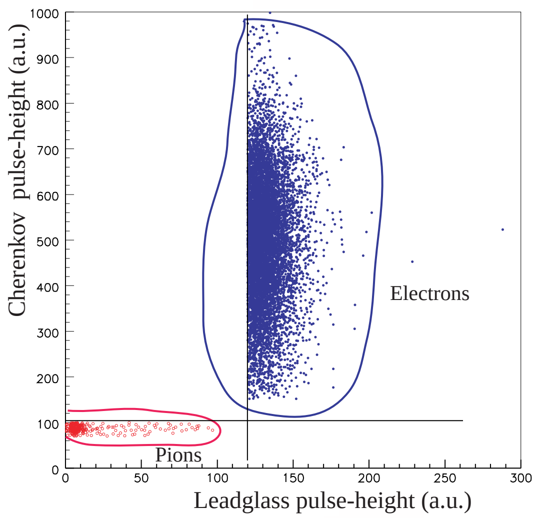

Figure 5.6: Particle identification in the test-beam experiment. The pulse-height from the Cherenkov counter is shown as a function of the pulse-height from the Leadglass calorimeter. Pions and electrons are obviously distributed in distinct regions. This distribution is shown after offline cuts on pulse-height.

detector used helium at 2 atm pressure as sensitive material. Particles with speed higher than the speed of light in the medium emit Cherenkov light, which is collected in photomultipliers and converted to an electric signal. In the leadglass calorimeter electromagnetic particles (like electrons and photons) produce showers, which result in a higher pulse-height with respect to other particles, like charged pions. Combining the information from those two detectors allows to clearly distinguish between pions and electrons, as shown in Fig. 5.6.

5.2 Time-over-threshold measurement

5.2.1 Time-over-threshold studies with a single straw

The results of the data analysis for the 'ToT straw' in the experimental set-up with all radiators in place (see Fig. 5.1) are discussed in this section. For this configuration, the amount of transition radiation generated by the 5, 10 and 20 GeV electrons corresponded to a probability of about 26% per straw for high-threshold hits, with energy above 5 keV, close to that expected in the ATLAS barrel TRT (see Section 6.4).

With incident pions, the high-threshold hit probability was about 6%, mostly due to large energy depositions caused by δ-rays, again close to that expected in the ATLAS barrel TRT.

The time-over-threshold method was evaluated in a way compatible with the ATLAS TRT electronics read out, by emulating the 3.125 ns DTMROC binning using the data obtained from the 1 ns TDC.

The uncorrected time-over-threshold data obtained in this way for the ToT straw and for 5 GeV pions (solid line) and electrons (dotted line) are shown in Fig. 5.7 and

Fig. 5.8. In Fig. 5.7, only hits without high-threshold discriminator level are included,

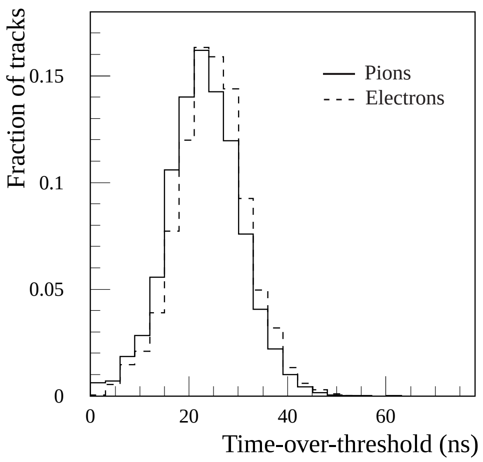

Figure 5.7: Uncorrected time-over-threshold distributions for 5 GeV pions and electrons for hits without high-threshold discriminator level.

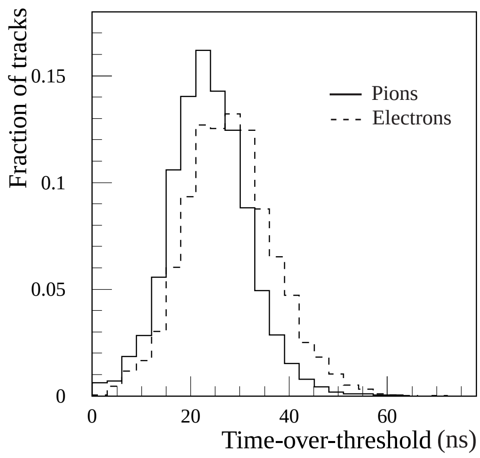

Figure 5.8: Uncorrected time-over-threshold distributions for 5 GeV pions and electrons for all hits.

since they provide a sample of hits used subsequently to build up a discriminating variable totally independent of the standard transition-radiation cluster-counting technique. In Fig. 5.8, all the hits are considered, and the difference between pions and electrons is, as expected, enhanced with respect to Fig. 5.7. The larger values in the time-over-threshold distributions of Fig. 5.8 are dominated by transition radiation for electrons and by δ-rays for pions.

The correlation between the uncorrected time-over-threshold and the distance of closest approach to the wire for 5 GeV pion data is shown in Fig. 5.9 for the sample without high-threshold hits. In order to parameterize this dependence, the straw was divided into 200 μm bins and the time-over-threshold was evaluated for each bin. The parameterization used a cubic polynomial.

The time-over-threshold residual, Δ_{ToT}, is then calculated as a function of y by

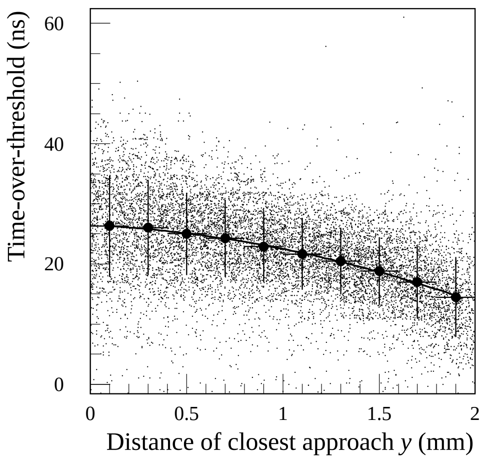

Figure 5.9: Parameterization of the dependence of time-over-threshold upon the distance of closest approach to the anode wire (y) for 5 GeV pions. The points represent the mean value for each y bin of width 200 μm, and the error bars represent the r.m.s. of the time-over-threshold distribution in each y bin.

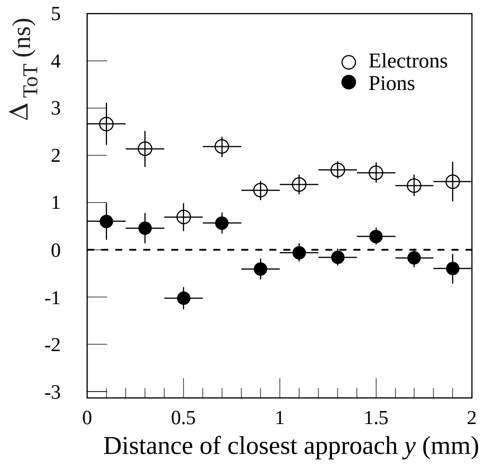

Figure 5.10: Correlation between the corrected time-over-threshold residuals (Δ_{ToT}) and the distance of closest approach for 5 GeV pions and electrons. The points represent the mean value for each y bin, and the error bars represent the statistical uncertainty on these mean values.

subtracting the parameterized pion time-over-threshold ($ToT_{\pi fit}(y)$) from the measured time-over-threshold ($ToT_{meas.}(y)$):

$$\Delta_{ToT} = ToT_{meas.}(y) - ToT_{\pi fit}(y).$$

This residual does not depend on the distance of closest approach (and therefore on the track length), as can be seen in Fig. 5.10. The values for pions are centered at zero, as expected, whereas those for electrons are shifted upwards on average by about 1.5 ns. The corrected Δ_{ToT} distributions for 5 GeV pions (solid line) and electrons (dotted line) are shown in Fig. 5.11 for straws without high-threshold hits.

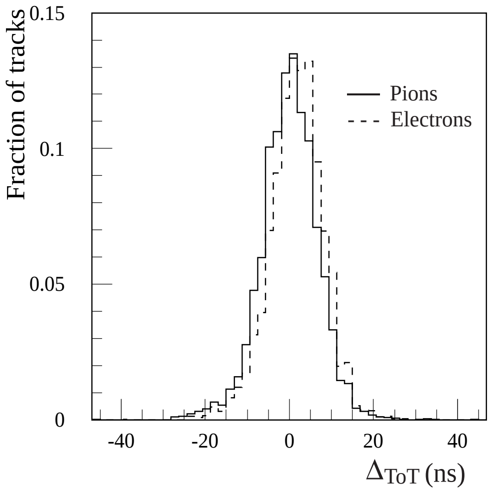

Figure 5.11: Corrected time-over-threshold residuals, Δ_{ToT}, for a single straw without high-threshold hits and for samples of 5 GeV pions and electrons (see text).

5.2.2 Time-over-threshold studies with pseudo-tracks

The energy loss measurements described above in detail for a single straw provide a powerful method for particle identification in gaseous detectors with many measurements available along the same track.

In the test-beam, there was just one straw, providing a single time-over-threshold measurement per track. In the ATLAS TRT, there will be on average 35 straws crossed per track and a large fraction of those will give a hit (i.e. will yield a measured drift time within a two-standard-deviation window from the reconstructed position of the track). The hit efficiency depends partially on η and largely on luminosity, as discussed in Section 3.2. For the study shown in this section, which will be compared to ATLAS prediction for single tracks at $\eta = 0.3$ (see Section 6.4.1), a hit efficiency of $\sim 90\%$ is assumed.

To simulate crudely the situation expected in the ATLAS experiment, pseudo-tracks were therefore created by randomly combining 32 hits (with a gaussian spread of three hits) from different test-beam events. This analysis was performed with 30000 pseudo-tracks for each beam energy and particle type.

A discriminating variable, $< \Delta_{ToT} >$, is formed by averaging the time-over-threshold residuals from n straws along the pseudo-track:

$$< \Delta_{ToT} > = \frac{\sum_i \Delta^i_{ToT}}{n} \text{ for } i = 1,...,n$$

Two $< \Delta_{ToT} >$ variables were studied: one used all hits available on the track; the other used only the hits without high-threshold discriminator level. These $< \Delta_{ToT} >$ distributions for pseudo-tracks are shown in Fig. 5.12 (no high-threshold hits) and Fig. 5.13 (all hits). The distributions of the number of high-threshold hits along the

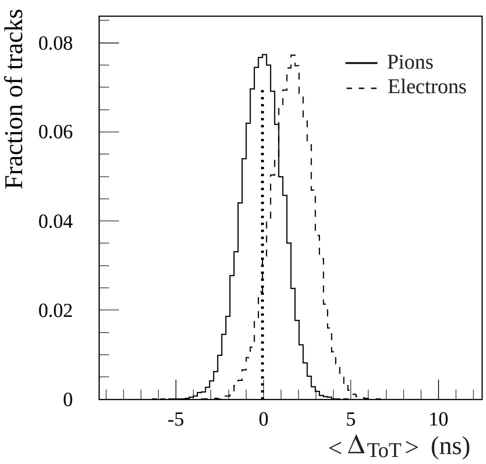

Figure 5.12: $< \Delta_{ToT} >$ (no high-threshold hits) for 5 GeV pseudo-tracks. The vertical line represents the $< \Delta_{ToT} >$ value for a 90% electron efficiency.

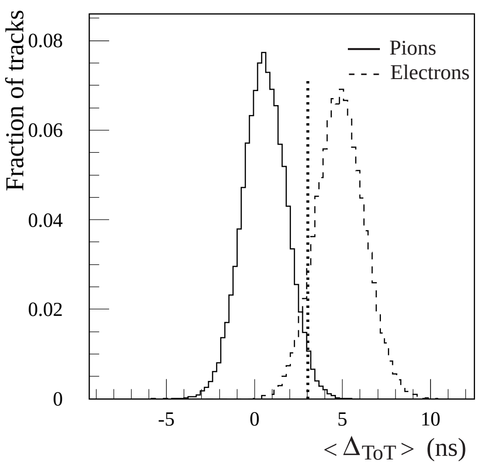

Figure 5.13: $< \Delta_{ToT} >$ (all hits) for 5 GeV pseudo-tracks. The vertical line represents the $< \Delta_{ToT} >$ value for a 90% electron efficiency.

reconstructed pseudo-tracks are shown in Fig. 5.14 for 5 GeV pions and electrons.

These distributions are the standard ones used for electron-pion separation using transition radiation.

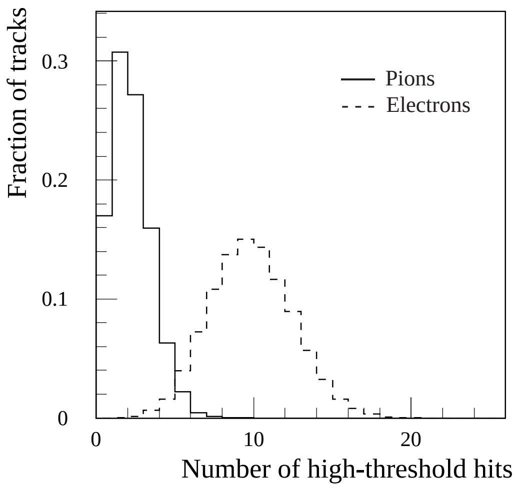

Figure 5.14: Number of high-threshold hits for 5 GeV pseudo-tracks.

5.2.3 Performance obtained for electron-pion separation

As illustrated in Fig. 5.13, an electron of 5 GeV can be identified with 90% efficiency, using the time-over-threshold technique described above, by requiring that $< \Delta_{ToT} >$ is above 3 ns. The fraction of pions passing this cut represents the pion misidentification probability. This pion misidentification probability is shown in Fig. 5.15 as a function of the electron efficiency for the two $< \Delta_{ToT} >$ variables, namely using all hits (large open circles) and using only hits without high-threshold discriminator level (large black circles). When $< \Delta_{ToT} >$ is used as the only discriminating variable, much better electron-pion separation is obtained of course if all the hits on the track are used. In particular, a pion misidentification probability as low as 2.6% can be achieved for a 90% electron efficiency at 5 GeV. In order to illustrate the importance of the correction for the track position inside the straw (discussed in Section 5.2.1), the results without this correction (small circles) are also shown in Fig. 5.15. In the

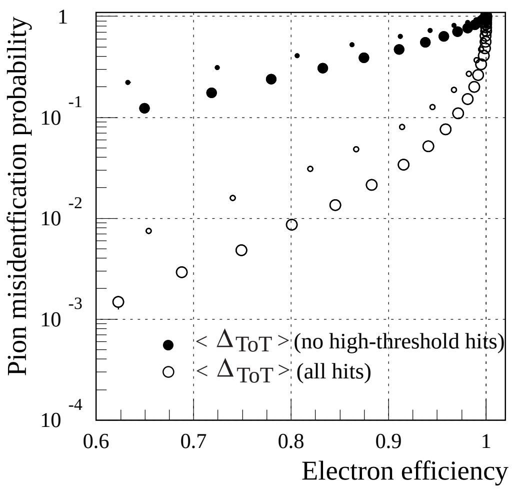

Figure 5.15: Pion misidentification probability versus electron efficiency, as obtained using $< \Delta_{ToT} >$ at 5 GeV for pseudo-tracks constructed from the test-beam data. The open circles are calculated using all the hits along the pseudo-track, whereas the black circles are calculated using only hits without high-threshold discriminator level. The large (resp. small) circles correspond to $< \Delta_{ToT} >$ corrected (resp. uncorrected) for the track position inside the straw.

case where all hits are used, the improvement obtained by using this correction is about a factor 2.5 for an electron efficiency of 90%.

In order to obtain the best possible electron-pion separation, the time-over-threshold has to be combined with the cluster-counting technique, that uses the number of high-threshold hits along the track. The correlation between $< \Delta_{ToT} >$ and the number of high-threshold hits is shown in Fig. 5.16 ($< \Delta_{ToT} >$ without high-threshold hits) and Fig. 5.17 ($< \Delta_{ToT} >$ with all hits) for 5 GeV electrons and pions. While there is now one more degree of freedom for optimizing electron identification, the two discriminating variables are correlated. The correlation is clearly stronger, as expected, when Δ_{ToT} is averaged over all the hits on the pseudo-track. A likelihood analysis

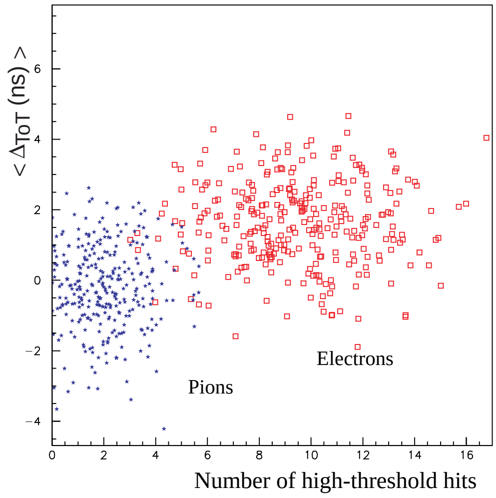

Figure 5.16: Distribution of $< \Delta_{ToT} >$ (no high-threshold hits) versus number of high-threshold hits for 5 GeV pseudo-tracks. Electrons are plotted as red squares and pions as blue stars.

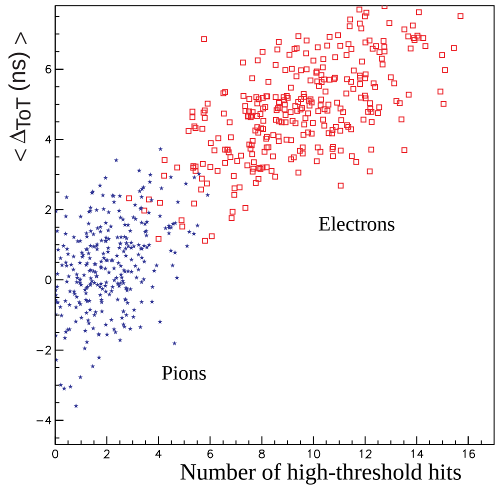

Figure 5.17: Distribution of $< \Delta_{ToT} >$ (all hits) versus number of high-threshold hits for 5 GeV pseudo-tracks. Electrons are plotted as red squares and pions as blue stars.

has been performed to combine the two variables in an optimal way for three different test-beam energies of 5, 10 and 20 GeV. The likelihood analysis shows that very similar overall performace is obtained by combining to the number of high threshold hits any of the two $< \Delta_{ToT} >$ variables. The likelihood distributions for pions and electrons are shown in Fig. 5.18. The pion misidentification probability at 90% electron efficiency for various time-over-threshold methods, for the cluster-counting technique and for the combined method is tabulated in Table 5.1 as a function of energy. The comparison between the electron-pion separation achieved at 5 GeV with the cluster-counting technique and the combined method is shown in Fig. 5.19, which can also be compared to Fig. 5.15, where only the time-over-threshold information is

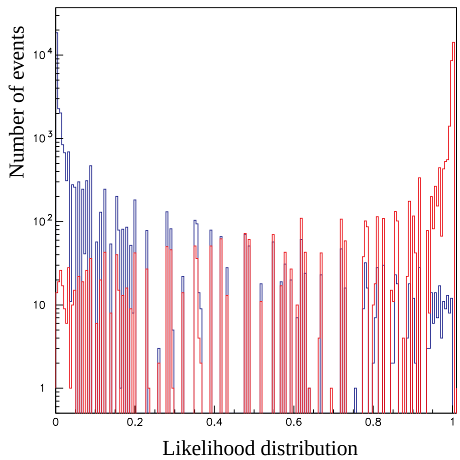

Figure 5.18: Likelihood distribution for pions (blue line) and electrons (red line), as obtained combining the two discriminating variables, namely the number of high-threshold hit and $< \Delta_{ToT} >$ (all hits).

Table 5.1: For a 90% electron efficiency and for pseudo-tracks constructed from test-beam data at three different energies, pion misidentification probability obtained using different techniques (see text).

Method	$E_b = 5\,\mathrm{GeV}$	$E_b = 10\,\mathrm{GeV}$	$E_b = 20\,\mathrm{GeV}$
Time-over-threshold (no high-threshold hits)	0.46 ± 0.01	0.58 ± 0.01	0.73 ± 0.01
Time-over-threshold (all hits, no y correction)	0.067 ± 0.002	0.10 ± 0.01	0.17 ± 0.01
Time-over-threshold (all hits)	0.026 ± 0.001	0.041 ± 0.001	0.10 ± 0.002
Number of high-threshold hits	0.0072 ± 0.0003	0.012 ± 0.001	0.017 ± 0.001
Combined method	0.0037 ± 0.0002	0.008 ± 0.001	0.016 ± 0.001

used. Table 5.1 clearly demonstrates that the cluster-counting information provides a rejection which is a factor 3.5 to 6 higher than that obtained with time-over-threshold alone. Nevertheless, the pion misidentification probability at 5 GeV and at 90% electron efficiency improves by a factor of 2 for the combined method with respect to the standard transition-radiation cluster-counting technique alone (see Fig. 5.19).

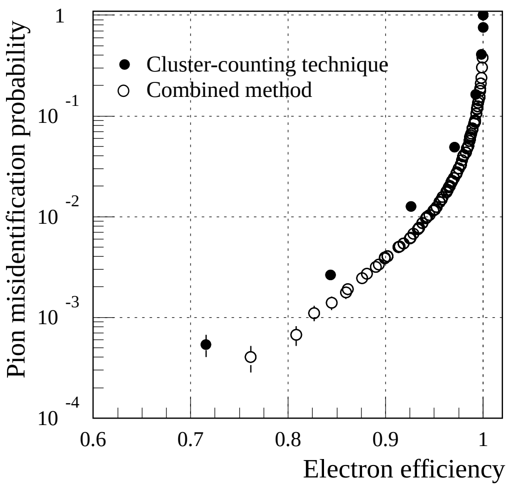

Figure 5.19: Pion misidentification probability versus electron efficiency at 5 GeV for pseudo-tracks constructed from test-beam data. The results are shown for the standard cluster-counting technique and for the combined method using also the time-over-threshold information (see text and Table 5.1).

Chapter 6

Monte Carlo simulation

This chapter describes how reliable predictions for the electron-pion separation in the ATLAS TRT detector have been obtained, based on single straw test-beam measurements discussed in Chapter 5. The Monte Carlo simulation of the test-beam experiment is described in Section 6.3, where it is shown that test-beam data are in agreement with test-beam Monte Carlo predictions. The expected performance for the electron-pion (resp. kaon-pion) separation in the ATLAS TRT are outlined in Section 6.4 (resp. Section 6.5). The parameterization of the time-over-threshold for kaons, pions and protons as a function of η and p_T is discussed in Section 6.6. This parameterization was used for the analysis of two B decays. The decay $B^+ \to K^+K^+\pi^-$, which may be relevant in the search for physics beyond the Standard Model is described in detail in Section 6.7, while a short description of the improvement obtainable using the time-over-threshold information for the decay $B^0_d \to \pi^+\pi^-$, useful to extract information about the angle α of the unitarity triangle used for CP-violation study, is given in Section 6.8.

6.1 Simulation framework

The framework for the simulation program for the LHC experiments is provided by a package called SLUG (Simulation for LHC using GEANT). SLUG provides the basic infrastructures for handling ZEBRA banks and a set of facilities for dealing with event generation, detector geometries and simulation.

The ATLAS simulation program is called DICE (Detector Integration for a Collider Experiment) [32]. It has continuously evolved in the last ten years, providing more accurate description of the detectors. The simulation of a LHC bunch crossing is very demanding, since on average an interesting physics event will be superimposed on 23 inelastic collision (the so called minimum-bias or pile-up events). The design of DICE permits the user to simulate single events of a given interesting physics process, and to add to it pile-up events in such a way to simulate a bunch crossing reliably. For the detector description, DICE uses the GEANT package. The DICE package provides the capability of writing dedicated routines to model the detector response. This option turns out to be very useful for processes where GEANT does not reliably reproduce the data, as in the case of ionization loss and transition radiation, whose modeling is described in Section 6.2.

The ATLAS simulation program can be logically divided into three separate modules, which communicate through a set of ZEBRA banks, namely the event generation, the detector simulation and the digitization. Event generation facilities are implemented within SLUG by using the GENZ package, which provides an interface between event generators and GEANT, via ZEBRA banks. Amongst the most widely used event generators, PYTHIA is worth mentioning since it has been used to generate the sample of $B \to KK\pi$ events for the analysis described in Section 6.7. Single-particle generators have been used, on the other hand, for single-track studies aimed to investigate the performance of the time-over-threshold method, both for the

ATLAS TRT geometry and for the test-beam set-up, reported in Section 6.3-6. The GENZ output bank is used as the input to the detector simulation.

6.1.1 GEANT

The GEANT package evolved over the past few years to simulate always more reliably the detector characteristics and performance. The GEANT 3.21 [33] version has been used for the final studies of the detector. The simulation program ideally should be able to describe in an as detailed a way as possible a broad range of physics processes. The most time-consuming physics processes to describe are showers in the calorimeter. In the electromagnetic shower development, for example, electrons and photons are tracked down just to an energy of 100 keV, and then forced to be absorbed by the detector. This approach has been validated against test-beam data, and illustrates the sort of compromise between the amount of detail needed to reproduce the detector response accurately and the amount of CPU needed for the simulation. In order to simplify the description of the ATLAS geometry in GEANT, a FORTRAN-based language (AGE, Atlas GEant) has been used to set up detector-description banks, to implement the detector geometry, and to define the HITS and DIGI structures (defined in the following sections) associated with it. Detector-description parameters are stored as well into a ZEBRA bank (DEPT bank, DETector Parameters), and can be overwritten interactively via datacards before they are used for the construction of the geometry.

Detector simulation

The detector simulation is the most time-consuming phase of the simulation; several different geometrical setups can be used for the same set of input physics events in order to understand the impact of changes in the detector on the physics performance. In the geometry modules for the individual sub-detectors, some regions are defined as active material; the effect of the interaction of incident particles with the active material are simulated by GEANT. For the TRT straw tube, for example, the energy deposited in the active gas by ionizing particles is recorded. This information is stored in the HITS banks; the particle four-vectors, on the other hand, are tracked through the various detector systems and stored in the KINE banks. The information collected in the HITS banks, although dependent on the geometry used by GEANT for event tracking, is nevertheless very general and independent of the detector readout structure. It normally consists of hit positions (for tracking detectors) and energy loss (for calorimeters), and provides the input for the detector response simulation, which takes place at the digitization step.

Digitization

The digitization procedure starts from the collection of all the hits from the HITS bank in any given detector element. This information is then processed in order to simulate the detector output. Detailed models to describe phenomena not well represented by GEANT can be implemented at this stage. In the case of the TRT, for example, the PAI (Photo-Absorption Ionization) model for the energy loss is implemented. Simulation of the front-end electronics response and noise injection are also introduced at the digitization level. The outputs of the digitization phase are the so-called digits, which are stored in the DIGI banks. The digits have a format similar to what can be expected from the readout electronics in the actual experiment, like the outputs of the discriminators in the case of the TRT straw tubes. The DIGI information is then used for the reconstruction of the event.

6.2 Simulation of the TRT straw tube response

The TRT simulation includes detailed models to describe the energy deposition in the straws, transition-radiation creation and absorption and the response of the front-end electronics [34]. Each straw tube is modeled individually as a GEANT tube, containing drift gas and a wire. The straw itself is 85 μm of Kapton and has an internal diameter of 0.4 cm. The straw wall is thicker than the actual straw wall, to allow for the mass associated with the four strengthening carbon fibres that are glued to the straw. The straw is filled with a mixture of 70%Xe, 20%CF_4, and 10%CO_2 at atmospheric pressure. Each straw is simulated with a central copper wire with a radius of 25 μm, which is positioned along the longitudinal axis of the straw. The time response model of the straw is composed by the following steps:

- The energy loss for each charged particle crossing the straw ionization gas is calculated using the Photo-Absorption Ionization (PAI) model [35]. In thin gas layers, the Landau model of the energy loss fluctuation does not work, since the number of primary collision is too small. The PAI model considers the atomic structure of the atom, and uses the photoelectric cross-sections to describe the energy loss distribution.

- This ionization is deposited over a small (typically $\sim$ 50 per cm for minimum-ionizing particles, while $\sim$ 70 per cm for particles at the Fermi plateau) number of primary ionization centers along the path length, as shown in Fig. 6.1. In addition, for a charged particle with a Lorentz factor above 1000, transition-radiation photons are generated in the radiator material, according to the formulae given in [24, 36]. This photon spectrum is transported along the particle track, partially absorbed in the radiator itself, in the straw walls, and in the gas mixture inside the straws. Transition-radiation photons deposit point-like ionization clusters in the same straws as those crossed by the parent particle.

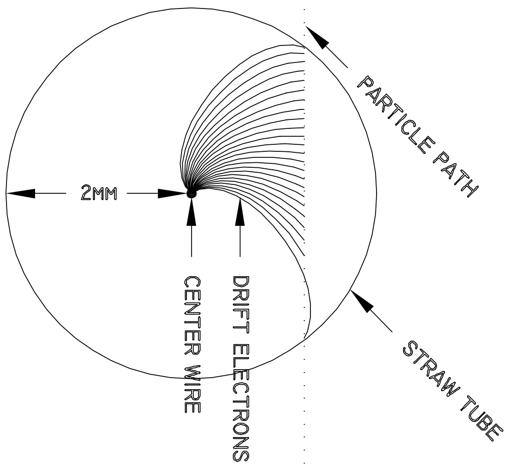

Figure 6.1: Illustration of how ionized electrons drift to the anode wire in a TRT straw, in the presence of both an electric and a magnetic field.

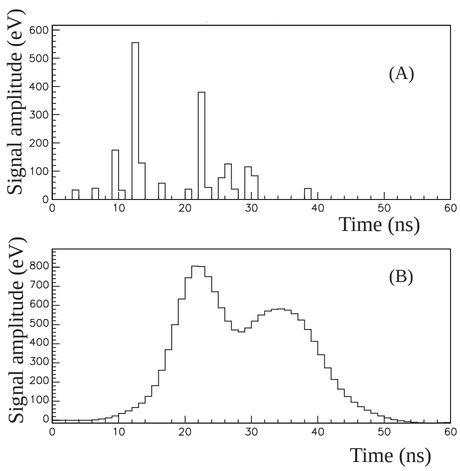

Figure 6.2: Monte Carlo simulation of the straw signal. (A) The ionization clusters drift towards the anode and the signal amplitudes and arrival times are recorded. (B) The straw output signal is then convoluted with a model of the response of the front-end electronics.

- The drift-time of each generated cluster to the wire is calculated using the measured electron-drift velocity [37]. This drift-time is then corrected for the flight and propagation times. The flight time is the time between the production of the particle and the time when it crosses the straw, while the propagation time is the time necessary for the signal to reach the front-end electronics. All the primary clusters are then allowed to drift towards the anode, as shown in Fig. 4.13, and the signal amplitudes and arrival times on the wire are summed over all primary clusters for all charged particles crossing each straw; this forms the straw output signal. Space-charge effects, that cause a reduction in the gain for large energy depositions are also simulated.

- This summed signal is then folded with a model of the electronics signal shape, based on the measurements of the response of the prototype electronics. The distribution of the pulse-height as a function of time is shown in Fig. 6.2.
- A low threshold and a high threshold are then applied. The amplified signal can fail to cross the threshold, cross the threshold once, or cross the threshold more than once.
- The discriminated signal is then digitized in 3.125 ns bins.
- The time of the leading edge of the signal above the low threshold is used to reconstruct the track coordinate using the established R-t dependence, as discussed in Section 5.1.1.

The spatial resolution depends on the energy and particle type, because of multiple scattering. For 20 GeV simulated single-track pions, the typical spatial resolution for single straw is $\sim 120\,\mu$m, in agreement with test-beam measurements. In the real detector, however, the overall spatial resolution is predicted to be $\sim 170\,\mu$m, due to systematic effects such as alignment errors and pile-up hits. In order to reproduce this resolution, the cluster arrival time is therefore jittered by $\pm$ 6 ns.

6.3 Simulation of the test-beam experiment

A Monte Carlo model, based on GEANT 3.21, has been developed to simulate the straws and the other detectors in the beam line, according to the experimental set-up shown in Fig. 5.1. The beam detector chambers and the silicon telescope, in particular, were simulated as well as the single straw equipped with the ASDBLR, the straws equipped with ADC and the different radiators. A single-track generator was used to generate pion and electron tracks with a given momentum along the z-axis (the direction perpendicular to the anode wire in the ADC straws). The ASDBLR straw was rotated by 21°, in order to reproduce the experimental conditions. Tracks were reconstructed according to the same procedure as described in Section 5.1.1.

In order to compare the PAI model with experimental data in detail for the ionization losses of pions and electrons, the pulse-height information from the straw prototype (for the configuration without radiators) placed between the two silicon detectors was used. The comparison between the Monte Carlo and experimental differential energy spectra is shown in Fig. 6.3 and 6.4, respectively for 5 GeV pions and electrons. The most probable energies are 1.1 keV for pions and 1.3 keV for electrons. The integral energy deposition spectra for 5 GeV pions and electrons and for data

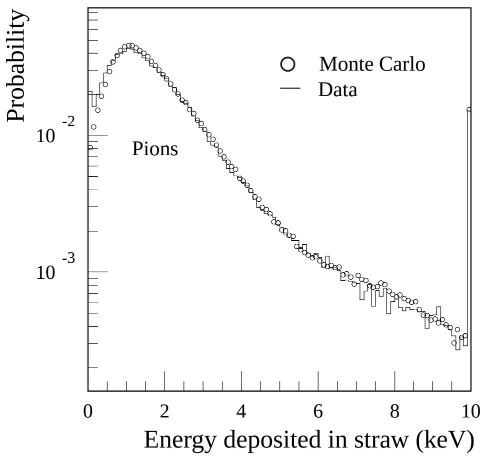

Figure 6.3: For a single straw without radiator and for 5 GeV pions, differential energy spectra from test-beam data (histograms) and Monte Carlo simulation (open circles).

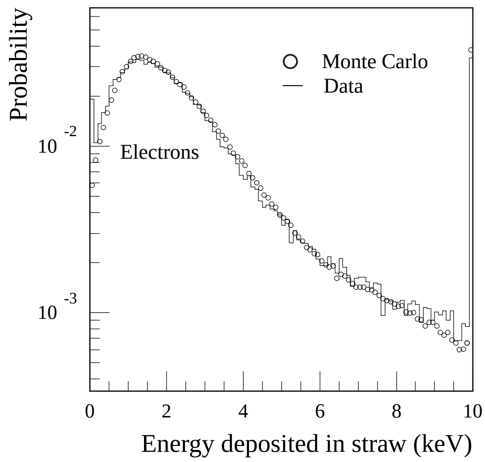

Figure 6.4: For a single straw without radiator and for 5 GeV electrons, differential energy spectra from test-beam data (histograms) and Monte Carlo simulation (open circles).

and Monte Carlo are shown in Fig. 6.5. The integral spectra are obtained from the differential spectra above the low threshold of 0.2 keV, chosen for the operation of the ATLAS TRT front-end electronics.

The good agreement observed between the Monte Carlo and the experimental data for the differential and integral spectra above 0.2 keV is an essential ingredient in the work required to obtain reliable predictions for the electron-pion separation to be expected in ATLAS using the methods described above.

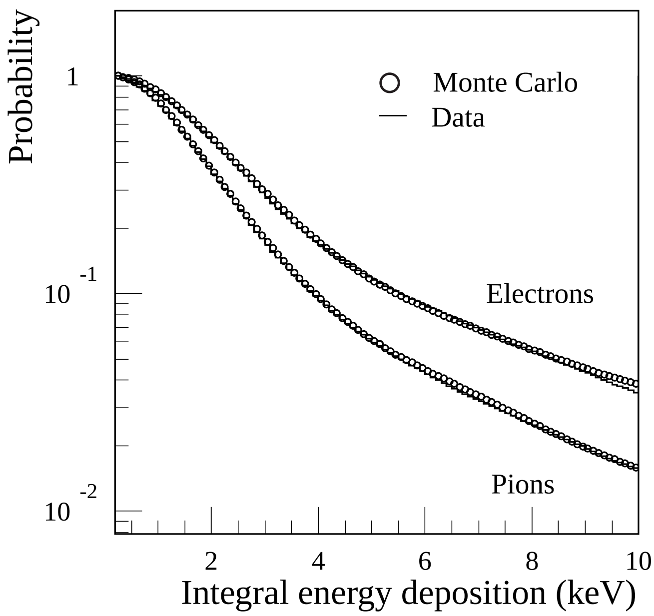

Figure 6.5: Integral energy deposition spectra (integrated above 0.2 keV) for 5 GeV pions and electrons, as measured in the test-beam and predicted by Monte Carlo simulations for a single straw without radiator.

The pion misidentification probability at 90% electron efficiency is shown as a function of energy in Fig. 6.6 for the test-beam data at 5, 10 and 20 GeV and for the Monte Carlo simulation. For both the Monte Carlo and the data time-over-threshold analysis, the same software chain has been used. The results are shown for pseudo-tracks and for the various methods described above. Additional Monte Carlo simulation results at lower energies (1 and 2 GeV) are also shown in Fig. 6.6. The four sets of points (data) and lines (Monte Carlo) represent (in order of decreasing pion misidentification probability) the time-over-threshold method alone (without using high-threshold hits and using all hits), the cluster-counting technique alone and the overall combined method. In the lower-energy region (1-2 GeV), where transition radiation production is not yet saturated, the time-over-threshold method is expected to improve the overall electron-identification performance by up to one order of magnitude.

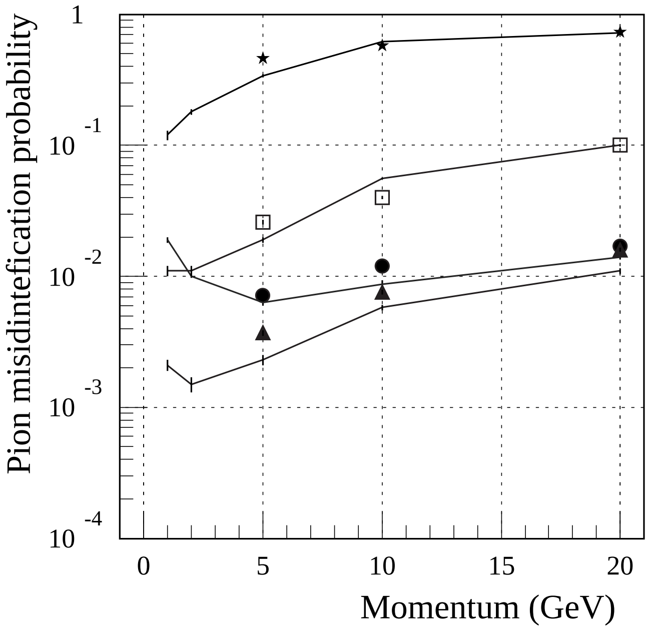

Figure 6.6: Pion misidentification probability as a function of momentum at 90% electron efficiency for pseudo-tracks in the test-beam setup. The performance is shown for $< \Delta_{ToT} >$, without using high-threshold hits (stars), for $< \Delta_{ToT} >$ using all hits (squares), for the transition-radiation cluster-counting technique (circles) and for the overall combined method (triangles). The test-beam data results at 5, 10 and 20 GeV are shown as points, while the Monte Carlo simulation results are shown as lines from 1 GeV to 20 GeV. The errors shown are statistical (above 5 GeV the errors are often smaller than the symbols).

6.4 Expected performance for e/π separation in the ATLAS TRT

The electron-pion separation was studied in more detail for the ATLAS TRT by using the full simulation (based on GEANT 3.21) of single particles without pile-up and with the overall straw response tuned to test-beam data. Tracks were generated in the barrel TRT, in a narrow region around $\eta = 0.3$ ($0.29 < \eta < 0.31$) and at different momenta. This η region corresponds approximately to the incidence angle of 21° of the beam tracks with respect to the straw axis in the test-beam setup. These

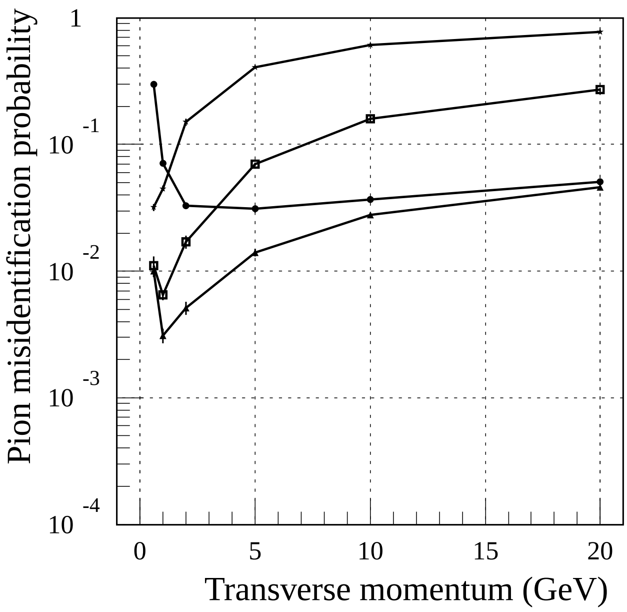

Figure 6.7: Pion misidentification probability as a function of transverse momentum at 90% electron efficiency for simulated single tracks at $\eta = 0.3$ in the ATLAS Inner Detector without pile-up. The performance is shown for $< \Delta_{ToT} >$ without using high-threshold hits (stars), for $< \Delta_{ToT} >$ using all hits (squares), for the transition-radiation cluster-counting technique (circles), and for the overall combined method (triangles).

detailed studies are necessary to validate the time-over-threshold predictions reported in Section 5.2.3, due to the somewhat different radiator geometry in the test-beam setup and since pseudo-tracks do not take into account possible correlations between successive straws on a track. Such correlations are expected to be energy-dependent to some extent and are due, in particular, to hadronic interactions, electromagnetic showers, high energy δ-rays and transition radiation.

The reconstruction of the tracks was performed using the XKALMAN pattern recognition code, which starts by associating hits in the TRT and then projects the track candidates back to the silicon hits [38]. Standard quality cuts were applied to select well reconstructed tracks, in particular more than twenty straw hits with a drift-time measurement within a $2\,\sigma$ window around the track were required.

The resulting pion misidentification probability is shown in Fig. 6.7 as a function of p_T, for a 90% electron efficiency and for the different methods discussed above. For a transverse momentum of 5 GeV, the time-over-threshold method improves the overall TRT performance by a factor of 2, while at even lower energies of 1-2 GeV the improvement is expected to be as large as one order of magnitude, in agreement with the test-beam data pseudo-track predictions discussed in Section 5.2.3.

6.4.1 Comparison between pseudo-tracks and the full ATLAS Monte Carlo

The performance predicted for the electron-pion separation with the full ATLAS simulation (see Fig. 6.7) is consistent with the studies done with pseudo-tracks obtained from test-beam data (see Fig. 6.6) for the time-over-threshold method without using high-threshold hits. However, the predicted performance of the time-over-threshold method with all hits, of the cluster-counting technique and of the combined electron-pion separation are significantly worse in the case of the ATLAS barrel TRT Monte Carlo.

In order to separate out the effect due to transition radiation from other effects, such as possible correlations between successive straws along a track (neglected obviously in the pseudo-track analysis described in Section 5.2), the radiator model used for the full ATLAS barrel TRT Monte Carlo was tuned to roughly reproduce the test-beam transition-radiation yields. As a result of this tuning, the radiator yield in the ATLAS barrel TRT Monte Carlo had to be increased by 20% to account for the differences between the radiator used in the test-beam and the radiator planned to be used for the barrel TRT. Tracks were then generated in the barrel TRT and compared to test-beam Monte Carlo pseudo-tracks, that have been shown in Section 6.3 to reproduce reliably the test-beam data. The resulting pion misidentification probabil-

Table 6.1: For a 90% electron efficiency, for different techniques and for different momenta, pion-misidentification probability as obtained from barrel TRT tracks and test-beam pseudo-tracks. The barrel TRT tracks were simulated at $\eta = 0.3$, corresponding to an incident angle close to the test-beam one.

Monte Carlo tracks type	p = 5 GeV	p = 10 GeV	p = 20 GeV
TR technique			
Barrel TRT tracks	0.007 ± 0.001	0.008 ± 0.001	0.012 ± 0.001
Test-beam pseudo-tracks	0.006 ± 0.001	0.009 ± 0.001	0.014 ± 0.001
ToT method (no HT hits)			
Barrel TRT tracks	0.41 ± 0.01	0.61 ± 0.01	0.77 ± 0.01
Test-beam pseudo-tracks	0.34 ± 0.01	0.62 ± 0.01	0.72 ± 0.01
ToT method (all hits)			
Barrel TRT tracks	0.031 ± 0.001	0.075 ± 0.001	0.14 ± 0.01
Test-beam pseudo-tracks	0.019 ± 0.001	0.056 ± 0.001	0.10 ± 0.01

ities at 90% electron efficiency are tabulated in Table 6.1, for the transition-radiation cluster-counting technique, the time-over-threshold method without high-threshold hits and the time-over-threshold method with all hits. The results are shown as a function of momentum for fully simulated tracks and for test-beam pseudo-tracks.

The results now show a good agreement between the predictions from barrel TRT tracks with tuned radiator performance and from test-beam pseudo-tracks, in the case of the standard transition-radiation cluster-counting technique. The discrepancies observed between test-beam pseudo-tracks and barrel TRT tracks, in the case of the time-over-threshold methods, are significant (up to $\sim 50\%$ in terms of pion misidentification probability) and are most likely due to the correlation effects mentioned above.

6.5 Expected performance for K/π separation in the ATLAS TRT

Hadron identification is obviously important for many aspects of B-physics studies, in the ATLAS experiment [39]. Earlier Monte Carlo studies of K/π separation using signal shape information from the ATLAS TRT are reported in [1]. In that work, only the expected shift in the time of the leading edge as a function of particle mass was used, and a maximum K/π separation of 0.9 standard deviation was predicted at 5 GeV momentum.

In this thesis, the time-over-threshold method is used, assuming that the TRT readout will provide this information at low luminosity while preserving the output bandwidth requirements. The analysis of the time-over-threshold follows the same procedure as described above and, obviously, all hits are used in this case. The expected $< \Delta_{ToT} >$ distributions for reconstructed tracks in the ATLAS barrel TRT at $|\eta| = 0.3$ are shown in Fig. 6.8 for 5 GeV pions and kaons. The expected K/π

separation as a function of transverse momentum is shown in Fig. 6.9 in units of standard deviation. Without including any pile-up effects, the K/π separation is predicted to be above one standard deviation for transverse momenta between 2 and 5 GeV, averaged over the full rapidity coverage (solid line), and above one standard deviation over a broader p_{T}-range between 2 and 15 GeV at $|\eta| = 0.3$ (dotted line).

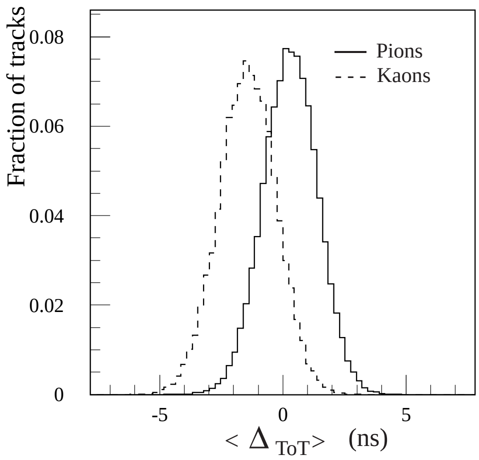

Figure 6.8: $< \Delta_{ToT} >$ (all hits) for reconstructed tracks in the ATLAS barrel TRT at $|\eta| = 0.3$ for 5 GeV pions (solid line) and kaons (dashed line).

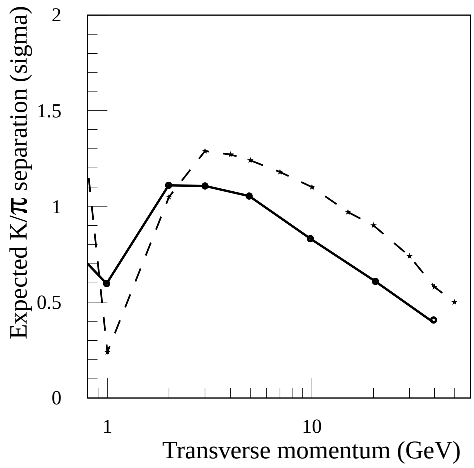

Figure 6.9: Expected K/π separation in the ATLAS TRT as a function of transverse momentum (no pile-up effects included). The separation is shown as an average over the full rapidity coverage (solid line) and at $|\eta| = 0.3$ (dotted line).

6.6 Parameterization of the $\frac{dE}{dx}$ estimator

In order to study real physics processes in the ATLAS experiment, the mean and the sigma of the $< \Delta_{ToT} >$ distributions, well described by gaussians, were parameterized as a function of p_{T} and η over the full acceptance region of the ATLAS TRT. The comparison between the mean of the dE/dx distribution for pions, kaons and protons as a function of η is shown in Fig. 6.10 for p_{T}=10 GeV particles, while the corresponding distributions for the sigma are shown in Fig. 6.11.

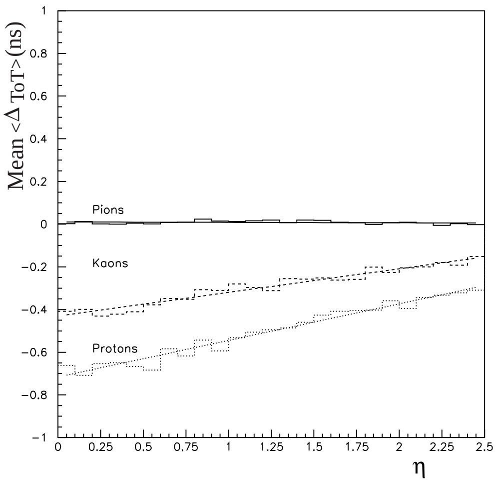

Figure 6.10: Parameterization of the mean of the dE/dx distribution as a function of η for p_{T}=10 GeV pions, kaons and protons (shown in order of decreasing average mean).

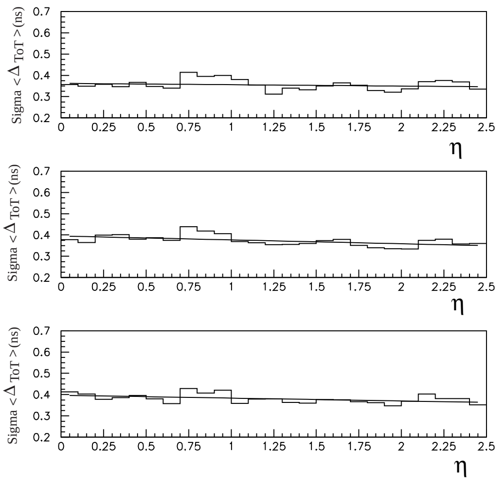

Figure 6.11: Parameterization of the sigma of the dE/dx distribution for 10 GeV p_{T} pions (upper plot), kaons (central plot) and protons (bottom plot).

Both the mean and the sigma of the dE/dx distribution have been parameterized as a straight line as a function of η and for fixed p_{T}, as shown in Fig. 6.10 and 6.11. The coefficients of this straight line fit, namely the intercept ($a_0^{p_T}$) and the slope ($a_0^{p_T}$), have then been parameterized as a function of p_{T}, as shown for the kaons in Fig. 6.12 and Fig. 6.13. Linear interpolation was used for this latter parameterization.

6.7 Study of the $\mathrm{B}^+ \rightarrow \mathrm{K}^+\mathrm{K}^+\pi^-$ decay

The observation potential of the decay $\mathrm{B}^+ \rightarrow \mathrm{K}^+\mathrm{K}^+\pi^-$ with the ATLAS detector at LHC is described in this section [3]. Many B-meson decays have been considered for observing effects originating from physics beyond the Standard Model (SM). Flavour

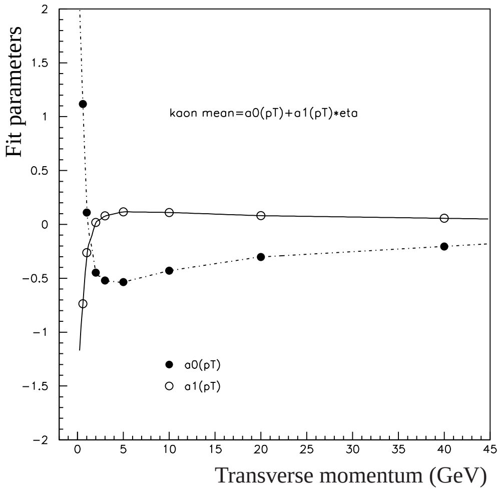

Figure 6.12: Parameterization of the straight line fit parameters of the mean of the dE/dx distribution as a function of p_{T} for kaons.

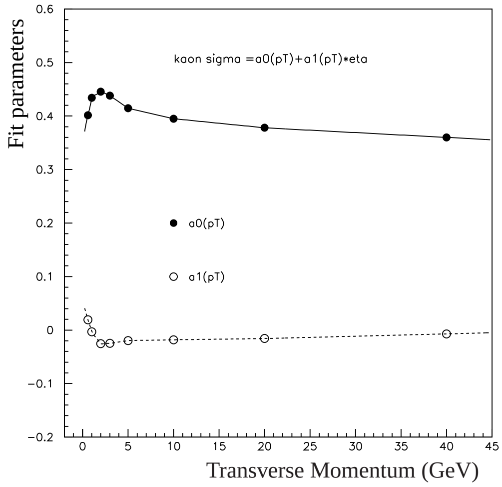

Figure 6.13: Parameterization of the straight line fit parameters of the sigma of the dE/dx distribution as a function of p_{T} for kaons.

Changing Neutral Currents (FNCN) processes such as $\mathrm{b} \to \mathrm{s}\gamma$ have been analyzed, but theoretical uncertainties hamper the observation of new physics signatures [40, 41]. Channels such as $\mathrm{b} \to \mathrm{sq\bar{q}}$ [42] and $\mathrm{b} \to \mathrm{sl\bar{l}}$ [43] also suffer from large theoretical uncertainties. Other processes such as $\mathrm{B} \to \tau$ have been shown to be rather insensitive to a large class of new physics models [44].

New physics can be probed efficiently with the study of decays with extremely tiny branching ratios predicted by the Standard Model. The $\mathrm{B}^{\pm} \to \mathrm{K}^{\pm}\mathrm{K}^{\pm}\pi^{\mp}$ is a decay mode which is strongly suppressed in the SM. This decay can be produced in the SM by box diagrams (see Fig. 6.14a) with an estimated branching ratio at a level lower than 10^{-11}. The Minimal Supersymmetric Standard Model (MSSM) introduces squark-gaugino (or higgsino) box diagrams (see Fig. 6.14b), raising the estimated branching ratio to $10^{-7} \sim 10^{-8}$ [45]. Supersymmetry with broken R parity provides a model with a significant enhancement of this decay as well (see Fig. 6.14c). The decay has also been studied in several Two Higgs Doublet Models that could lead to a branching ratio at the level of 10^{-7} [46].

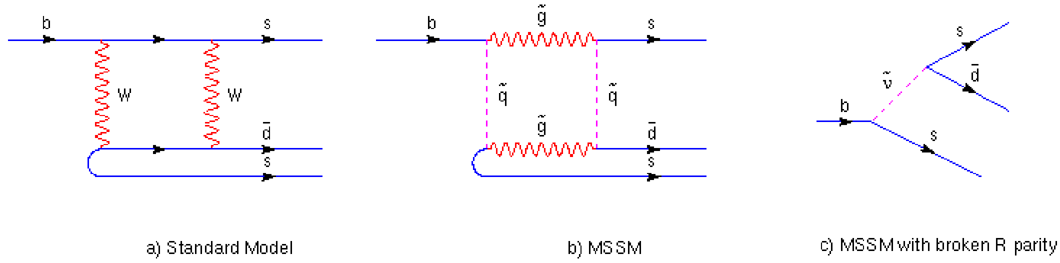

Figure 6.14: Feynman diagrams contributions to $b \to ss\bar{d}$ decay in various models. From [3].

An upper limit of 8.79×10^{-5} for the branching ratio $\mathrm{BR}(\mathrm{B}^{\pm} \to \mathrm{K}^{\pm}\mathrm{K}^{\pm}\pi^{\mp})$ was recently set by the OPAL collaboration, at a 90% confidence level [47] .

6.7.1 Event simulation

The $\mathrm{B}^{+} \to \mathrm{K}^{+}\mathrm{K}^{+}\pi^{-}$ decay was implemented in the Monte Carlo program Pythia5.7 [48] in order to generate the signal sample, using the ATLAS B-physics event generation framework [1]. In the event generation, b-quark pairs were produced either directly via the lowest order process, or via gluon splitting or flavour excitation.

Events containing a B^{+} meson were selected, and then the B^{+} was forced to decay into a $\mathrm{K}^{+}\mathrm{K}^{+}\pi^{-}$ final state. The associated $\bar{\mathrm{b}}$ was forced to decay semileptonically into μX, in order to satify the level-1 trigger requirements for B-physics (a muon with a $p_{\mathrm{T}} > 6$ GeV and $|\eta| < 2.4$).

The second level trigger for this hadronic B decay could be envisaged to be the presence of three charged particles with $p_{\mathrm{T}} > 1.5$ GeV, forming an invariant mass close to the B-meson mass. The detailed trigger rates have not yet been studied.

[1]http://msmizans.home.cern.ch/msmizans/production/0.html

For the background, one million $b\bar{b} \rightarrow \mu X$ events were generated. An important physics background to the $B^+ \rightarrow K^+K^+\pi^-$ signal could be the $B^+ \rightarrow K^+pi^+\pi^-$ decay, which was not studied in this analysis.

6.7.2 Fast simulation parameterization

A fast simulation program was used instead of the full GEANT simulation. The parameterization was established by studying in detail the resolutions of the five helix parameters of the tracks in fully-simulated samples, including tails ([49],[50]). The smeared five helix parameters of the track and the corresponding covariance matrix were obtained, and a look-up table as a function of p_T and η was produced. The parameterization was then applied to the four-momenta of the generated particles. In case of pions, the parameterization included a dependence on the decay radius as well, in order to be able to describe pions coming from the decay of long lifetime particles such as K^0_S. The parameterization handles differently muons, electrons and hadrons. Muon resolutions in fully simulated samples did not show appreciable tails and so they were parameterized with Gaussian functions as a function of p_T and η. Electron resolutions, on the contrary, showed a non-Gaussian behaviour which is due to interactions with the Inner Detector material. To take this effect into account, electron distributions were parameterized allowing for a single hard bremsstrahlung, chosen at random from the appropriate distribution.

The parameterization for pions was established by studying the resolutions of the five track parameters in fully-simulated samples. The total sample was divided into bins of p_T, η and decay radius R. In each bin, the track parameter resolutions were described as the sum of two Gaussians in order to take into account the presence of tails. This method allows for obtaining a parameterization of the full covariance matrix (including the correlation terms) as a function of p_T, η and R. This parameterization was used to smear the five generated pion-track parameters in the fast-simulation program.

6.7.3 Analysis

Several variables were used in order to select efficiently the signal, while rejecting as much background as possible. The invariant mass spectra for the signal (red line) and the background (blue line) is shown in Fig. 6.15. For the background, all possible triplets of two positive and one negative curvature tracks were considered. These spectra are obviously not normalized for the number of events expected at the LHC. The χ^2 distribution of the B-vertex fit and the transverse momentum distribution of

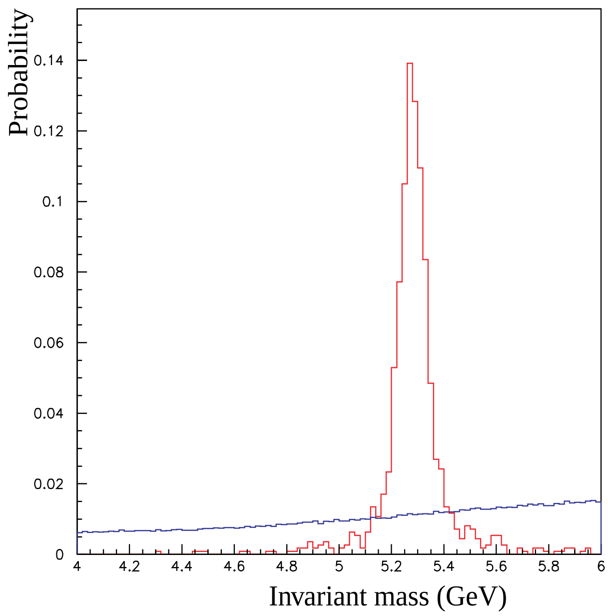

Figure 6.15: Invariant mass for all the possible triplets of two positive and one negative curvature tracks. These spectra are not normalized for the number of events expected at the LHC (see text).

the B candidate are shown respectively in Fig. 6.16 and Fig. 6.17. The distribution of

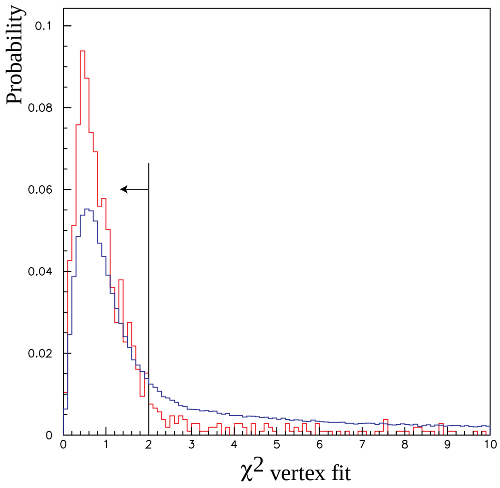

Figure 6.16: The χ^2 distribution for the B-candidate vertex fit. The signal is shown as red line, while the background as blue line.

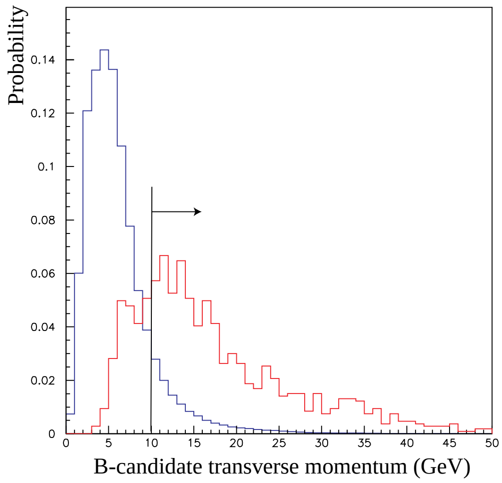

Figure 6.17: Transverse momentum distribution for the B candidate. The signal is shown as red line, while the background as blue line.

the signed distance between the primary vertex and the secondary vertex in the radial plane is shown in Fig. 6.18. The sign of this distance is calculated using information from the momentum of the B candidate just before its decay. The distance is positive for the signal, since the momentum of the B candidate points always away from the primary vertex, while it is spread around zero for the background, since in this case there is no preferred direction for the reconstructed momentum with respect to the primary vertex. The Dalitz plot for the signal is shown in Fig. 6.19, where the invariant mass squared $m^2_{\pi K_1}$ is shown versus $m^2_{\pi K_2}$.

Event selection

The event selection cuts are summarised in Table 6.2. The cuts on the transverse momentum of the particles and the loose cut on the B-candidate mass emulate the second-level trigger requirements. The other selection criteria are based on the quality of the B-vertex fit, on the transverse momentum and on the long lifetime of the B

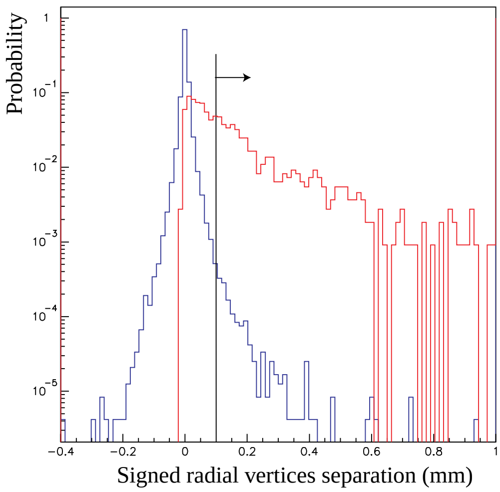

Figure 6.18: The distribution of the distance (in mm) between the primary and the displaced vertex. The signal is shown as red line, while the background as blue line.

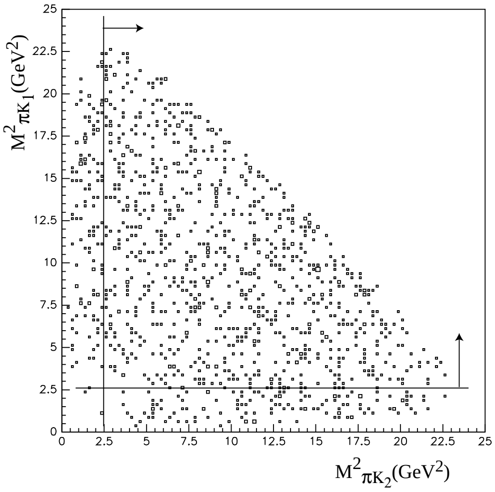

Figure 6.19: Dalitz plot for the signal. The invariant mass squared $m^2_{\pi K_1}$ is shown versus $m^2_{\pi K_2}$.

meson (the reconstructed B vertex is required to be separated from the primary vertex with at least 100 μm in the transverse plane), on the rejection of events in which two of the particle pairs form masses close to light resonance masses, and on the probability that the three particles form a KKπ combination. The last selection criterium is explained in more detail in the next subsection. The resolution of the decay length in the transverse plane is 72 μm. All cuts are applied in sequence.

The overall signal efficiency was found to be 11.6%, while the background efficiency was $2.8 \cdot 10^{-4}$ %. The study of the background rejection was limited by the statistics of the simulated background sample.

The invariant mass plot, after applying all the cuts described above, is shown in Fig. 6.20.

Cuts	Signal efficiency	Background efficiency
p_T(tracks) $> 1.5\,\mathrm{GeV}$	50.9%	68.8%
4 GeV < M(B) < 6 GeV	97.7%	53.1%
χ^2(triplet vertex fit) < 2	83.6%	68.4%
$p_\mathrm{T}(B) > 10$ GeV	80.1%	22.6%
Vertex detachment > 0.1mm	58.33%	0.3%
$\mathcal{P}(dE/dx) > 0.1$	87.8%	76.3%
Dalitz, m^2_{13} and $m^2_{23} > 2.5$ GeV	74.4%	35.9%
5.16 GeV < M(B) < 5.45 GeV	91.2%	5.8%
Overall	11.6%	$2.8 \cdot 10^{-4}$ %

Table 6.2: Signal and background efficiencies after various cuts. The cuts are applied in sequence.

Use of the dE/dx information

The selection criteria discussed above reduce the background by six orders of magnitude, while preserving about 12% of the signal, as it is shown in Table 6.2. In this section, the use of the dE/dx information is explained in detail.

Using the fast simulation, the detector read-out information is not available. The knowledge of the particle identity is therefore essential in order to simulate the detector dE/dx response to charged particle tracks. For a track with given p_T and η, the so-called dE/dx_{actual}, which in the full simulation would be the dE/dx as measured by the detector, was simulated using the sigma and the mean provided by the parameterization, described in Section 6.6, according to equation (6.1).

$$\left.\frac{dE}{dx}\right|_{actual} = \text{mean} + \textsc{rnd} * \sigma \tag{6.1}$$

where RND is a gaussianly distributed pseudo-random number.

For any given triplet of particles, two positive and one negative — candidates to be the decay products of the B^+ — the χ^2 distribution was constructed according to

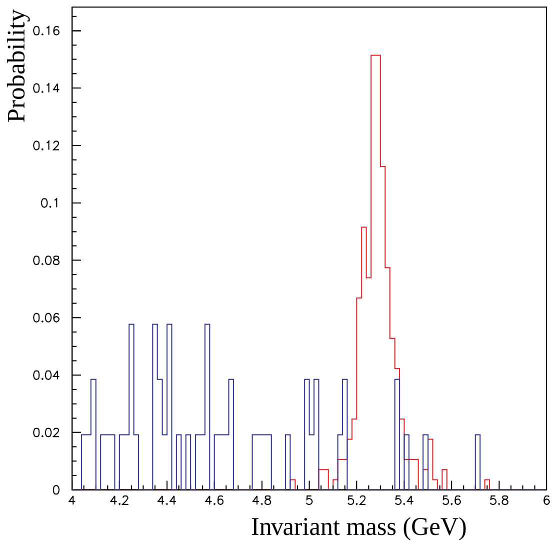

Figure 6.20: Invariant mass for all the possible triplets of two positive and one negative curvature tracks, after the application of all the cuts described above. These spectra are not normalized for the number of events expected at the LHC (see text).

formula (6.2):

$$\chi^2 = \sum_{i=1}^{3} \left[\frac{\frac{dE}{dx}\big|_{exp} - \frac{dE_i}{dx}\big|_{act}}{\sigma_i} \right]^2 \tag{6.2}$$

where the index i labels the individual particles in the triplet and dE/dx_{exp} (the expectation for the signal hypotesis) is given by the mean value of the dE/dx distribution for pions (if the track has negative curvature) or for kaons (if the track has positive curvature). The χ^2 probability for three degrees of freedom is then calculated. The χ^2 probability is constructed to be flat for the signal (as expected from equation (6.2)), while for the background it is peaked towards lower probability values, as is shown in Fig. 6.21. The background misidentification probability as a function of the signal efficiency is shown in Fig. 6.22 for the $\frac{dE}{dx}$ χ^2 probability after the proposed second level trigger (see Section 6.7.1).

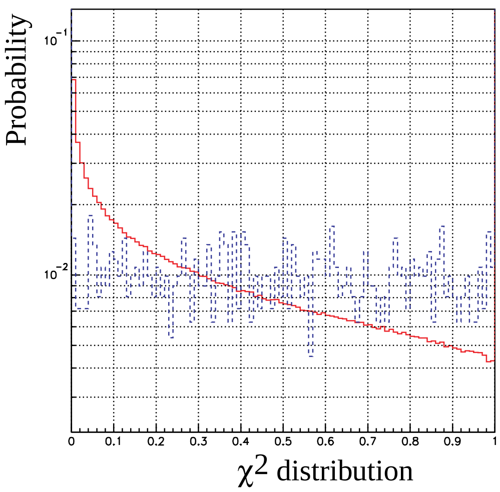

Figure 6.21: The χ^2 probability for three degrees of freedom for the signal (dashed line) and the background (solid line), as expected after the proposed second level trigger (see text).

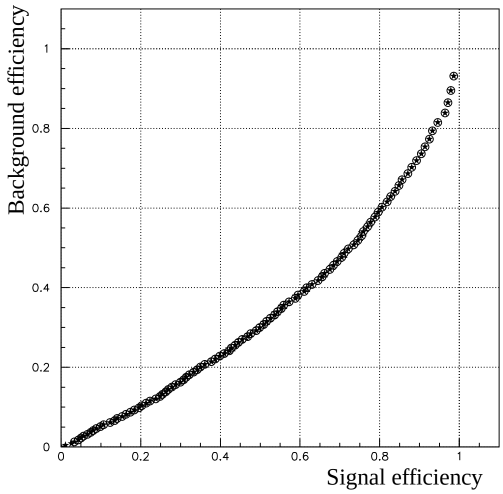

Figure 6.22: Background misidentification probability as a function of the signal efficiency, for the $\frac{dE}{dx}$ χ^2 probability after the proposed second level trigger (see text).

Results

The number of signal events produced during one year of running at low luminosity at the LHC can be estimated as follows:

$$N^{\rm prod}_{\rm signal} = \sigma({\rm pp} \rightarrow {\rm b\bar{b}} \rightarrow \mu 6{\rm X}) \times \mathcal{B}{\rm r}({\rm b} \rightarrow {\rm B}^+) \times \mathcal{B}{\rm r}({\rm B}^+ \rightarrow {\rm K}^+{\rm K}^+\pi^-) \times \mathcal{L} \times {\rm T} \tag{6.3}$$

and

$$N^{\rm obs}_{\rm signal} = {\rm N}^{\rm prod}_{\rm signal} \times \epsilon_{\rm reconstruction} \times \epsilon_{\rm identification} \tag{6.4}$$

where

- $\sigma({\rm pp} \rightarrow {\rm b\bar{b}} \rightarrow \mu 6{\rm X}) = 2.3\mu{\rm b}$
- $\mathcal{B}r({\rm b} \rightarrow {\rm B}^+) = 39.7\%$

- $\mathcal{B}r(\mathrm{B}^+ \rightarrow \mathrm{K}^+\mathrm{K}^+\pi^-) = 10^{-7}$(assumed)
- $\mathcal{L} = 10^{33}\mathrm{cm}^{-2}\mathrm{s}^{-1}$
- $T = 10^7$s for one year of running.
- $\epsilon_{\mathrm{reconstruction}} = 11.6\%$
- $\epsilon_{\mathrm{identification}}(\mu 6) = 85\%$
- $\epsilon_{\mathrm{identification}}(\pi, \mathrm{K}) = 90\%$

The number of produced signal events per year is thus $N^{\mathrm{prod}}_{\mathrm{signal}} = 913$, and the number of observed events is $N^{\mathrm{obs}}_{\mathrm{signal}} = 65$. The number of background events produced during one year of running at low luminosity at the LHC can be estimated as follows:

$$N^{\mathrm{prod}}_{\mathrm{back}} = \sigma(\mathrm{pp} \rightarrow \mathrm{b}\bar{\mathrm{b}} \rightarrow \mu 6\mathrm{X}) \times \mathcal{L} \times \mathrm{T} \tag{6.5}$$

The number of produced background events is thus $\mathrm{N}^{\mathrm{prod}}_{\mathrm{bg}} = 2.3 \times 10^{10}$.
Using $\epsilon_{\mathrm{reconstruction}} = 2.8\ 10^{-4}\%$ and $\epsilon_{\mathrm{identification}}(\mu 6) = 85\%$, $\epsilon_{\mathrm{identification}}(\pi, \mathrm{K}) = 90\%$, the number of observed background events is $\mathrm{N}^{\mathrm{obs}}_{\mathrm{bg}} = 4 \times 10^4$.
Assuming $\mathcal{B}r(\mathrm{B}^+ \rightarrow \mathrm{K}^+\mathrm{K}^+\pi^-) = 1 \times 10^{-7}$, the signal significance after one year of running is $S/\sqrt{B} = 0.3$ and after three years it is $S/\sqrt{B} = 0.6$.

If one requires signal significance of three standard deviations ($S/\sqrt{B} = 3$), an upper limit of the branching ratio of the signal is $\mathcal{B}r(\mathrm{B}^+ \rightarrow \mathrm{K}^+\mathrm{K}^+\pi^-) = 5.3 \times 10^{-7}$ after three years of low luminosity data-taking. The ATLAS experiment could therefore see this decay in the case of a SUSY scenario.

6.8 The $B_d^0 \to \pi^+\pi^-$ decay

As a second example of the importance of having some K/π separation (and, more generally, hadron identification) in ATLAS, the time-over-threshold information has been used for the study of the $B_d^0 \to \pi^+\pi^-$ decay, which is useful for extracting information about the angle α of the unitarity triangle used for CP-violation studies. The two-pion final state of the B_d^0 decay is plagued by various sources of background, mostly three or two-body decays involving also kaons and protons. The predicted $\pi^+\pi^-$ invariant mass spectrum for the ATLAS experiment, after three years of low-luminosity data-taking at the LHC is shown in Fig. 6.23, using recent values of the B_d^0 branching ratios (as quoted in [51]), and for a scenario without hadron identification in the ATLAS TRT.

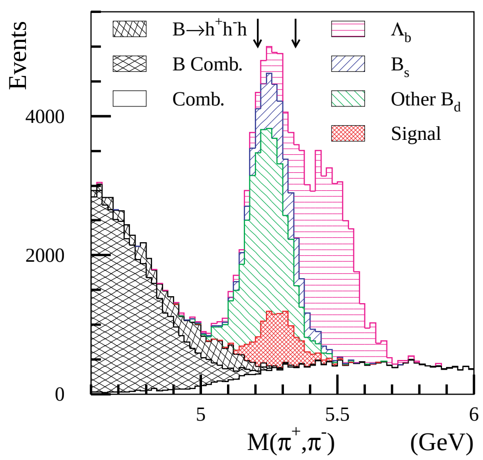

Figure 6.23: $\pi^+\pi^-$ mass spectrum in the ATLAS experiment for B_d^0 signal and various backgrounds and for the scenario without kaon-pion separation in the ATLAS TRT. From [51].

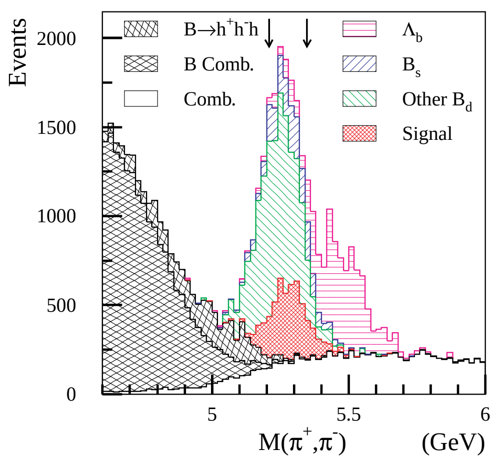

Figure 6.24: $\pi^+\pi^-$ mass spectrum in the ATLAS experiment for B_d^0 signal and various backgrounds and for the scenario with a kaon-pion separation in the ATLAS TRT as predicted by the study presented in this thesis (see text).

The signal is represented by the dark shaded area, while the various backgrounds (most of which lie just on top of the signal) are represented as lighter shaded regions [51]. As an illustration, the corresponding predicted $\pi^+\pi^-$ invariant mass spectrum when dE/dx information (via the time-over-threshold measurements in the TRT) is used is shown in Fig. 6.24, for a 50% efficiency for the $\mathrm{B_d^0} \rightarrow \pi^+\pi^-$ signal. The fraction of the signal in a window around the $\mathrm{B_d^0}$ mass improves from a value of 15% to a value of 21%. The accuracy of the measurement of the $\mathrm{B_d^0} \rightarrow \pi^+\pi^-$ asymmetry, which makes use of dE/dx information together with other information in an event-by-event maximum likelihood, is improved by about 35% with respect to the scenario without hadron identification in the ATLAS Inner Detector.

Conclusion

I have described in this thesis a novel technique for particle identification using the ATLAS Transition Radiation Tracker (TRT). This technique is based on signal-shaping information already available in the TRT front-end electronics. I used the time-over-threshold, defined as the width of the low-threshold (200 eV) discriminated pulse, as an estimator of the energy loss.

The analysis of test-beam data and detailed Monte Carlo simulations show that the time-over-threshold technique, like other methods based on multiple measurements of the particle's energy loss, improves particle identification in the low-energy region due to significant differences in the relativistic rise of the energy loss for different particles.

The test-beam data analysis, in particular, shows that significant electron-pion separation using time-over-threshold method is possible in the energy region below 10 GeV. In the test-beam experiment pion and electron beams of different energy were used to probe the time-over-threshold response of a straw equipped with a version of the analog chip very close to the final design.

In order to estimate the performance expected in the ATLAS TRT, where on average 35 straws will be crossed per track, hits from different events were combined to form pseudo-tracks. Using this novel time-over-threshold technique a pion misidentification probability ranging from $2.5 \cdot 10^{-2}$ at 5 GeV to $1 \cdot 10^{-1}$ at 20 GeV was measured, for a 90% electron efficiency.

Detailed Monte Carlo simulations for the ATLAS TRT detector, tuned on test-beam data, showed that for energy lower than 10 GeV a significant improvement with respect to the standard transition-radiation cluster-counting technique can be obtained by using also the time-over-threshold information. In particular, a factor of two improvement is expected at 5 GeV, while at the lower energy of 0.6-2 GeV the improvement is expected to be as large as one order of magnitude. The time-over-threshold technique, therefore, complements the cluster-counting technique in the low-energy region where the transition-radiation yield for electron is small and the electron-pion separation therefore is more problematic.

This development of the time-over-threshold method using test-beam data and the extrapolation to the performance expected in the ATLAS TRT detector has been described in an article submitted for publication [2].

References

[1] ATLAS Detector and Physics Performance Technical Design Report, CERN/LHCC/99-14,15, ATLAS TDR 14 (1999), p. 74-76 and ATLAS TDR 15 (1999) p. 577-582.

[2] T. Akesson et al., 'Particle Identification using the Time-over-Threshold Method in the ATLAS Transition Radiation Tracker', submitted to Nucl. Instr. and Meth. in Phys. Res.

[3] J. Damet, P. Eerola, A. Manara, S. Nooij, 'Searching for physics beyond the Standard Model in the decay $B^+ \rightarrow K^+K^+\pi^-$', ATL-PHYS-2000-027.

[4] The Large Hadron Collider Accelerator Project, LHC CERN/AC/93-03.

[5] The Large Hadron Collider Conceptual Design, LHC CERN/AC/95-05.

[6] G. Flugge. Future Research in High Energy Physics. In N. Ellis and M. B. Gavela, editors, 1993 European School of High Energy Physics, Yellow reports. CERN 94-04, 1994.
U. Egede, Ph.D. thesis, LUNFD6/(NFFL-7150) 1997.

[7] Particle Physics Booklet, Particle Data Group, Springer.

[8] CMS, The Compact Muon Solenoid, Technical Proposal, CERN/LHCC/94-38.

[9] LHCb, Technical Proposal, CERN/LHCC/95-70.

[10] ALICE, A Large Ion Collider Experiment, Technical Proposal, CERN/LHCC/95-71.

[11] S. Gottlieb, Particle Physics course, lecture notes, Indiana University.

[12] G. Altarelli, hep-ph/9809532.

[13] S. Weinberg, Phys. Rev. Lett. 19, 1264 (1967).

[14] S. Weinberg, Rev. Mod. Phys. 52, 515 (1980).

[15] R.S. Chivukula, hep-ph/9803219.

[16] G.C. Ross, Grand Unified Theories, Benjamin, New York, 1984.

[17] A. Sen, Proceedings of ICHEP'98, Vancouver, 1998.

[18] S. Dimopoulos, S. Raby, F. Wilczek, Phys. Rev. D24 (1981), 1681.

[19] ATLAS Collaboration, Technical Proposal for a General Purpose pp Experiment at the Large Hadron Collider at CERN, CERN/LHCC/94-43 (1994).

[20] ATLAS Inner Detector Technical Design Report, CERN/LHCC/97-17, ATLAS TDR 5 (1997).

[21] ATLAS Inner Detector Technical Design Report, CERN/LHCC/97-16, ATLAS TDR 4 (1997), p. 96-97.

[22] http://magboltz.web.cern.ch/magboltz

[23] V. L. Ginzburg and I.M. Frank, Zh. Eksp. Teor. Fiz. 16, 15 (1946)

[24] M. Cherry, G. Hartmann, D.Muller, T. A. Prince, Phyis. Rev. 10 (1974) 3594

[25] X. Artru, G. B. Yodh, G. Mennessier, Phys. Rev. D12 (1975), 1289

[26] M. Cherry, D. Muller, Phys. Rev. Lett. 38 (1977), 5

[27] M. Cherry, Phys. Rev. D 17(1978), 2245

[28] J. T. Shank et al., Nucl. Instr. and Meth. in Phys. Res., A310 (1991) 133.

[29] T. Akesson et al., Nucl. Instr. and Meth. in Phys. Res., A372 (1996) 70.

[30] T. Akesson et al., Nucl. Instr. and Meth. in Phys. Res., A412 (1998) 200.

[31] V. Bashkirov and B. Dolgoshein, ATLAS INDET-No-090 (1994).

[32] A. Artamonov et al, "DICE-95", internal note ATLAS-SOFT/95-14, CERN (1995).

[33] CN division Application Software group, GEANT detector description and simulation tool, CERN Program Library Long Writeup W5013, 1993

[34] ATLAS Inner Detector Technical Design Report, CERN/LHCC/97-16, ATLAS TDR 4 (1997), p. 90-91.

[35] V.M. Grishin, V.K. Ermilova, S.K. Kotelnikov, Nucl. Instr. and Meth. in Phys. Res., A307 (1991) 273.

[36] G.M. Garibian, L. A. Gevorgian, C. Yang, Nucl. Instr. and Meth. in Phys. Res., 125 (1975) 133.

[37] RD6 collaboration, ATLAS Internal Note, INDET-No-157.

[38] I. Gavrilenko, ATLAS Internal Note, ATLAS-INDET-No-165 (1997).

[39] ATLAS Detector and Physics Performance Technical Design Report, CERN/LHCC/99-15, ATLAS TDR 15 (1999), p. 561-618.

[40] The CLEO Collaboration, Phys. Rev. Lett. 71 (1993) 674-678.

[41] The CLEO Collaboration, Phys. Rev. Lett. 74 (1995) 2885-2889.

[42] L. L. Chau *et al.*, Phys. Rev. D 43 (1991) 2176.
C. D. Lu *et al.*, Phys. Lett. B 400 (1997) 188.

[43] C. D. Lu *et al.*, Phys. Lett. B 397 (1997) 279.

[44] D. Guetta and E.Nardi, Phys. Rev. D 58 (1998) 012001.

[45] K. Huitu *et al.*, Phys. Rev. Lett. 81 (1998) 4313.

[46] K. Huitu *et al.*, Phys. Lett. B 445 (1999) 394-398.

[47] G. Abbiendi *et al.*, OPAL Coll., Phys. Lett. B 476 (2000) 233-242.

[48] T. Sjostrand, Computer Physics Commun. 82 (1994) 74.

[49] E. J. Buis *et al.*, ATL-INDET-97-195.

[50] E. J. Buis *et al.*, ATL-INDET-98-215.

[51] Proceedings of the workshop on standard model physics (and more) at the LHC, G. Altarelli and M.L. Mangano editors, CERN 2000-004, p 329-333

Curriculum Vitae

Name:	Manara Andrea
Born the:	6 November 1969 in Turin (Italy)
Nationality:	italian
Marital status:	single
Phone number:	+39-011-842581
Mobile:	+39-338-5076177
E-mail address:	andrea.manara@cern.ch
Permanent address:	via Maria Cristina 14
	Pino Torinese (TO), 10025, Italy

Positions:

Graduate student, research assistant at Indiana University, since 1997.

CEA fellow, Saclay Laboratory (France), DISTO experiment, 1995-1996.

Education:

Ph.D. in Experimental High Energy Physics, 2000

Indiana University, Bloomington, IN

Thesis Topic: *Particle identification in the ATLAS TRT detector*

Laurea in Fisica with a 110/110 score, 1994

Universita di Torino, Torino, Italy

Thesis Topic: *Online and offline data analysis of the LPS detector at HERA*

Selected Publications

1. Particle Identification using the Time-over-Threshold Method in the ATLAS Transition Radiation Tracker, TRT collaboration, submitted to Nucl. Instr. and Meth. in Phys. Res. (2000).

2. Searching for physics beyond the Standard Model in the decay $B^+ \rightarrow K^+K^+\pi^-$, J. Damet, P. Eerola, A. Manara, S. Nooij, ATL-PHYS-2000-027.

3. Spin transfer in exclusive Λ production from pp collision at 3.67 GeV/c, F. Balestra et al., Phys. Rev. Lett. 83 (1999) 1534.

4. DISTO: A Large Acceptance Multiparticle Spectrometer for 1- 3 GeV Proton Beams, F. Balestra et al., Nucl. Instr. Meth. A426 (1999) 385.

5. Production of ϕ and ω mesons in near threshold pp reactions, F. Balestra et al., Phys. Rev. Lett. 81 (1998) 4572.

6. The DISTO Data Acquisition System at Saturne, IEEE Trans. Nucl. Sci. 45 (1998) 868.

7. The DISTO First Level Trigger at Saturne, IEEE Trans. Nucl. Sci. 45 (1998) 817.

Recent talks, schools and workshops

1. ATLAS week, CERN (Geneve), 2-6 October 2000.

2. Invited talk, Uppsala (Sweden), 14 September 2000.

3. TRT workshop, Philadelphia (U.S.A), 2-8 June 2000.

4. Candidacy seminar, Indiana University, 10 November 1999.

5. ATLAS week, CERN (Geneve), 4-8 October 1999.

6. Instrumentation School in particle physics, Istanbul (Turkey) 1-15 July 1999.

7. TRT workshop, Krakow (Poland), 1-6 June 1999.